Title
Development of a Scanning Probe Microscope and Studies of Graphene Grown on Copper

Author
Rasool, Haider Imad

Publication Date
2012

Peer reviewed|Thesis/dissertation

UNIVERSITY OF CALIFORNIA

Los Angeles

Development of a Scanning Probe Microscope and Studies of Graphene Grown on Copper

A dissertation submitted in partial satisfaction of the requirements for the degree Doctor of Philosophy in Chemistry

by

Haider Imad Rasool

2012

ABSTRACT OF THE DISSERTATION

Development of a Scanning Probe Microscope

and Studies of Graphene Grown on Copper

by

Haider Imad Rasool

Doctor of Philosophy in Chemistry

University of California, Los Angeles, 2012

Professor James K. Gimzewski, Chair

A description of the construction of a low noise fiber interferometer deflection sensor is presented in order to illustrate the capabilities of the developed home built scanning probe microscope (SPM). A description of the critical components and a rationale behind their implementation in the design of the sensor is provided. An analysis of an ideal interference cavity is used to understand the optimization of the deflection sensor towards achieving the highest possible sensitivity and lowest deflection noise density. The low noise interferometer can be used to detect the motion of micron sized resonators without the need for external lenses or polarization sensitive optical components, allowing for simplified implementation in a variety of circumstances. True atomic resolution imaging of muscovite mica in water by atomic force microscopy (AFM) is demonstrated using the developed sensor in the home built SPM.

Results on graphene grown on copper substrates by chemical vapor deposition (CVD) is provided. Graphene appears to grow over grains of different identities and across grain boundaries of the copper. Graphene island growth on the surface appears to depend on the

underlying substrate. Temperature dependent growth studies show a significant decrease in growth rate with decreasing temperature. The graphene grown on copper is shown to be transferable to arbitrary substrates and can be suspended across perforations in a receiving substrate. The knowledge gained from the growths on copper allowed for the successful fabrication of a new type of hybrid polymeric – conductive AFM probe using patterned silicon substrates and thin copper films.

Scanning tunneling microscopy (STM) was performed on graphene grown on copper substrates using the home built instrument. First, atomic scale STM imaging of graphene on polycrystalline copper substrates was accomplished. Graphene is shown to grow continuously over atomic steps, edges, and vertices of these corrugated copper surfaces. Continuous graphene growth is observed to exist over facets of different identities. The results on polycrystalline copper strongly suggests that the copper atoms are mobile during growth and that the underlying substrate does not limit graphene growth. In addition, STM was performed on graphene grown on copper (100) single crystals. The growth is again shown to be continuous over a wide range of surface features. The grown graphene exists in a variety of orientations with respect to the underlying copper crystal lattice. This leads to graphene overlayers which are polycrystalline in nature. Transmission electron microscopy (TEM) is used to reveal the crystallinity of graphene grown on single crystals and the real space distribution of the crystal domains in grown graphene. The compiled results of graphene growth on copper suggest that understanding and controlling the nucleation at the surface will ultimately be required for wafer scale growth of monolayer single crystal graphene on copper.

The dissertation of Haider Imad Rasool is approved.

Peter M. Felker

Yang Yang

James K. Gimzewski, Chair

University of California, Los Angeles

2012

I dedicate this thesis to my mother,

Nada Rasool,

whom I love very much.

TABLE OF CONTENTS

LIST OF FIGURES

ACKNOWLEDGEMENTS

I would like to thank my research advisor, Professor James K. Gimzewski, for his guidance, mentorship, and kind support over the years. I could not have accomplished the research presented in this thesis without his help. I have always enjoyed our discussions of science and am continuously amazed at his broad scientific knowledge across both the life and physical sciences. Jim's perspective of various fields has served as a continual source of inspiration and helped me realize that seemingly unrelated topics are often connected by fundamental principles. I also really appreciate that Jim took interest in the aesthetics of our scholarly work together, encouraging my creativity in presenting and publishing. Jim's mentorship will undoubtedly have a major impact on my future career and I am grateful to have had this experience. Thank you very much Jim.

I would like to thank my committee members, Professor Peter M. Felker and Professor Yang Yang, for their review of my oral examination and review of this doctoral dissertation. I would also like to thank Professor Richard B. Kaner for review of my oral examination and professional guidance over the years.

I am grateful to have been able to work with a variety of individuals from different disciplines. Emil B. Song, from the group of Professor Kang L. Wang of the Department of Electrical Engineering, has been a wonderful friend and colleague. Professor B. C. Regan and his group in the Department of Physics at UCLA have helped me tremendously and I am grateful to have found such a strong and fruitful collaboration.

I would also like to thank Harry Lockart and the Physics Machine Shop at UCLA. Harry made it possible for me to get my instrument up and running and was wonderful to work with.

Often times, I don't think I would have been able to accomplish what I did without his help. Thanks for everything Harry.

I would like to thank Henry D. Tran and Juan Villa for their friendship and support over these challenging years. In addition to being my close friend, Henry has read each one of my manuscripts and always provides invaluable advice for the presentation of my scholarly work. I know he has his own life and work to do and it means a lot that he sets aside his own time to help me. I look forward to our continued friendship. Juan, thanks for being like a brother to me and keeping me sane in times of insanity.

I want to thank Jennifer Andrade for her loving support and encouragement these last years of my doctoral work. Balancing personal and professional life can always be quite challenging and I am lucky to have met someone who is so understanding of my commitment to my work. Thanks for listening to my crazy ideas and taking interest in the things that I believe are interesting. I love you so very much.

Lastly, I would like to express my sincerest gratitude and appreciation to my family. My mother, Nada Rasool, always looked after me while I was growing up. Gave me the confidence, love, and support needed to proceed through life. I love you very much Mom and I miss you every single day. Words will never be able to express my gratitude, and for this reason, I will simply note that this thesis is dedicated to her. My brother, Jafar Rasool, has provided me with support and encouragement my entire life and somehow never ceases to amaze me. His character and huge heart has served as a source of inspiration. He is more than family, he is more than a best friend, he is a “big brother” in the truest sense. I love you man. And, of course, the man of men, my inspiration, the rock, my father, Imad Rasool. Again, words may never be enough, but I must try. My father has always given me support and love that allowed me to not only finish the work presented in this thesis, but to find my way through life. He believed in me every step of

the way and encouraged me in any pursuit. He only pushed me to relax and enjoy life and reminded me that sometimes it is necessary to take a moment and breathe. His advice provided me with clarity of thought and his love calmed my nerves. Thanks for everything. I love you very much Dad.

A large part of this thesis has appeared in three main articles that have been published during my work with Professor James K. Gimzewski. Each one of these articles has a variety of co – authors without whom the work may not have been possible.

Chapter 2 of this thesis is a version of an article published in the journal, *Review of Scientific Instruments*. The full article citation is as follows: Haider I. Rasool, Paul R. Wilkinson, Adam Z. Stieg, and James K. Gimzewski, "A low noise all – fiber interferometer for high resolution frequency modulated atomic force microscopy imaging in liquids," *Review of Scientific Instruments* 81, 023703 (2010). In this article, H.I.R. helped with the design of the deflection sensor, incorporated it into a scanning probe microscope, performed experiments, and wrote the manuscript. P.R.W. helped with the design of the deflection sensor and analysis of experimental data. A.Z.S. provided input on the design of the microscope. J.K.G. was the director of the project and oversaw all the work performed. Every author helped with the final manuscript.

Chapter 4 of this thesis is a version of an article published in the journal, *Nano letters*. The full article citation is as follows: Haider I. Rasool, Emil B. Song, Matthew J. Allen, Jonathan K. Wassei, Richard B. Kaner, Kang L. Wang, Bruce H. Weiller, James K. Gimzewski, "Continuity of Graphene on Polycrystalline Copper," *Nano Letters* 11, 251 (2011). In this article, H.I.R. performed STM experiments, analyzed experimental data, acquired X – Ray diffraction data, and wrote the manuscript. E.B.S. synthesized samples and provided experimental support.

M.J.A. helped construct experimental apparatus for sample synthesis. J.K.W. provided support for synthesis. R.B.K., K.L.W., and B.H.W. advised on the synthesis of samples. J.K.G. was the director of the project and oversaw the STM work. Every author helped with the final manuscript.

Chapter 5 of this thesis is a version of an article published in the journal, *Journal of the American Chemical Society*. The full article citation is as follows: Haider I. Rasool, Emil B. Song, Matthew Mecklenburg, B. C. Regan, Kang L. Wang, Bruce H. Weiller, James K. Gimzewski, "Atomic-Scale Characterization of Graphene Grown on Copper (100) Single Crystals," *Journal of the American Chemical Society* 133, 12536 (2011). H.I.R. acquired STM images, SEM images, analyzed experimental data, and wrote the manuscript. E.B.S. synthesized samples and provided experimental support. M.M. acquired all TEM data. B.C.R. oversaw the TEM work. K.L.W. and B.H.W. oversaw the synthesis of samples for the study. J.K.G. was the director of the project and oversaw the STM work. Every author helped with the final manuscript.

VITA

EDUCATION

2001 – 2006 University of California, Los Angeles, CA
Bachelor of Science, Biochemistry (*cum laude*)
GPA: 3.71, Major Requirement GPA: 3.90

RESEARCH

2006 – 2012 University of California, Los Angeles, CA
Graduate Student Researcher, Department of Chemistry
Advisor: Professor James K. Gimzewski

2008 National Institute for Materials Science, Tsukuba, Japan
Invited Researcher, Atomic Electronics Group
Advisor: Dr. Tsuyoshi Hasegawa

2005 – 2006 University of California, Los Angeles, CA
Undergraduate Researcher, Department of Chemistry
Advisor: Professor Richard B. Kaner

HONORS AND AWARDS

2009 John Jordan Fellowship Award, UCLA

2007 Excellence in Teaching, UCLA

2006 Ralph H. Bauer Award for Excellence in Inorganic Chemistry, UCLA

2006 Bachelor of Science Highest Honors, UCLA

PUBLICATIONS

2011 **H. I. Rasool**, E. B. Song, M. Mecklenburg, B. C. Regan, K. L. Wang, B. H. Weiller, J. K. Gimzewski, "Atomic-Scale Characterization of Graphene Grown on Copper (100) Single Crystals," *Journal of the American Chemical Society* 133, 12536 (2011).

H. I. Rasool, E. B. Song, M. J. Allen, J. K. Wassei, R. B. Kaner, K. L. Wang, B. H. Weiller, J. K. Gimzewski, "Continuity of Graphene on Polycrystalline Copper," *Nano Letters* 11, 251 (2011).

2010 **H. I. Rasool**, P. R. Wilkinson, A. Z. Stieg, and J. K. Gimzewski, "A low noise all – fiber interferometer for high resolution frequency modulated atomic force microscopy imaging in liquids," *Review of Scientific Instruments* 81, 023703 (2010).

S. Sharma, **H. I. Rasool**, V. Palanisamy, C. Mathisen, M. Schmidt, D. T. Wong, J. K. Gimzewski, "Structural-Mechanical Characterization of Nanoparticle Exosomes in Human Saliva, Using Correlative AFM, FESEM, and Force Spectroscopy," *ACS Nano* 4, 1921 (2010).

2009 M.B. Weinberger, J.B. Levine, H.-Y. Chung, R.W. Cumberland, **H.I. Rasool**, J.M. Yang, R.B. Kaner, and S.H. Tolbert, "Incompressibility and Hardness of Solid Solution Transition Metal Diborides: $Ru_{1-x}Os_xB_2$" *Chemistry of Materials* 21, 1915 (2009).

2008 J.B. Levine, S.L. Nguyen, **H.I. Rasool**, J.A. Wright, S.E. Brown, and R.B. Kaner, "Preparation and Properties of Metallic, Superhard Rhenium Diboride Crystals," *Journal of the American Chemical Society* 130, 16953 (2008).

A.Z. Stieg, **H. I. Rasool**, and J.K. Gimzewski, "A flexible, highly stable electrochemical scanning probe microscope for nanoscale studies at the solid-liquid interface," *Review of Scientific Instruments* 79, 103701 (2008).

PRESENTATIONS

2012 "Understanding Graphene Growth on Copper Substrates"
Talk delivered at the 243rd American Chemical Society Spring Meeting, "Chemistry of Life."
Authors: **H. I. Rasool** and J. K. Gimzewski

"Understanding Graphene Growth on Copper Substrates"
Talk delivered at the 2012 Materials Research Society Spring Meeting.
Authors: **H. I. Rasool** and J. K. Gimzewski

2009 "Development of a NC – AFM for Ambient and Liquid Environments"
Poster presented at the 12th International Conference on Noncontact Atomic Force Microcopy and Casimir 2009 Workshop.
Authors: **H. I. Rasool**, S. Sharma, and J. K. Gimzewski

2008 "High Performance Atomic Force Microscopy for Ambient and Liquid Environments" Talk delivered at the 5th NIMS-IRC-UCLA Nanotechnology Summer School, Tsukuba, Japan
Authors: **H. I. Rasool** and J. K. Gimzewski

CHAPTER 1

INTRODUCTION

1.1 BRIEF DISCUSSION OF SCANNING PROBE MICROSCOPY

A scanning probe microscope (SPM) is a general term used to describe a type of microscope that works by positioning a local probe over a surface and performing a lateral scan to generate a topographic image. This type of image construction is likened to the way a person without use of their eyes navigates through their environment by use of the sense of touch. Physical contact with the environment is required to generate a real space distribution of the objects around them. The type of probe and signal used to generate the topographic image in a lab instrument can be altered to provide a wealth of information about a given surface. While a variety of probes and imaging signals exist, the two most commonly used SPM techniques are scanning tunneling microscopy (STM) [1] and atomic force microscopy (AFM) [2]. The STM works by measuring a current that is passed between a conductive tip and a conductive sample. In order to generate the current when an electrical bias is applied between the two electrodes. Thus, the contrast or height scale seen in STM images is a convolution of local variations of the electronic structure of the surface and the physical topography of the sample.

The AFM works by using the force generated between a tip and the surface to generate an image of the sample topography. In the simplest configuration, the movement of the tip apex towards or away from the sample due to the attractive or repulsive interactions, generates a signal that is monitored to create an image of the sample topography. This method of imaging is commonly referred to as contact mode – AFM (CM – AFM), since the tip of the probe is essentially placed into contact with the sample and swept across the surface. One major drawback of CM – AFM is that the lateral forces on the sample are usually large and can cause considerable irreversible damage to the surface. In order to alleviate these damaging lateral forces on the sample, dynamic modes of AFM imaging were developed.

Two of the most most popular dynamic modes of operation are amplitude modulated –

AFM (AM – AFM) [3] and frequency modulated – AFM (FM – AFM) [4]. In AM – AFM the tip is oscillated above the sample with an initially known free oscillation amplitude and the change in amplitude due to the interaction force between the tip and the sample is monitored. The act of oscillation minimizes the total interval of time in which the tip is interacting with the sample and thus ultimately minimizes the deleterious affects of the lateral forces. The FM – AFM technique is similar to AM – AFM. An oscillating tip is again used to measure the interaction force, however, in this mode of imaging the change in the frequency of the oscillation compared to the free oscillation frequency is measured while maintaining a constant amplitude of oscillation. A major advantage of FM – AFM over AM – AFM is a straightforward deconvolution of the frequency change to the gradient of the force interaction between the tip and sample. In addition, true atomic resolution imaging of surfaces with FM – AFM can be achieved more readily than other modes of operation [5].

1.2 THESIS OVERVIEW

The thesis first describes instrumentation development and follows with results on the growth of graphene on copper substrates. Design and construction of a home – built SPM was first accomplished. In general, it is desirable to construct an SPM system that can scan at high speeds with true atomic resolution of a variety of surfaces in different imaging modes, have a large dynamic range of different imaging scales, and also maintain a reasonable level of usability. In practice, however, many sacrifices must be made in design criteria to achieve the best possible performance and reduce overall cost. With this in mind, the specific goal of true atomic resolution imaging in both AFM and STM modes of operation in ambient and liquid environments was established and the machine was designed accordingly.

Once the microscope was operational and true atomic resolution imaging was

accomplished, we looked to use the microscope to study scientific problems of interest. Samples of graphene grown on copper substrates were chosen as the ideal candidate, since an understanding of the growth process at the atomic scale was lacking. The first set of experiments primarily involved STM imaging of graphene grown on polycrystalline copper substrates. Large area images of the sample topography were acquired to understand the general sample morphology. Then, specific sites of interest on the sample surface were imaged with atomic resolution to understand the grown material and make conclusions about how the reaction propagation occurs. A similar analysis was then performed on graphene samples grown on copper (100) single crystal substrates. In addition, to imaging with the STM, a more holistic view of the growth was obtained by imaging the samples with an SEM and TEM.

In Chapter 2 of this thesis, the development of the home – built microscopes low noise all-fiber interferometer is discussed to demonstrate the instruments capabilities. The deflection sensor is optimized for liquid environment FM – AFM. A detailed description and rationale for the choice of the critical components is provided along with the design of a simple alignment assembly. The optimization of the deflection sensor towards achieving the highest possible sensitivity and lowest deflection noise density is discussed in the context of an ideal interference cavity. Based on the provided analysis we have achieved deflection noise densities of 2 fm/√Hz on commercially available cantilevers in both ambient and liquid environments. This translates into a root mean square amplitude noise of approximately 10 picometers with a measurment bandwidth of 1000 Hz. The low noise interferometer works without the need for differential detection, special focusing lenses, or polarization sensitive optics, dramatically simplifying measurements. True atomic resolution imaging of muscovite mica by FM – AFM in water is demonstrated using the developed deflection sensor in the home – built SPM.

In Chapter 3, the characterization of graphene growth on polycrystalline copper foil is

discussed. A majority of the body of work presented in this chapter serves as the basis for the general understanding required to perform the experiments required for the high resolution imaging and studies presented in Chapter 4 and 5 of the thesis. Graphene is shown to grow over the entirety of the copper surface, with different copper crystal grains producing different island growth morphologies. The reactions performed at lower temperatures show a significant decrease in reaction rates as well as varied growth morphology when compared to high temperature growths. Using developed transfer techniques, the graphene can successfully be transferred to arbitrary substrates of interest for further analysis. TEM analysis of suspended transferred samples indicate that the graphene is polycrystalline in nature, with monolayer sheets continuously stitched together. The knowledge gained from this work was applied to the fabrication of graphene coated AFM probes from patterned substrates. Lastly, a demonstration of the graphene coated AFM probes ability to image test samples is presented.

In Chapter 4, the atomic structure of graphene on polycrystalline copper substrates was studied using scanning tunneling microscopy (STM). The graphene overlayer is shown to maintain a continuous pristine atomic structure over atomically flat planes, monatomic steps, edges, and vertices of the copper surface. Facets of different identities are found to be overgrown with graphene's perfect carbon honeycomb lattice. These observations suggest that growth models including a stagnant catalytic surface do not apply to graphene growth on copper. Contrary to the initial expectations, these results reveal that the growth of macroscopic pristine graphene is not limited by the underlying copper atomic structure.

In Chapter 5, growth of graphene on copper (100) single crystals is discussed. The atomic structure of the graphene overlayer was studied using STM. A detailed analysis of moiré superstructures present in the graphene topography reveals that growth occurs in a variety of orientations over the square atomic lattice of the copper surface. Transmission electron

microscopy is used to elucidate the crystallinity of the grown graphene. Pristine, defect-free, graphene is observed over copper steps, corners, and screw dislocations. Distinct protrusions, known as “flower” structures, are observed on flat terraces, which are attributed to carbon structures that depart from the characteristic honeycomb lattice. Continuous graphene growth also occurs over copper adatoms and atomic vacancies present at the single crystal surface. Copper atom mobility within vacancy islands covered with suspended graphene sheets reveals a weak graphene – substrate interaction. The observed continuity and room temperature vacancy motion indicates that copper mobility likely plays a significant role in the mechanism of sheet extension on copper substrates. Lastly, the presented results suggest that the quality of graphene grown on copper substrates will ultimately be limited by the nucleation at the surface of the metal catalyst.

In Chapter 6, a summary of the thesis is provided and conclusions of each chapter are discussed. Possible future work for instrument development and suggestions for the improvement of the home – built microscope are discussed. In addition, possible directions for graphene related research are discussed.

1.3 REFERENCES

[1] G. Binning, G.; Rohrer, H.; Gerber, C.;Weibel, E. *Phys. Rev. Lett.* **1982,** 49, 57.

[2] G. Binning, C. F. Quate, and C. Gerber, *Phys. Rev. Lett.* **1986**, 56, 930.

[3] Martin, Y.; Williamns, C.C.; Wickramasinghe, H. K. *J. Appl. Phys.* **1987**, 61, 4723.

[4] Albrecht, T. R.; Grütter, P.; Horne, D.; Rugar, D. *J. Appl. Phys.* **1991**, 69, 668.

[5] Giessibl, F. J. *Rev. Mod. Phys.* **2003**, 75, 949.

CHAPTER 2

DEVELOPMENT OF A LOW NOISE INTERFEROMETER

2.1 INTRODUCTION

Since the original conception of the atomic force microscope (AFM) [1] and through the development of dynamic modes of operation, it is now possible to obtain true atomic resolution [2] images using the frequency modulation imaging technique (FM – AFM) [3]. In ultra high vacuum (UHV) environments it is possible to image the charge state of surface adsorbate atoms [4], subsurface atomic vacancies [5], and the atomic structure of isolated molecules [6]. Recently, there has also been rapid progress in molecular and atomic resolution imaging in ambient [7] and liquid [8,9] environments. Using FM – AFM it is possible to image the hydration layers above supported lipid bilayers with molecular scale resolution [10], voltage – dependent anion channels in native membranes [11], and lipid – ion networks [12] under physiological conditions. Many of these advances can be attributed to the development of high performance deflection sensors [13 – 15] for the transduction of the tip – sample interaction to a measurable signal.

In ambient and liquid environments the reduction of the displacement sensor noise was found to be the critical factor in obtaining high resolution images [16]. Reducing the sensor noise allows for the use of small oscillation amplitudes, which enhance the sensitivity to short range interactions that are necessary for obtaining true atomic resolution images [17]. The deflection noise density obtained in air and water was reduced to 17 and 40 fm/√Hz, respectively, from typical values of 100 – 1000 fm/√Hz in air by optimizing an optical beam deflection (OBD) sensor [16]. Similar results on mica and the cytoplasmic surface of purple membrane were reported [18] through the use of a low noise Fabry – Perot (FP) interferometer sensor with a deflection noise floor of 1 fm/√Hz that employed a focusing lens system and differential amplification [19]. These two optical methods are popular since they are relatively easy to implement in liquid environment imaging and provide excellent noise characteristics without imposing stringent conditions on the type of probe used for experimentation.

We have chosen to develop an all-fiber Fabry-Perot (FP) interferometer for use as the deflection sensor for high resolution FM – AFM imaging in liquid environments, which can be used with a variety of cantilever probes of different dimensions and mechanical properties. A fiber positioning assembly constructed from inexpensive commercial parts has been included in the sensor design to rapidly align a cleaved optical fiber flat over exchanged cantilever probes. This capability is important in liquid environments where probes are exchanged often, due to enhanced tip aging as compared to ambient or vacuum environment imaging. In addition to the versatility, we have focused on making the sensor simple to use and easy to construct from commercially available parts. The sensor does not require a special optical lens system or polarization sensitive optics, thereby reducing the complexity of the experimental setup. We also use a direct amplification of the reflected light from the interference cavity rather than a differential amplification scheme [20], which greatly simplifies the electronic measurement and reduces the shot noise of the sensor by a factor of 2 in comparison to the differential scheme.

In this chapter we describe the construction and optimization of our interferometer deflection sensor which achieves noise densities of 2 fm/√Hz in both air and water when aligned on commercially available cantilevers. An overview of the design and operation is given along with a detailed rationale for the choice of the critical components of the developed sensor. A discussion of the ideal FP cavity is presented in order to provide a basis for understanding the optimization of the constructed interferometer. In addition, a detailed analysis of the sensitivity and deflection noise density due to the photodiode shot noise is presented in the context of the ideal FP cavity and compared to experimental results obtained between a fiber and plane mirror. Typical interference patterns and deflection noise densities obtained on commonly used cantilevers is provided and compared to results obtained on a plane mirror. Lastly, true atomic

resolution FM – AFM imaging of muscovite mica in water is demonstrated with the developed all-fiber interferometer deflection sensor.

2.2 EXPERIMENTAL SETUP

2.2.1 Operation and Components

Figure 2.1 provides a schematic overview of the constructed interferometer for use as the deflection sensor in a modified home – built AFM [21] for imaging and experimentation in ambient and liquid environments. A fiber coupled laser diode (LD) [22] is used to inject light into a fiber optic circulator [23]. The light enters the circulator and is sent through a fiber positioning assembly to the interference cavity generated between the fiber end face and a mirror, or a reflective cantilever probe. The fraction of light reflected by the two mirror cavity is determined by a periodic function of distance that is described in detail in the following section. The reflected light is then passed back through the fiber optic circulator and routed to a fiber pigtailed photodiode (PD) [24]. The illuminated photodiode generates a current, which is fed into a current – to – voltage converter (FEMTO: DHPCA-100) that is connected to a computer-based control system used for imaging and experimentation.

The laser light source is a narrow line width low noise distributed feedback (DFB) laser diode for dense wavelength division multiplexing (DWDM) telecom applications in a 14-pin butterfly package. Several features of this type of laser diode make it an excellent choice for use in a practical sensor. The laser diode has an integrated thermoelectric cooler (TEC) and thermistor for precise temperature control of the laser to within 0.01 °C. Since the TEC element

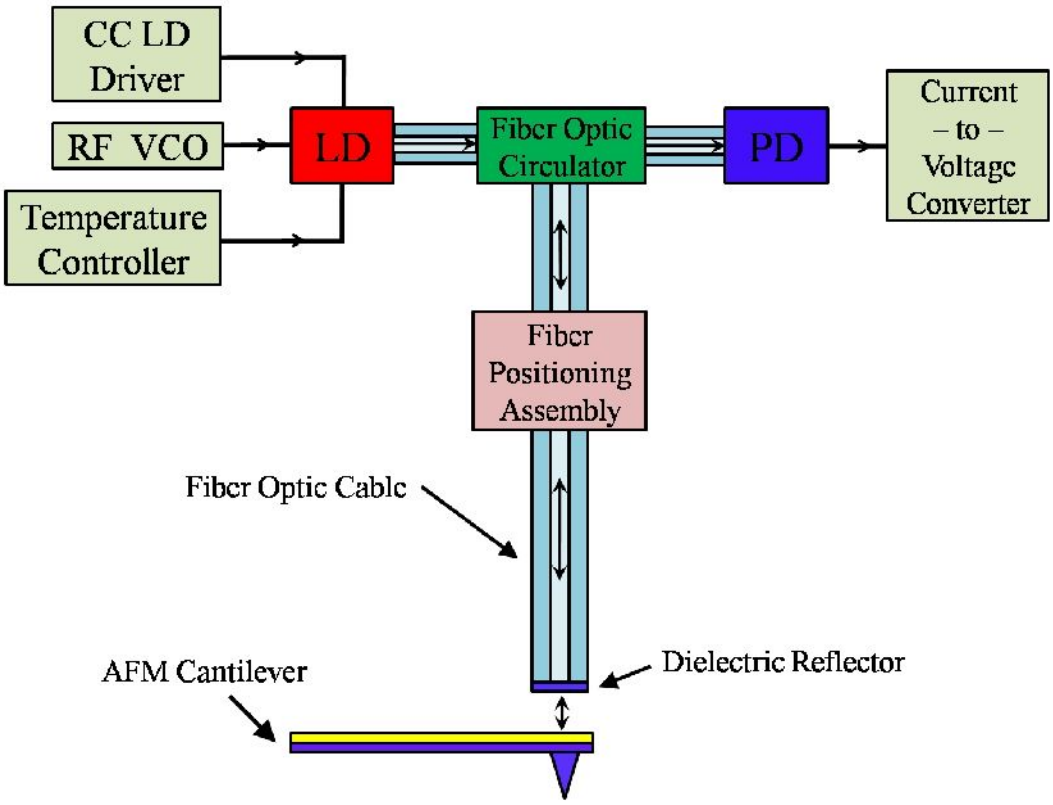

Figure 2.1. Experimental set – up for the fiber optic interferometer deflection sensor.

and sensing thermistor are mounted very close to the laser diode chip, the temperature controller (Thorlabs: TED200C) is able to respond very quickly to small changes in temperature providing excellent low frequency characteristics of the laser output. Maintaining a constant temperature ensures the lowest possible noise output and a well defined output wavelength when a constant current (CC) laser diode driver (Thorlabs: LDC201CU) is used to operate the laser. An integrated photodiode is also present in the module for optional monitoring of the output intensity of the laser. This diode is implemented when an automatic power control (APC) unit is used. When a CC source is employed, it is possible to use this photodiode to generate the reference signal in a differential amplification scheme.

The laser diode also has an integrated 30 dB Faraday isolator at the output of the module. This allows light to be passed in the forward direction, but attenuates any back reflected light

from the interference cavity to the laser by three orders of magnitude, greatly reducing laser noise and increasing laser life-time. When back reflected light enters the laser cavity it can induce intensity oscillations in the output, leading to what is called "optical feedback noise" (OFN), significantly degrading the performance of the sensor [16]. Although the optical isolator works well to minimize OFN it does not completely eliminate it. A second feature of the laser module that helps manage OFN is an integrated bias tee in the laser drive circuitry. The bias tee has a bandwidth of 45 – 860 MHz and allows for the injection of radio frequency (RF) current from a voltage controlled oscillator (VCO), approximately 200 MHz, to the laser. This effectively converts the laser from single to multi mode. This reduces the effect of OFN, which often causes fluctuations in the output by inducing the competition of similar modes within the laser cavity. The RF injection also helps reduce noise associated with laser intensity fluctuations caused by the interference of light between different optical interfaces within the fiber system. This "optical interference noise" (OIN) is reduced due to a decrease in the coherence length of the emitted light by the laser [16]. While the RF injection decreases the coherence of the laser, no degradation to the working distance has been observed.

The fiber optic circulator and the fiber pigtailed photodiode were also specifically chosen for use in our low noise deflection sensor. The fiber optic circulator replaces the traditionally used 2 × 2 coupler [20] in our interferometer. A 2 × 2 coupler is used to split the light emitted from the laser along two separate paths, one leading to the reference photodiode and the other into the interference cavity. While the combination of the coupler and the differential scheme are effective at reducing laser intensity noise, the photodiode shot noise limit of a directly amplified interferometer is half that of the differential set – up because there is no correlation between the shot noise of the two different detectors. The fiber optic circulator also increases the optical throughput of the interferometer and makes it possible to operate the laser at output powers much

lower than the rated power, which tends to produce less laser intensity noise at the photodiode. A low back reflection fiber pigtailed photodiode has also been implemented into the sensor. This is designed to minimize back reflection from the active area of the photodiode via an angled cleave at the fiber end. The cut is made at the point where the fiber passes light onto the active area of the photodiode and reflects back scattered light out of the fiber cable system. The angled cleave helps reduce the OFN associated with back scattered light reaching the laser diode and reduce OIN generated between fiber optic connectors and the fiber end – photodiode gap.

2.2.3. Fiber Positioning Assembly

A commercial fiber optic manipulator (Newport: FP-2A) in combination with a piezoelectric stack actuator (PI Ceramic: P-016.00H) and custom fabricated hardware is used for course and fine positioning of the fiber end face over a cantilever probe. This fiber positioning assembly is depicted in **Figure 2.2**. The ring piezo stack with an attached aluminum sleeve is mounted to the manipulator with an epoxy adhesive. The aluminum sleeve is tapped and a set screw is used to hold the optical fiber chuck. The stripped end of a bare optical fiber, outer diameter 125 μm, is placed into a machined slit of the fiber chuck and held down with a thin brass leaf spring. Once the fiber is clamped onto the fiber chuck, a thin brass plate (not shown) is inserted into the slit to further secure the fiber within the assembly and reduce the probability of crack or fracture.

The piezo stack has a range of motion of approximately 5 μm, which is sufficient to calibrate the sensor before each experiment. While a large range of motion is desirable in order to check the quality of the alignment by the fringe pattern, it can lead to enhanced susceptibility to electromechanical noise caused by electrical coupling to the surrounding environment. In

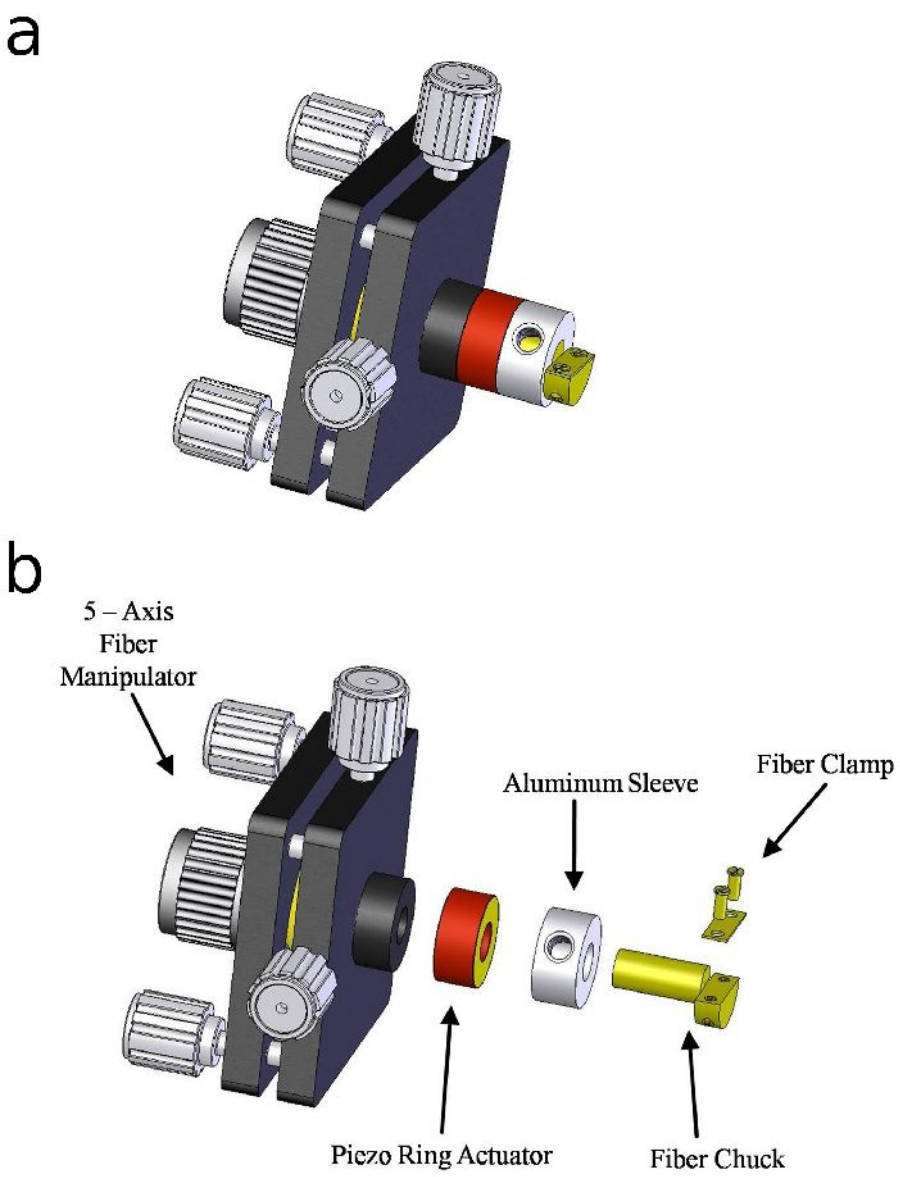

Figure 2.2. Schematic of the fiber positioning assembly. CAD drawing of the (a) assembled and (b) exploded view of the assembly required for course and fine positioning of the fiber optic cable over a mirror or cantilever.

order to reduce such noise in the deflection sensor output, we place low pass filters between the control electronics and the high voltage (HV) amplifier (RHK Technology: HVA 900) and in the line after amplification. During AFM imaging or force spectroscopy experiments the fiber – cantilever distance is held constant at a point where the slope of the fringe pattern is largest using the ring piezo on the fiber holder and a digital proportional – integral – derivative (PID) feedback

loop. The feedback loop is able to keep the average distance between the fiber end face and cantilever constant to within a few nanometers.

2.3. INTERFEROMETER DESCRIPTION

2.3.1. Ideal Interference Cavity

An interference cavity generated by placing a flat cleaved optical fiber close to a cantilever backing is essentially a Fabry-Perot Etalon. The well known mathematical description for the reflected power, P_r, generated between two identical reflective surfaces [25] as one varies the distance is given by

$$P_r = P_i \frac{F \sin^2 \frac{\delta}{2}}{1 + F \sin^2 \frac{\delta}{2}} = P_i \times \Theta(R, z) \tag{1}$$

The parameters F and δ are given by

$$F = \frac{4\mathrm{R}}{(1-R)^2} \tag{2}$$

$$\delta = \frac{4\pi n z}{\lambda_o} \tag{3}$$

here, P_i, R, n, λ_0, and z are the incident power, reflectivity, index of refraction between the surfaces, the wavelength of the light source in vacuum, and the separation, respectively. The derivative of the reflected power as a function of distance is given as

$$P_r' = P_i \frac{2\pi n}{\lambda_o} \frac{F \sin \delta}{\left(1 + F \sin^2 \frac{\delta}{2}\right)^2} = P_i \times \Phi(R, z) \tag{4}$$

In this treatment several idealized conditions are imposed to obtain a relatively simple expression. A completely monochromatic light source is assumed, absorption or losses at the two identical interfaces are neglected, and every light ray reflected from the cavity is accounted for through transmission or reflection. Although this is not the exact case for a real fiber optic based interferometer, we have found it helpful to understand the idealized case to make predictions about optimization of our experimental setup. It is possible to describe the interference cavity using two reflective surfaces of different identities [19] without significantly changing the discussion regarding optimization of the FP deflection sensor. The most notable effect observed in the interference pattern is the presence of an offset of the minima above zero reflected power. In addition, their exists a trade-off between enhancing the reflectivity of one of the surfaces with respect to the other and matching the reflectivity of the two surfaces to obtain the maximum possible sensitivity.

Without the use of focusing optics, it is useful to include a simple correction for the finite size of a fiber optic cable aperture to understand the experimental results. The fraction of light coupled back to a perfectly aligned fiber from a perfectly reflecting mirror can be considered as a special case of the coupling efficiency of optical fibers within the gaussian field approximation [26]. In this special case, the fraction of light coupled back into the fiber is simply,

$$F_c = \left[1 + \left(\frac{z}{z_r}\right)^2\right]^{-1} \tag{5}$$

where z is the spacing between the optical fiber end face and the reflective mirror, and z_r is the Rayleigh length given by,

$$z_r = \frac{\pi n w^2}{\lambda_o} \tag{6}$$

where w is the mode field radius of the optical fiber. If the mirror is not perfectly reflecting, then the light will further be attenuated by an amount proportional to the reflection coefficient of the mirror. This leads to an effective reflection coefficient, R_{eff}, of the mirror surface given by

$$R_{eff} = F_C R_{mirror} \tag{7}$$

Equation (7) shows that by changing the fiber to mirror distance, R_{eff} of the mirror can be matched to the optical fiber end face. When the reflection coefficients are identical, Eqs. (1) – (3) provide an excellent description for the back reflected power.

2.3.2. Sensitivity and Deflection Noise

The sensitivity, S, of a deflection sensor is defined as the change in voltage that occurs with a change in position. This quantity can be calculated from the derivative of the reflected power given in Eq. (4). The product of the value of the function, Φ, at a specifically chosen operating distance, z_{op}, and scaled by the appropriate quantum efficiency, η, of the photodiode, the current – to – voltage feedback resistance, R_{IV}, and incident power gives the sensitivity in V/nm. Thus, the sensitivity is given by

$$S = \frac{\Delta V}{\Delta z} = P_i \times \Phi(R, z_{op}) \times \eta \times R_{IV} \tag{8}$$

The above expression shows that the sensitivity can be increased by generating interference patterns of higher slopes. This can be accomplished by increasing the reflectivity or incident power at the cavity. While the sensitivity plays an important role in the description of the devices performance, it is more meaningful to discuss the sensitivity in conjunction with the deflection noise density. This is because an increase in sensitivity alone can not necessarily increase the signal – to – noise ratio (SNR) of the deflection sensor. The major noise sources such as

Johnson, laser, and photodiode shot noise need to remain constant or increase less rapidly than an increase in sensitivity, to obtain an overall increase in SNR.

The performance of a well designed optical deflection sensor will ultimately be limited by the photodiode shot noise. The shot noise causes a voltage noise across a load resistor given by

$$\delta V_s = R_{IV}\sqrt{2e\eta P_r B} \tag{9}$$

here, e and B are the electron charge and bandwidth of the measurement, respectively. These voltage noise fluctuations give rise to an effective deflection noise density given by

$$\delta n_{ZS} = \frac{\delta V_s / \sqrt{B}}{S} \tag{10}$$

Equation (10) highlights how increasing the sensitivity alone may not decrease the effective deflection noise density if a subsequent increase in voltage noise occurs.

In order to minimize the deflection noise density it is important to understand how it varies with reflectivity and power. Using Eqs. (1) and (8) – (10) we find that the deflection noise density can be expressed as

$$\delta n_{ZS} = \left(\frac{\Theta(R, Z_{op})^{1/2}}{\Phi(R, z_{op})}\right)\sqrt{\frac{2e}{\eta P_i}} \tag{11}$$

Equation (11) reveals two distinct contributions to the photodiode shot noise, a cavity term and a power term. The cavity term is quite general and can be applied to any interference cavity whose functional form is similar to that expressed in Eq. (1). We also find from Eq. (11) that the deflection noise density due to photodiode shot noise varies as the inverse root of the incident power, which is similar to the result found for an OBD sensor [27].

2.3.3. Sensor Optimization

The first parameter worthy of consideration when optimizing an interferometric deflection sensor is the reflectivity, *R*. **Figure 2.3a** and **2.3b** show the calculated reflected power and absolute value of the slope of the curves for four different reflectivities as the distance between the two plates is changed one wavelength in air. The maximum slope increases dramatically as one changes the reflectivity from 0.04 to 0.74. In addition, a change in reflectivity leads to a change in the operating distance that gives the maximum slope and hence a maximum sensitivity to changes in displacement. Therefore, for a given incident power at the cavity, an increase in reflectivity increases the power at the photodiode when working at the maximum slope. These two effects tend to act against each other in the case of minimizing the deflection noise density since both Θ and Φ increase in value. In order to understand the extent of these effects, we have used Eq. (11) to calculate the deflection noise density at varying *R* values when the interferometer is positioned at the z_{op} where the slope of the interference curve is a maximum. As can be seen from **Figure 2.3c** increasing the reflectivity of the two surfaces, and hence the sensitivity, provides an overall decrease in deflection noise density.

While increasing the reflectivity between the two surfaces decreases the deflection noise density it has dramatic consequences for practical operation. The maximum working oscillation amplitude decreases as one increases the reflectivity since large oscillation amplitudes lead to non-linear changes in the reflected intensity at the photodiode. In addition, the measurement becomes more susceptible to drift between the two surfaces due to the change in slope with operating distance. Using the fiber positioning assembly with active feedback of the operating distance minimizes this effect but can not completely eliminate drift between the fiber and cantilever.

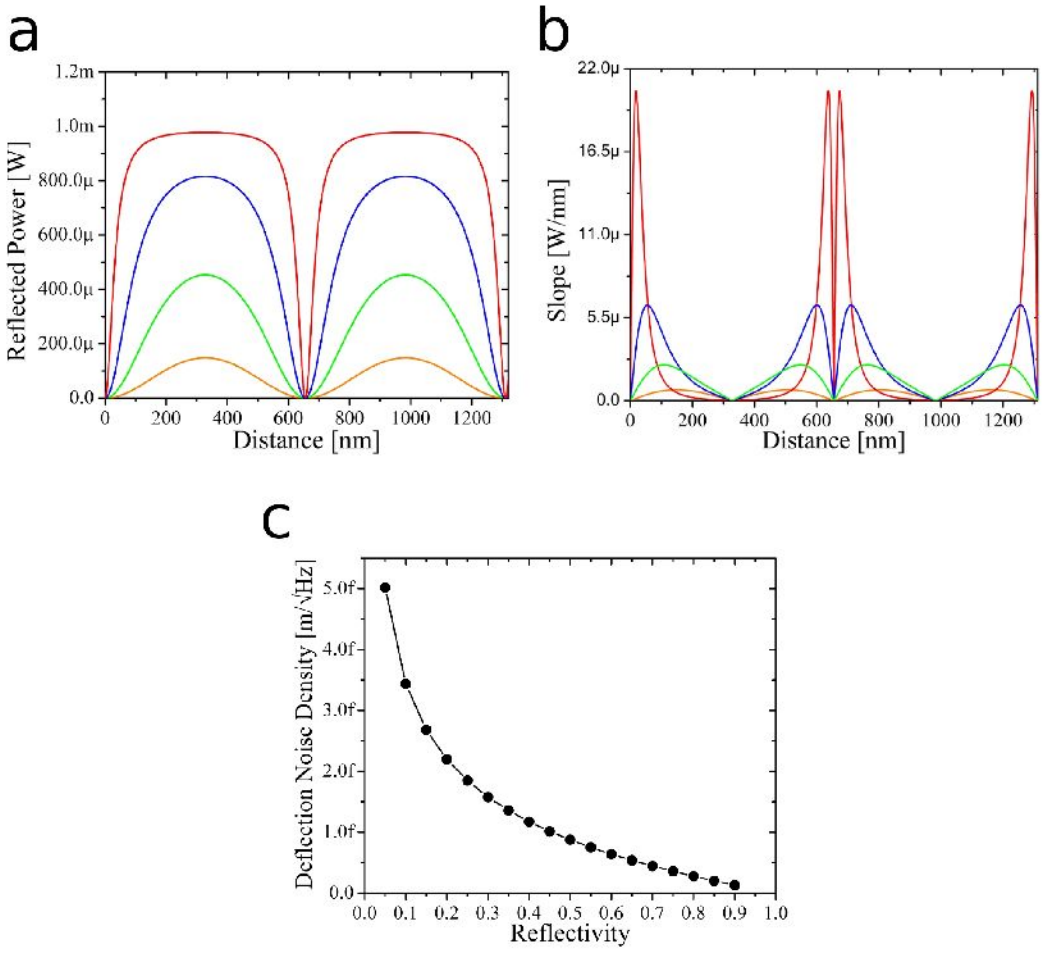

Figure 2.3. Calculated interference patterns and deflection noise densities with varying reflectivities. (a) Fringe pattern and the (b) absolute magnitude of the corresponding slope for varying R values with a P_i of 1.0 mW. The values for (a) and (b) are as follows; Red: R=0.74, Blue: R=0.40, Green: R=0.15, Orange: R=0.04. (c) The variation in deflection noise density due to the photodiode shot noise at varying reflectivities with z_{op} set to the maximum operating slope. The index of refraction for air, n=1.0, and a λ_0=1311 nm was used for all calculations.

The other parameter worthy of consideration is the operating power of the laser, or the incident power at the cavity. In **Figure 2.4a** and **2.4b** we have calculated the interference pattern and absolute value of its slope when the incident power is varied. A linear change in maximum slope occurs while z_{op} remains the same. This gives rise to a linear change in the average reflected power at the photodiode during operation whose slope is determined by the value of the periodic function, Θ, at z_{op}. The contribution of these two effects are clearly seen in Eq. (11)

where we find that for a given reflectivity and z_{op}, the deflection noise density decreases as one increases the incident power at the cavity. Although working at higher powers tends to increase the slope, it can have adverse affects on micro-machined devices such as commercial cantilevers used in AFM experiments. Increased noise from unwanted cantilever vibrations, optical damping of the cantilever, and self – oscillations can occur when the incident power on the cantilever is too large [28].

Using Eq. (11) we have plotted the deflection noise density as one varies the incident power at the cavity for R=0.004, R=0.04, and for R=0.74 and is found in **Figure 2.4c**. These values were chosen to resemble a bare fiber in water, bare fiber in air, and a reflective coated fiber in either environment, respectively. At an incident power of 1.50 mW the photodiode shot noise is calculated to be approximately 50 times higher for an uncoated fiber in water compared to an optical fiber with a reflective coating. This occurs because when the fiber is uncoated, the reflectivity of the fiber end is determined by the Fresnel reflectivity at the interface. The reflectivity is significantly reduced when submerged into a fluid due to the increase in the index of refraction of the surrounding media.

Given these considerations, optical fibers coated with a reflective coefficient of approximately 0.74 and typical incident powers of 1.00 to 1.75 mW have been chosen for practical operation. A reflective coefficient of 0.74 provides a reasonable trade-off between obtaining low deflection noise densities and slope curves that can be managed by the fiber positioning assembly feedback piezo. In addition, the slope of the interference curves provide good linearity over the oscillation amplitude ranges of 0.1 to 0.5 nm required for high resolution FM – AFM imaging. At the typical incident powers chosen, we have not observed any adverse affects on the cantilever dynamics when measured in either air or liquid environments.

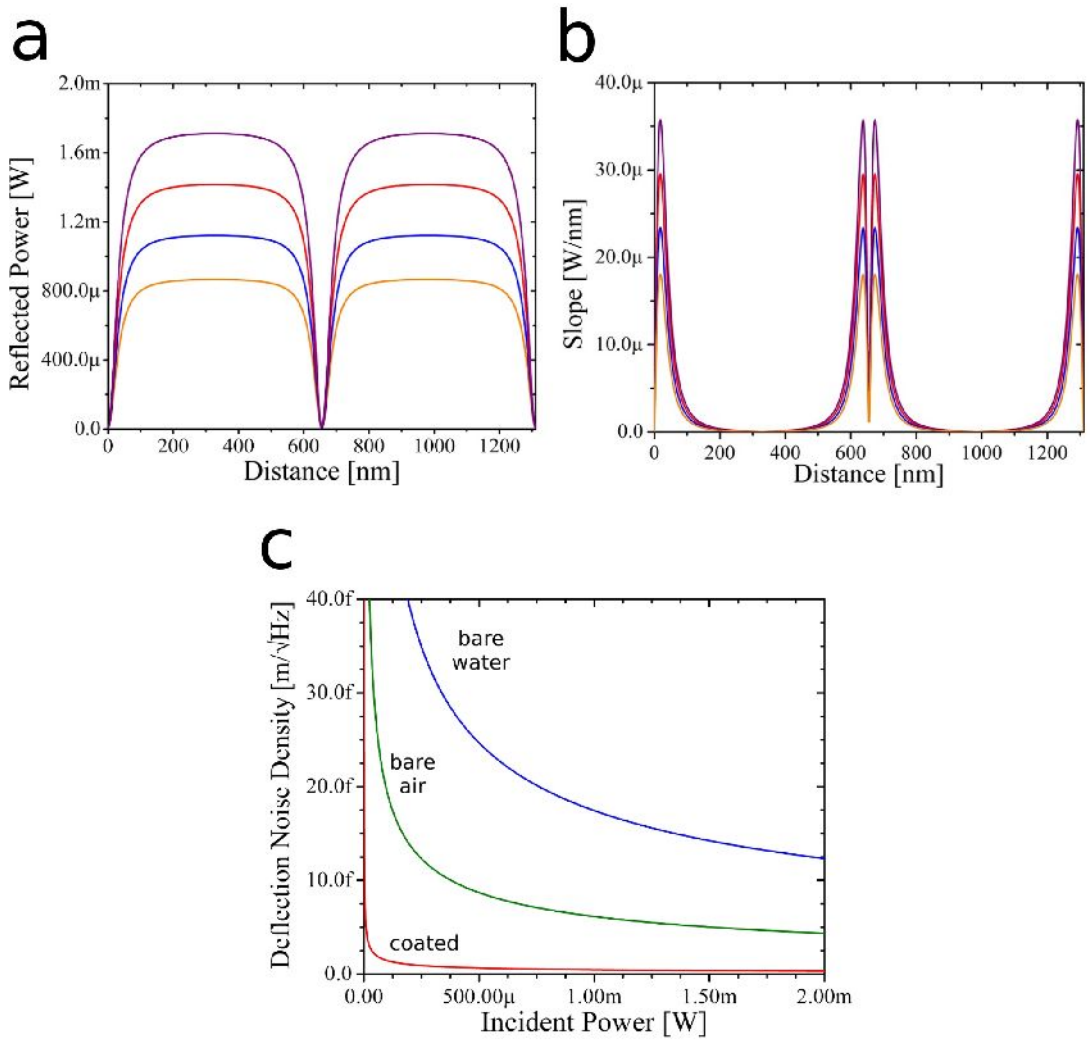

Figure 2.4. Calculated interference patterns and deflection noise densities with varying incident power. (a) Fringe pattern and (b) absolute value of the corresponding slope for varying P_i's when R=0.74. The values for (a) and (b) are as follows; Purple: P_i=1.742 mW, Red: P_i=1.440 mW, Blue: P_i=1.140 mW, Orange: P_i=0.88 mW. The index of refraction for air, n=1.0, and a λ_0=1311 nm was used for all calculations. (c) Variation of the deflection noise density due to the photodiode shot noise for three different reflectivities as the incident power is varied. Parameters for (b) are as follows; Blue: n=1.333, R=0.004, Green: n=1.0, R=0.04, Red: n=1.0, R=0.74. In all calculations λ_0=1311 nm. It is important to note that at each new reflectivity value a new z_{op} is determined and used in the calculations.

In the experimental set – up a good agreement is found with the idealized case using no focusing optics, a real light source with a peak width of approximately 0.1 nm, and imperfect reflecting surfaces of different identities. **Figure 2.5** shows a typical interference pattern generated between a cleaved fiber optic face with a dielectric coating and a silicon wafer with a 30 nm thick gold coating. The experimentally gathered raw data curves (purple) match reasonably well with the curves generated from Eqs. (1) – (4) where R=0.74 and P_i=1.74 mW. Using Eqs. (5) – (7) and the fact that our corning SMF-28 fiber has a mode field radius of 4.6 μm, operating in air (n=1) with a 1311 nm laser at a gold mirror (r_{mirror}=0.992) to fiber spacing of 30 μm we obtain an R_{eff} of 0.74 for the gold mirror. The null at 655.5 nm is a good indication that the effective reflectivity of the gold – silicon surface matches the reflectivity of the dielectric mirror coated fiber.

A series of interference patterns generated between the optical fiber and gold – silicon mirror was also measured at varying incident powers to compare to the expected sensitivity and deflection noise density described by Eqs. (8) and (11). **Figure 2.6a** and **2.6b** show the measured (black – dotted lines) and theoretical (dashed lines) sensitivity and deflection noise density, respectively, for an interference cavity operated at a distance where the slope is a maximum. The variance in the measured sensitivity with incident power in **Figure 2.6a** shows good agreement with theoretically calculated values. The measured deflection noise density shown in **Figure 2.6b** reaches values as low as 1.5 fm/√Hz and is only slightly higher than what is expected from strictly shot noise limited performance. The remaining noise can be attributed to excess laser noise at the photodetector.

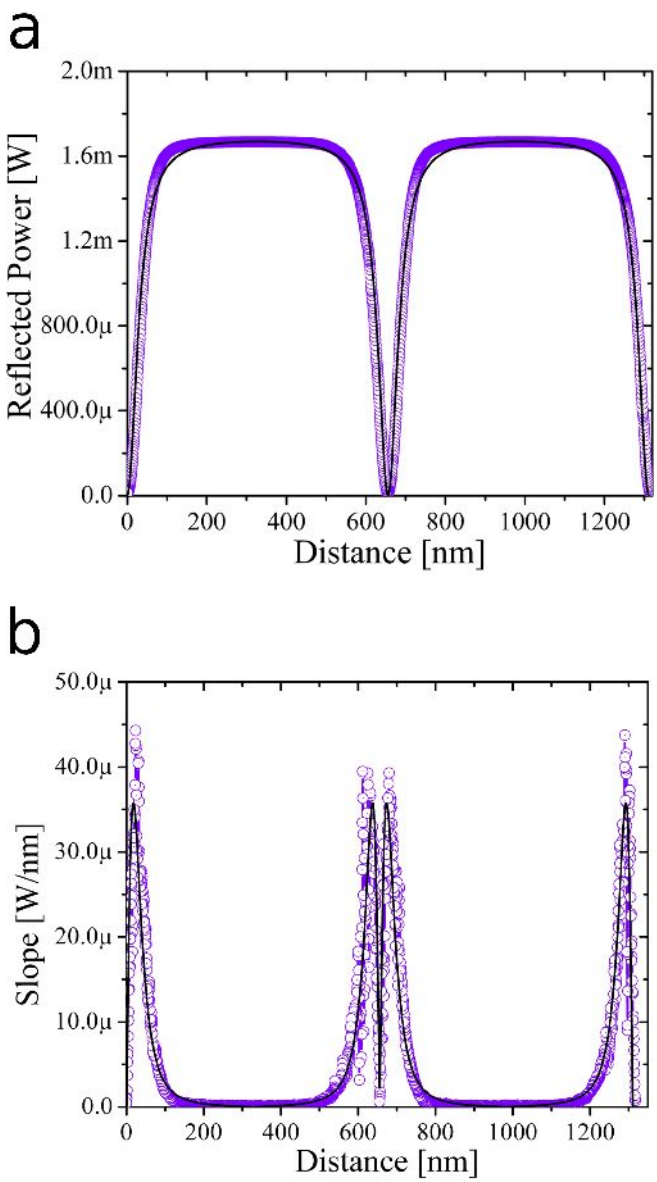

Figure 2.5. Comparison of the (a) ideal interference pattern to experimentally acquired data and the (b) absolute value of the corresponding slope obtained between a cleaved fiber optic cable with a dielectric reflective coating and a silicon wafer coated with 30 nm of evaporated gold. The parameters used for the calculation are as follows; R=0.74, P_i=1.742 mW, λ_0=1311 nm, and n=1.0.

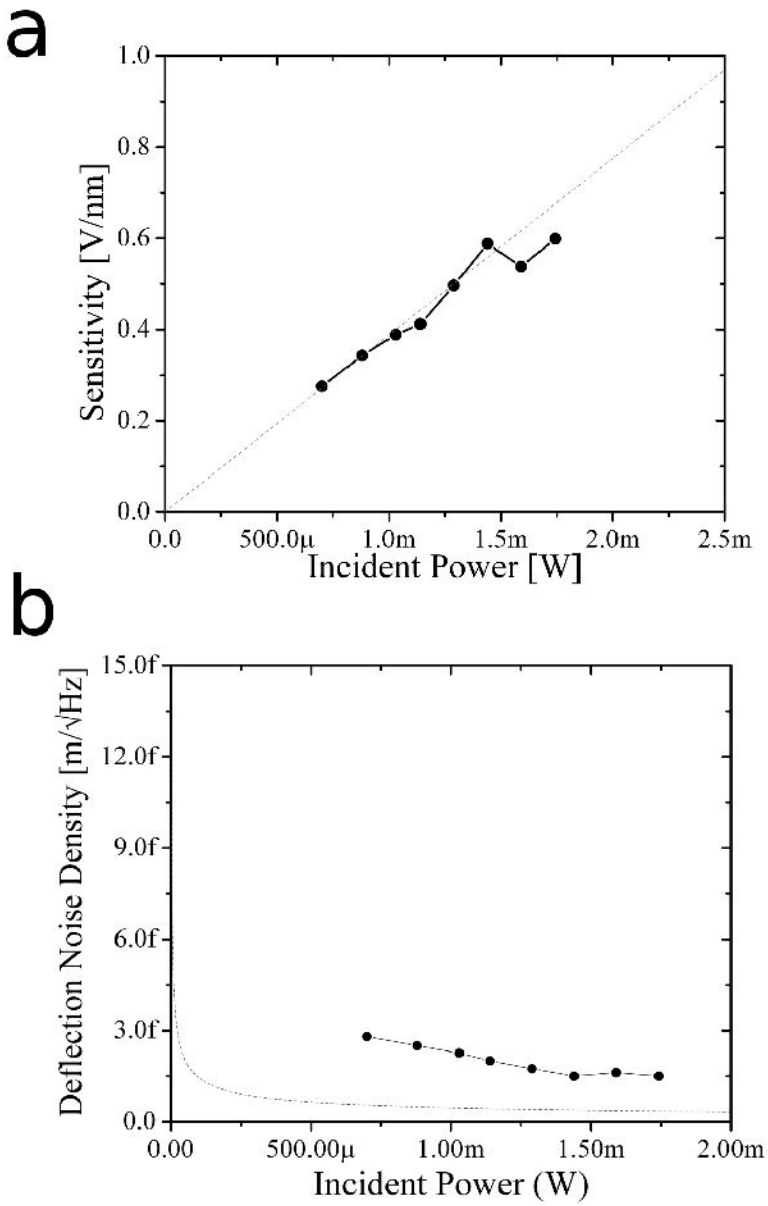

Figure 2.6. (a) Sensitivity and (b) deflection noise density at varying incident powers. The solid dotted lines (black) are the experimentally measured values and the dashed lines (gray) are calculated for an ideal interference cavity. The parameters used for the calculations are; R=0.74, λ0=1311 nm, zop=18.1 nm, n=1.0, RIV=21 kΩ, and η=0.90 A/W.

2.4. CANTILEVER DEFLECTION SENSOR

2.4.1. Ambient and Liquid Environment Interference

When a cantilever is used as a reflective surface in the FP cavity, the behavior is qualitatively similar to the ideal symmetric FP cavity. Increasing the reflectivity of the two surfaces and operating at higher powers generally gives the best sensitivities and deflection noise densities. With our deflection sensor we achieve sensitivities between 0.5 and 0.125 V/nm, which give deflection noise densities between 2 and 8 fm/√Hz, respectively. The spread in values is due to the variability in angular alignment over the cantilever end, the spacing between the two reflective surfaces, and any variability in the reflective coating between different cantilevers. When the fiber optic cable is placed over the end of the cantilever we generally obtain interference patterns that have minimum values that differ from zero and a range of different fringe visibilities, where $visibility=(i_{max}-i_{min})/(i_{max}+i_{min})$, as is expected for a FP cavity composed of two different reflective surfaces [19]. Here i_{max} and i_{min} are the maximum and minimum current output of the photodiode, respectively. The quality of the fringe pattern can be improved through proper angular alignment and careful tuning of the distance between the two reflective surfaces.

Figure 2.7 shows typical interference patterns generated between a fiber optic end face and the end of a cantilever (Nanosensors: PPP – NCHAuD) in air and after subsequent submersion in water without a change in alignment. In both cases a sweep distance of 1984.4 nm was performed in order to highlight the reduction in fringe spacing between the two different media. The degree of compression of the interference pattern is determined by the change in index of refraction when going from air (n=1.0) to water (n=1.333) due to a change in

wavelength of the light. In addition, the fringe visibility in air is slightly smaller than observed in water, since the fiber coupled power is greater for a given distance in water than in air in accordance with Eqs. (5) and (6). These two changes to the interference pattern lead to better sensitivities and deflection noise densities in water when compared to air.

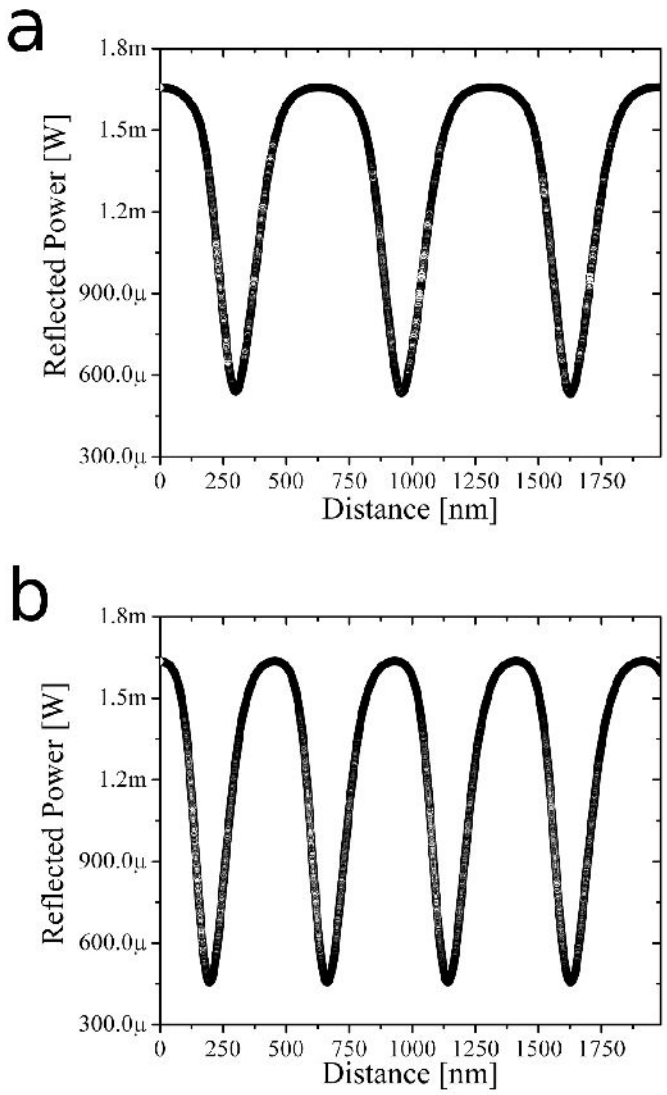

Figure 2.7. Typical interference pattern in (a) air and (b) water between a fiber optic end face and cantilever (Nanosensors: PPP-NCHAuD) backside used for FM – AFM imaging. A sweep distance of 1984.4 nm was performed in both (a) and (b). It is important to note that no change in alignment occurred between the two measurements.

2.4.2. Thermal Noise Limited Performance

The highest performance deflection sensors in AFM experimentation are limited primarily by the thermal noise of the probe oscillations. In order to obtain thermal noise limited performance, a deflection sensors noise density must be less than the noise generated by thermal Brownian motion of the cantilever. The deflection noise density generated by the thermal motion of a cantilever is given by [3]

$$n_{zB} = \sqrt{\frac{2k_B T}{\pi f_o k Q} \frac{1}{\left[1-(f/f_o)^2\right]^2 + \left[f/(f_o Q)\right]^2}} \qquad (12)$$

where f, f_0, k, k_B, T, and Q are the vibration frequency, resonant frequency of the cantilever, spring constant, Boltzmann constant, absolute temperature, and quality factor, respectively.

The developed deflection sensor is capable of obtaining thermal noise limited performance in both air and liquid environments with cantilevers that have relatively high spring constants (k = 40 – 200 N/m). The use of these stiff cantilevers is often necessary for high resolution imaging in the FM-AFM mode of operation since small oscillation amplitudes must be used to enhance sensitivity to short range interaction forces between individual atoms while avoiding "jump-to-contact" [17]. **Figure 2.8** shows the frequency spectra of a commercially available cantilever (Nanosensors: PPP – NCHAuD) in air and water. The dotted lines are the experimentally measured frequency spectra and the dashed lines are theoretically calculated spectra from Eq. (12). The amplitude of the deflection noise density near the resonance frequency is almost completely attributed to the thermal fluctuations of the cantilever in either environment.

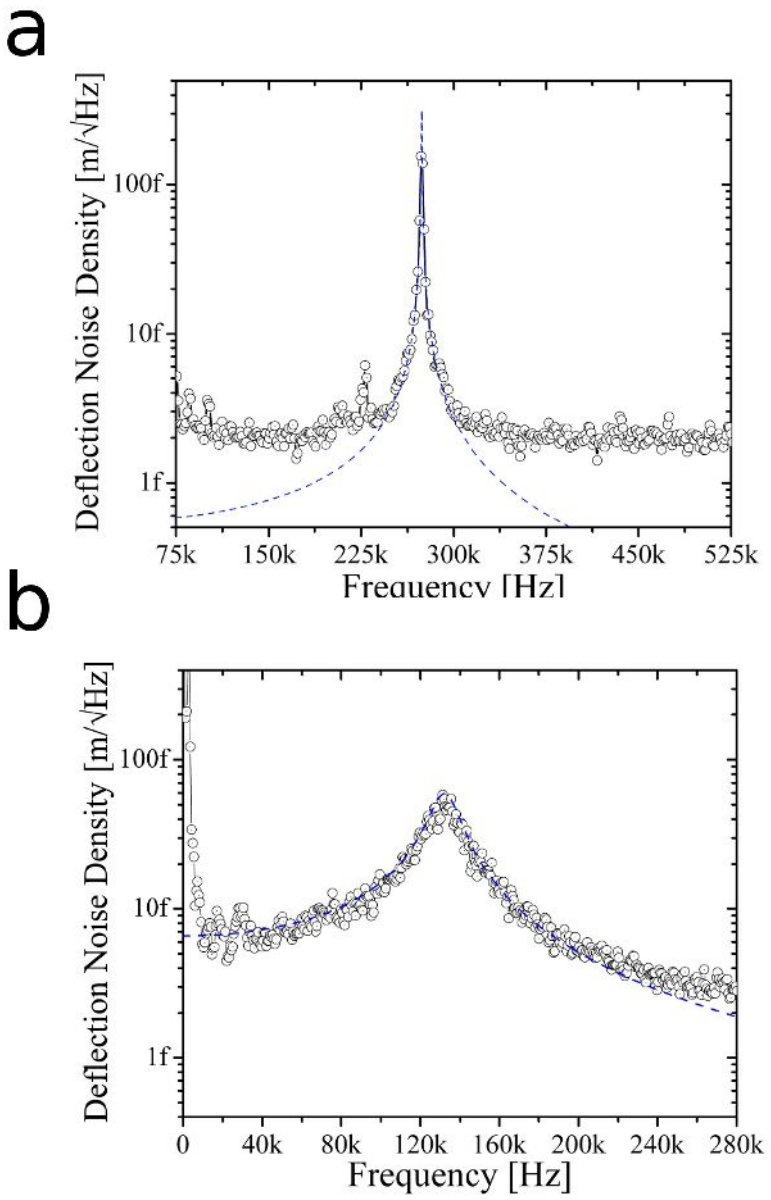

Figure 2.8. Frequency spectra of a cantilever (Nanosensors: PPP – NCHAuD) thermal Brownian motion measured in (a) air and (b) water. The dotted lines (black with white circles) are experimentally measured values and the dashed lines (blue) are theoretically calculated values using Eq. 9. The parameters used in calculating (a); k=50 N/m, f_0=274 kHz, Q=650, and T=293 K. The parameters used for (b); k=50 N/m, f_0=132.5 kHz, Q=9, and T=293 K. It is important to note that no change in alignment occurred between the two measurements.

2.5. FM – AFM IMAGING

A schematic of the experimental setup used for high resolution FM – AFM imaging is presented in **Figure 2.9**. A cleaved fiber optic cable of the deflection sensor is positioned over a commercial silicon cantilever with the manual manipulator. The optimum operating position is determined by sweeping the fiber feedback piezo at least one wavelength and finding the point where the sensitivity is a maximum. Once established, the fiber cantilever distance is maintained constant with feedback electronics. The low frequency voltage from the photodiode – preamp circuitry is monitored and fed into a digital PID controller which outputs a voltage through the controller electronics and amplified with a HV amplifier (RHK Technology: HVA 900). This amplified voltage is constantly applied to the piezo ring of the fiber positioning assembly to continuously maintain a fixed gap distance between the fiber end and cantilever backside. The AC coupled output voltage of the preamp is routed to the input of the FM detector (Nanonis: OCB – 2) for monitoring the frequency shift of the cantilever resonance. The cantilever oscillation is driven by a piezo actuator drive assembly controlled by the excitation voltage from the output of the phase locked loop (PLL) circuitry. The amplitude of the cantilever oscillation is kept constant during FM – AFM imaging with the digital feedback loop of the controller. Imaging is performed in constant frequency shift mode where the feedback electronics (Nanonis: Universal SPM Controller) keep the resonant frequency shift constant by controlling the vertical position of the sample. All voltages applied to the custom built piezo tube scanner are first generated by the control electronics and amplified (Nanonis: HVA4) depending on the desired range and sensitivity of the images. Lower amplifications of 4× are generally used for high resolution imaging, which results in a Z – range of approximately 320 nm and X,Y – ranges of about 900 nm. Lastly, the voltages on the cantilever, V_T, and sample, V_S, can be independently set

by the controller to minimize long range electrostatic interactions between the cantilever and sample.

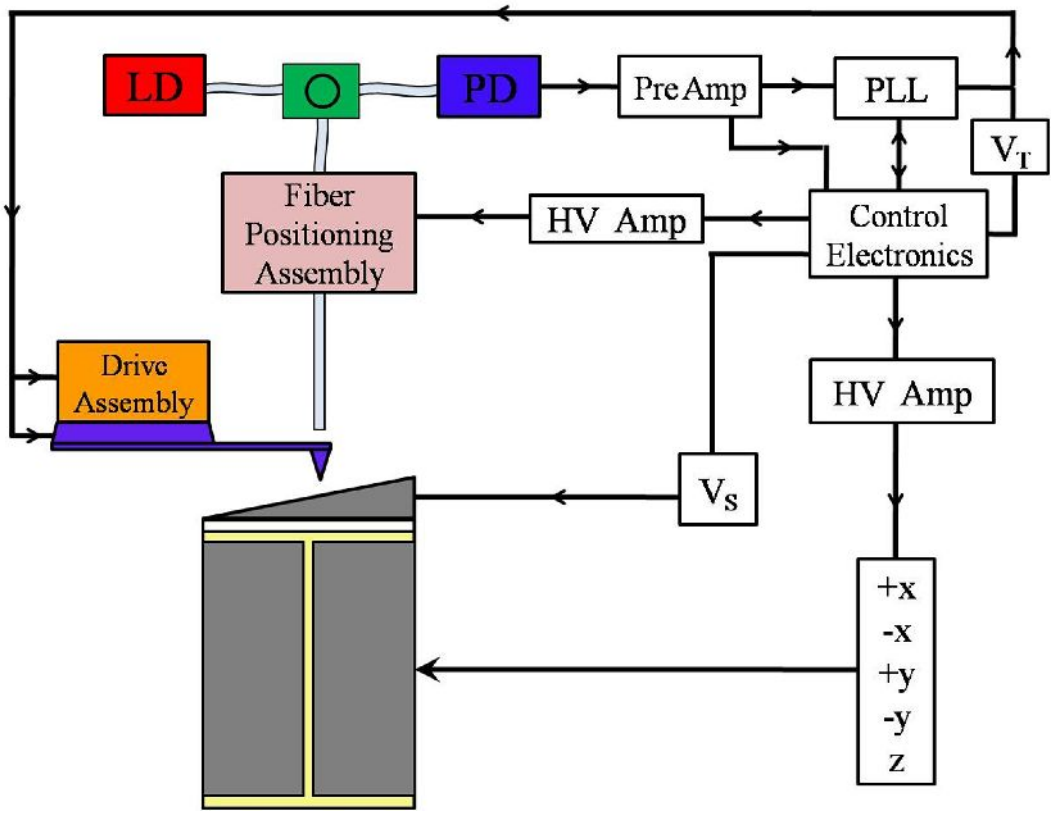

Figure 2.9. Schematic of the experimental set – up used for FM – AFM imaging using the developed fiber optic deflection sensor.

Figure 2.10 shows a high resolution FM – AFM image of muscovite mica under 18.2 MΩ water. The mica sample was mechanically cleaved under ambient conditions shortly before imaging. The characteristic hexagonal pattern previously observed for mica [9] imaged under similar conditions is clearly observed. Atomic scale variations can be seen in the image

illustrating that the developed interferometer deflection sensor is capable of true atomic resolution imaging.

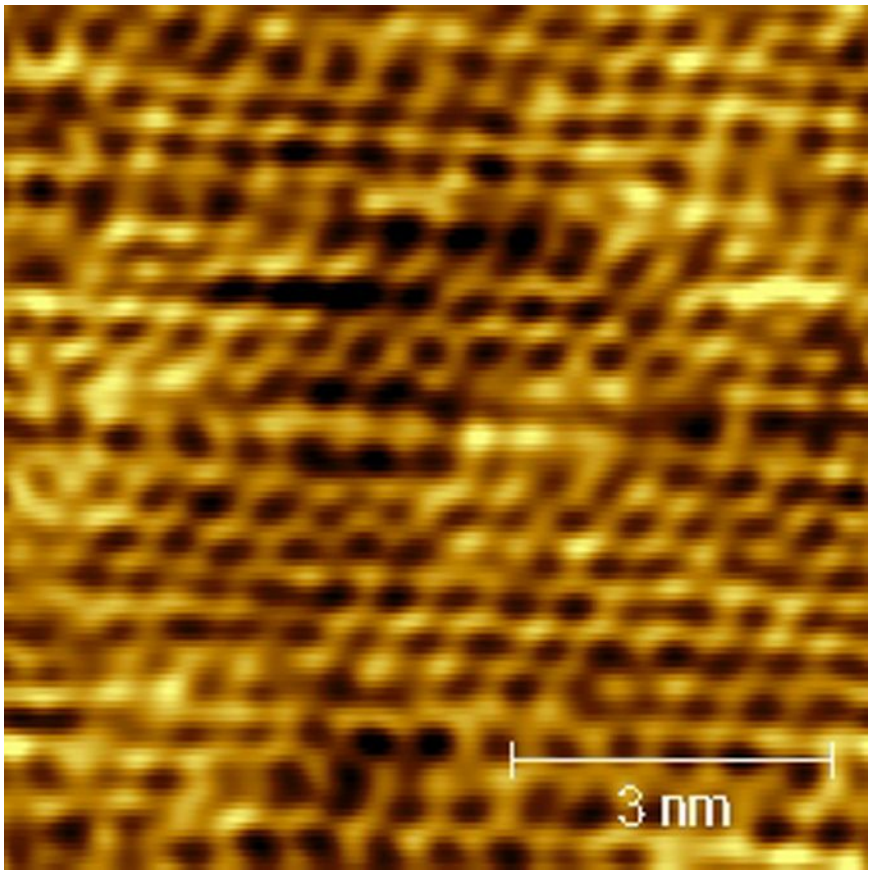

Figure 2.10. True atomic resolution FM – AFM image of muscovite mica acquired in pure 18.2 MΩ water. The image (8 nm x 8 nm, Δf= +880 Hz, A=0.275 nm, Scan Speed=533.34 nm/s) was acquired with a commercial cantilever (Nanosensors: PPP – NCHAuD).

2.6. SUMMARY

In this chapter, the development of a low noise all-fiber Fabry-Perot interferometer capable of achieving noise densities of 2 fm/√Hz on commercially available cantilevers in both ambient and liquid environments is discussed. A description of the critical components is

provided along with the design of a simple fiber positioning assembly used for rapid alignment of a fiber optic end face over a cantilever to generate an interference cavity. A description of an ideal interference cavity is presented in order to understand how the reflected light at a photodiode varies with the distance between a fiber and mirror. The reflectivity of the cavity and the incident power are presented as two important parameters that require consideration when optimizing such a deflection sensor. Increasing the reflectivity and incident power were shown to decrease the deflection noise density due to photodiode shot noise. While the discussion considers an interference cavity comprised of identical reflectors, the expression derived for the deflection noise density and considerations for optimization are general and can be applied to more rigorous models. The interference patterns generated between a dielectric mirror coated optical fiber and commercial cantilever in air and water are presented along with the measured deflection noise densities when the fiber is positioned to achieve maximum sensitivity to displacement. Finally, true atomic resolution FM – AFM imaging of muscovite mica in water is demonstrated using the developed sensor.

2. 7. REFERENCES

[1] G. Binning, C. F. Quate, and C. Gerber, Phys. Rev. Lett. 56, 930 (1986).

[2] F. J. Giessibl, Science 267, 68 (1995).

[3] T. R. Albrecht, P. Grütter, D. Horne, and D. Rugar, J. Appl. Phys. 69, 668 (1991).

[4] L. Gross, F. Mohn, P. Liljeroth, J. Repp, F. J. Giessibl, and G. Meyer, Science 324, 1428 (2009).

[5] S. Torbrügge, M. Reichling, A. Ishiyama, S. Morita, and Ó. Custance, Phys. Rev. Lett. 99, 056101 (2007).

[6] L. Gross, F. Mohn, N. Moll, P. Liljeroth, and G. Meyer, Science 325, 1110 (2009).

[7] T. Fukuma, T. Ichii, K. Kobayashi, H. Yamada, and K. Matsushige, Appl. Phys. Lett. 86, 034103 (2005).

[8] T. Fukuma, K. Kobayashi, K. Matsushige, and H. Yamada, Appl. Phys. Lett. 86, 193108 (2005).

[9] T. Fukuma, K. Kobayashi, K. Matsushige, and H. Yamada, Appl. Phys. Lett. 87, 034101 (2005).

[10] T. Fukuma, M. J. Higgins, and S. P. Jarvis, Biophys. J. 92, 3603 (2007).

[11] B. W. Hoogenboom, K. Suda, A. Engel, and D. Fotiadis, J. Mol. Biol. 370, 246 (2007).

[12] T. Fukuma, M. J. Higgins, and S. P. Jarvis, Phys. Rev. Lett. 98, 106101 (2007).

[13] F. J. Giessibl, Appl. Phys. Lett. 46, 1470 (2000).

[14] G. Meyer and N. M. Amer, Appl. Phys. Lett. 53, 1045 (1988).

[15] D. Rugar, H. J. Mamin, R. Erlandsson, J. E. Stern, and B. D. Terris, Rev. Sci. Instrum. 59, 2337 (1988).

[16] T. Fukuma, K. Kobayashi, K. Matsushige, and H. Yamada, Rev. Sci. Instrum. 76, 053704 (2005).

[17] F. J. Giessibl, Rev. Mod. Phys. 75, 949 (2003).

[18] B. W. Hoogenboom, H. J. Jug, Y. Pellmont, S. Martin, P. L. T. M. Frederix, D. Fotiadis, and A. Engel, Appl. Phys. Lett. 88, 193109 (2006).

[19] B. W. Hoogenboom, P. L. T. M. Frederix, J. L. Yang, S. Martin, Y. Pellmont, M. Steinacher, S. Zach, E. Langenbach, and H. J. Heimbeck, A. Engel, and H. J. Hug, Appl. Phys. Lett. 86, 074101 (2005).

[20] D. Rugar, H. J. Mamin, and P. Guethner, Appl. Phys. Lett. 55, 2588 (1989).

[21] A. Z. Stieg, H. I. Rasool, and J. K. Gimzewski, Rev. Sci. Instrum. 79, 103701 (2008).

[22] Applied Optoelectronics, Inc., 13115 Jess Pirtle Blvd., Sugar Land, TX. 77478, USA.

[23] OZ Optics Ltd., 219 Westbrook Rd., Ottawa, Ontario, K0A 1L0, Canada.

[24] PD – LD Inc., 30 – B Pennigton – Hopewell Road, Pennigton, NJ. 08534, USA.

[25] M. Born and E. Wolf, *Principles of Optics* (Cambridge University Press, New York, Seventh (expanded) Edition, 1999).

[26] S. Nemoto and T. Makimoto, Opt. Quant. Electron. 11, 447 (1979).

[27] T. Fukuma and S. P. Jarvis, Rev. Sci. Instrum. 77, 043701 (2006).

[28] H. Hölscher, P. Milde, U. Zerweck, L. M. Eng, and R. Hoffmann, Appl. Phys. Lett. 94, 223514 (2009).

CHAPTER 3

UNDERSTANDING GRAPHENE GROWTH ON COPPER

3.1. INTRODUCTION

Graphene, an infinite two dimensional network of carbon atoms, has captivated the attention of researchers with its unique electronic [1,2] and mechanical properties [3,4,5]. Suspended and specially supported graphene have shown extraordinary electron mobility through this exotic material [6,7,8]. In addition to an incredible mechanical strength, recent results have shown strong adhesive properties and impermeability to even the smallest of gas molecules [9, 10]. While fundamental studies of these properties are invaluable in their own right, and essential to the progress of the field, a great deal of effort has also been made to fabricate practical devices from this material [11,12]. One promising avenue is the development of electronic devices that can be modulated with very high frequencies [13, 14]. Mechanical resonators made from suspended graphene structures can be used in nanoelectromechanical systems (NEMS) applications [15 – 18].

In order to generate practical devices made from graphene, methods for mass (commercial) production must be developed. One promising route for graphene production is the thermal decomposition of carbon containing gases in the presence of metal catalysts. Traditional surface science studies have focused on growth on metal single crystals such as Ir (111) [19], Pt (111) [20], Ru (0001)[21], Au (111) [22], Cu (111) [23], and Cu (100) [24]. Recently, the remarkable growth of large area graphene on polycrystalline copper foil has also been accomplished [25]. The reaction is found to occur on the surface without significant diffusion into the bulk and is self limiting (growth terminates after the copper surface is covered with graphene) [26]. While the graphene is shown to be continuous over the entirety of the copper surface and can grow across grain boundaries within the underlying copper, the resulting monolayer of graphene is polycrystalline in nature [27, 28]. Each of the different crystallographic orientations of graphene confined to the plane of the sheet is stitched together by carbon

structures that depart from the characteristic hexagonal bonding. These carbon structures are composed of pairs of pentagons and heptagons and are expected to dramatically influence the electronic and mechanical properties of the grown material [29 – 33]. Although, recent work has shown that very large single crystal regions, greater than 100 μm^2 in size, can be obtained on a copper substrate [34], further understanding of the growth mechanisms may allow for generation of single crystals on the scale of meters as has been accomplished for silicon single crystals.

In this chapter, the growth of graphene on polycrystalline copper foils by CVD is discussed in great detail. An analysis of growths where graphene is allowed to grow over the entire surface of a copper substrate is provided. In order to gain information about the nucleation process and early stages of growth, a series of experiments were performed where reactions were quenched at different temperatures and times through a rapid cooling of the reaction vessel. A variety of scanning electron microscope (SEM) images are presented where different graphene island morphologies exist on the surface of distinct grains of the polycrystalline copper foil. The rate of reaction propagation and growth morphology are shown to be dependent on the temperature at which the reaction is carried out. The graphene grown over the entire surface or the partial growth of graphene islands can be transferred from the copper metal catalysts to arbitrarily chosen receiving substrates. SEM images of the transfer of different graphene samples to substrates comprised of a 300 nm SiO_2 layer grown on a Si wafer reveal the high fidelity of the developed technique. By modifying the last steps of the transfer, it is possible to create suspended membranes of graphene. Creating these suspended structures opens the possibility for studying the intrinsic properties of graphene or constructing devices such as chemical sensors or nanometer scale resonators. The graphene membranes are shown to be robust, enabling AFM imaging over the one atom thick sheet and TEM analysis of their crystalline structure. Lastly, the fabrication of graphene coated AFM probes from evaporated copper thin films on SiO_2 – Si

wafers is discussed.

3.2 GRAPHENE GROWTH ON COPPER

The chemical vapor deposition (CVD) synthesis of graphene on copper substrates can be accomplished at either ambient or low pressures. All synthetic experiments of graphene for this work was done at low pressures, primarily to avoid the use of argon which is often used as the diluting medium for ambient pressure growth. In addition, the use of a low pressure set-up for synthesis does not preclude the possibility of performing ambient pressure growths. To accomplish low pressure growth of graphene, a carbon containing gas, methane in this case, is flowed over a copper substrate heated in a tube furnace in the presence of a hydrogen gas flow. The hydrogen acts to aid in the degradation of the methane gas generating active carbon species at the metal surface. These carbon species ultimately react to form a continuous layer of graphene over the entire metal surface.

In a typical CVD growth of graphene, the copper is placed in the center of the tube furnace and pumped down to a pressure of approximately 10 mTorr. Pure hydrogen gas is then flowed in the tube furnace at a typical flow rate of 2 – 5 sccm and a pressure of 50 – 250 mTorr. The pressure is monitored by an upstream gauge and controlled by a downstream valve placed directly after the furnace. The temperature of the furnace is brought to 1000 °C for annealing. The copper is then allowed to anneal for 15 to 90 minutes in order to clean the surface and remove any residual oxide that may exist on the metal surface. After annealing, the growth temperature and pressure are set. The methane is introduced to the gas inlet at a flow rate of 25 – 35 sccm. In a majority of the cases, a growth pressure of 500 mTorr is used. The growth time depends on the growth temperature, however, at a growth temperature of 1000 °C the entire copper surface is overgrown with graphene in 2 to 3 minutes. When a growth is completed, the

heating elements of the furnace are shut down, the tube furnace is opened, and a fan is placed over the tube for rapid cooling. In the first minute of cooling, the reactor tube temperature drops to 500 or 600 °C. A schematic of the CVD apparatus with its critical components highlighted is shown in **Figure 3.1**.

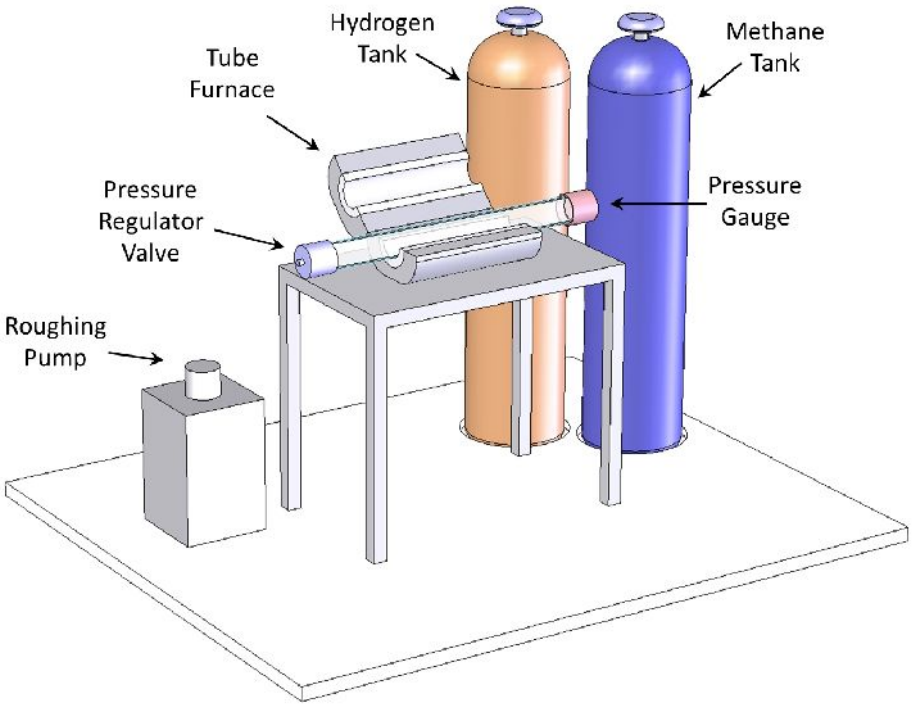

FIGURE 3.1. Schematic illustration of the CVD setup used to grow graphene. The gas tank outlets connect to flow controllers which control the flow of gas into the quartz tube. The quartz tube is translucent tube capped with the pressure gauge, highlighted in red, and with the pressure regulator valve, highlighted in light purple. The output of the regulator feeds into the roughing pump via a flexible steel tube (not shown).

The growth of graphene has been accomplished on a variety of copper substrates using this growth procedure. The most popular choice for large area graphene growth is performed on polycrystalline copper foil since it is inexpensive and can be obtained in high purity with sizes

that can be meters in size. In addition to growth on copper foil, we have accomplished growth on a variety of copper single crystal substrates. A thorough analysis of graphene grown on Copper (100) single crystals can be found in Chapter 5 of this thesis. This particular facet is of interest since the polycrystalline copper foils tend to facet with the (100) plane parallel to the copper foil surface.

A set of scanning electron microscope (SEM) images of a copper foil completely overgrown with graphene, also referred to as a "full growth," can be found in **Figure 3.2**. In the large area image of the copper surface a variety of contrasts can be observed due to the different grains scattering of the electron beam. Some grains can be as large as 100 x 100 μm. Upon imaging at higher magnifications a variety of features become apparent. Growth of graphene over the copper substrate appears to be uninhibited by the presence of grain boundaries within the underlying copper. **Figure 3.2b** shows the coalescence of four copper grains after the growth of graphene. When imaging with the SEM, a variety of surface morphologies can be observed when inspecting different grains. **Figure 3.2c** shows two grains that have come together which have two distinct surface morphologies. The grain with darker contrast appears to be smoother with crescent shaped step bunches. The grain with lighter contrast has a step like pattern which run along the same direction within the grain. In addition to the different surface morphologies, dark patches and lines can be seen on the surface after graphene synthesis. The dark patches are attributed to areas where more than one layer of graphene has been grown. These dark patches are consistently observed over the entirety of samples, however, they only account for 5 to 10 % of the sample surface area. The dark lines present at the surface are generally attributed to wrinkles in the graphene overlayer, which are likely formed during the cooling over the copper substrate after growth. These wrinkles occur as a result of the different expansion coefficients of the copper and graphene. The red dashed circle and arrow in **Figure 3.2d** highlight a graphene

multilayer region on the sample and a graphene wrinkle, respectively.

While observation of the copper after growth elucidates useful information regarding the sample morphology, additional insight are gained by observing the growth at its initial stages. One method used to accomplish this is done by effectively quenching the reaction by a rapid cooling of the reaction chamber. In these experiments, the methane gas was allowed to flow for 1 to 2 minutes over the copper before the furnace is shut down, opened, and rapidly cooled with fans. A decrease of 500 °C is easily achieved in 20 to 30 seconds. Since the high temperatures are necessary for graphene sheet extension, the reaction is effectively frozen on the surface.

Large area images of graphene islands produced from a "partial growth" due to the quenching of different reactions can be seen in **Figures 3.3** and **3.4**. In these images the graphene islands appear as dark features and the surrounding copper appears lighter. This is expected since a partial copper oxidation occurs during the transfer of the grown sample from the CVD reactor to the SEM chamber for imaging. The copper oxide appears "flat" whereas the graphene islands reveal the topography of the underlying copper. This is especially evident in high magnification images acquired over the islands. It is believed that this contrast occurs as the result of the graphene protecting the copper from oxidation in air, inhibiting the formation of the amorphous oxide that diminishes surface feature contrast under the electron beam of the SEM.

Low magnification images of the copper reveal a uniform distribution of graphene islands over the entirety of the surface. Within certain grains, a unique cluster pattern is often observed

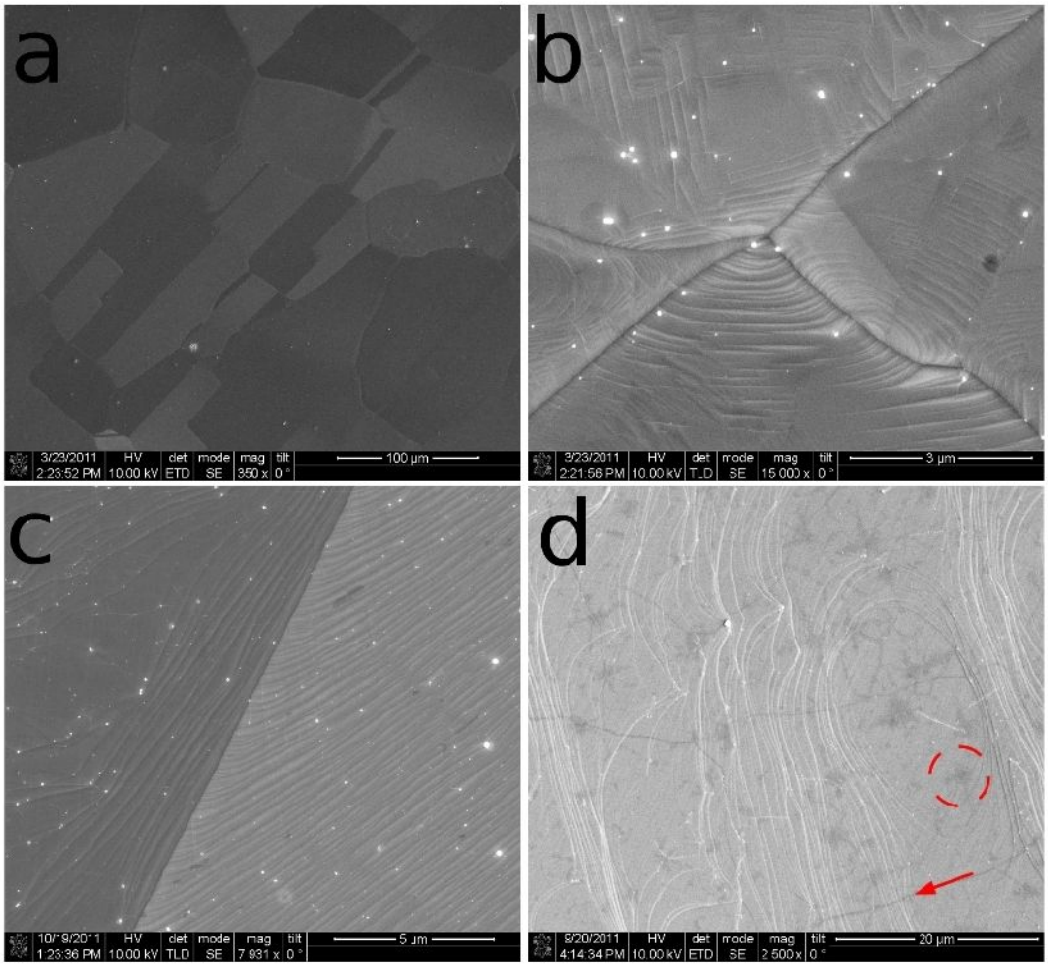

FIGURE 3.2. SEM images of graphene full growths on polycrystalline copper foils. (a) Low magnification image of different copper grains clearly observed in the foil due to grain contrast in the SEM. (b) Coalescence of four copper grains with a graphene overlayer. (c) Copper grain boundary showing different contrast and nanometer scale morphological differences in the two copper grains. (d) Flat region in a single crystal region of a copper grain. The red arrow indicates a fold in the graphene overlayer. The red dotted circle indicates a region with multiple graphene layers.

which is composed of 10 to 15 individual islands, with a cluster spacing of approximately 5 to 10 μm. The inner graphene islands of the cluster are smaller in size and are surrounded by larger islands. The observed cluster morphology may be the result of a two step nucleation process whereby nucleation of individual islands first occurs at the surface of the copper followed by the coalescence of mobile islands during the line growth of the sheets edges.

In addition to the complex nucleation patterns observed at the surface of partial growth samples, a variety of island morphologies are clearly observed over distinct copper crystal grains. While it is possible to observe similar island morphologies on different copper crystal grains as shown in **Figure 3.3a**, many copper grains create different graphene island growth morphologies. For example, in **Figure 3.3c** four different growth characteristics are present over the five different copper crystal grains imaged. When the island growth crosses one of the distinct copper grains, the morphology of the neighboring grain appears to dominate. The first growth pattern is that depicted in **Figure 3.3b**. The second growth pattern is characterized by isolated hexagonal graphene islands without signs of cluster formation. A third pattern, which is often observed and has been studied extensively, is the four lobed island morphology shown in **Figure 3.3d** and **Figure 3.4b**. These islands are associated with the growth over a well aligned copper (100) surface which is parallel to the face of the copper substrate. The last growth mode shown in **Figure 3.3** closely resembles the clustered island growth previously described, but in this particular instance the graphene islands have a distinct anisotropic extension. This slight alteration in the island shape may be the result of the copper having an anisotropic atomic corrugation characteristic of a high index facet. Additional graphene island morphologies are shown in **Figure 3.4** for completeness.

The four lobed graphene islands that are often observed on polycrystalline copper foils are believed to be the result of diffusion limited sheet extension on a copper (100) surface. A high magnification image of an isolated island is shown in **Figure 3.5a**. Each arm of the island is approximately the same length, with smaller extensions protruding perpendicular to the larger arms. This growth modality is reminiscent of the three dimensional diffusion limited fractal growth seen in the electro deposition of metals from solution. Upon close inspection of the

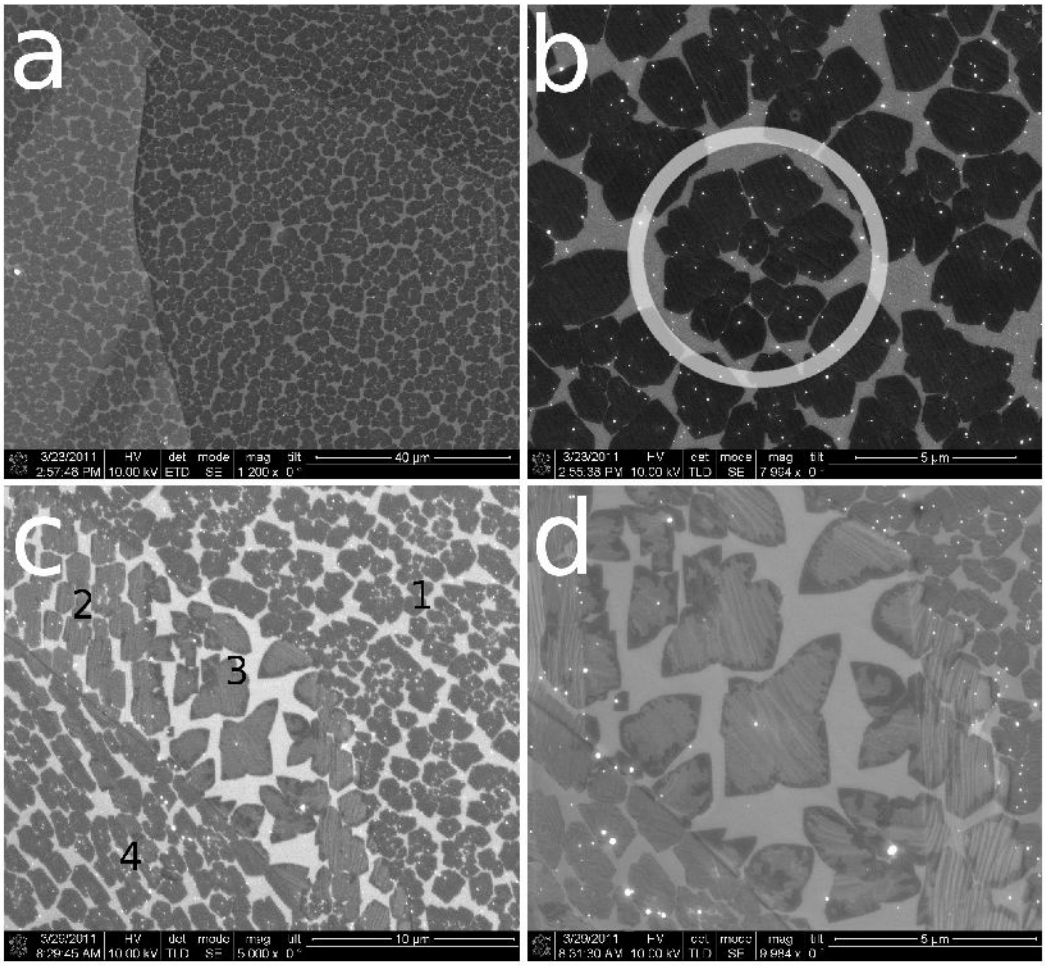

FIGURE 3.3. SEM images of graphene partial growth on a polycrystalline copper foil. (a) Low magnification image of different copper grains of the foil with similar graphene island growth morphology on each grain. (b) A high magnification image of graphene growth morphology from (a) illustrating the unique cluster formation often observed on such samples. (c) Image illustrating different copper grains of the copper foil producing distinct graphene island growth morphologies. Four distinct growth patterns are observed on the five copper grains present in the image. (d) High magnification image of the typically reported four lobe graphene islands observed on copper foils.

copper background, there exists striations in the copper which are oriented 90 degrees with respect to each other and 45 degrees with respect to the four lobes of the graphene island. This is likely the result of the graphene lobes oriented along the {100} directions of a copper (100) crystal plane present at the surface. When multiple islands nucleate in close proximity along the

surface, the arm lengths close to neighboring islands appear significantly shorter in length. Since each growing island is competing for active carbon species at the surface, a slowed growth rate results in the region between islands. A set of three closely spaced islands with asymmetric arm lengths is shown in **Figure 3.5b**.

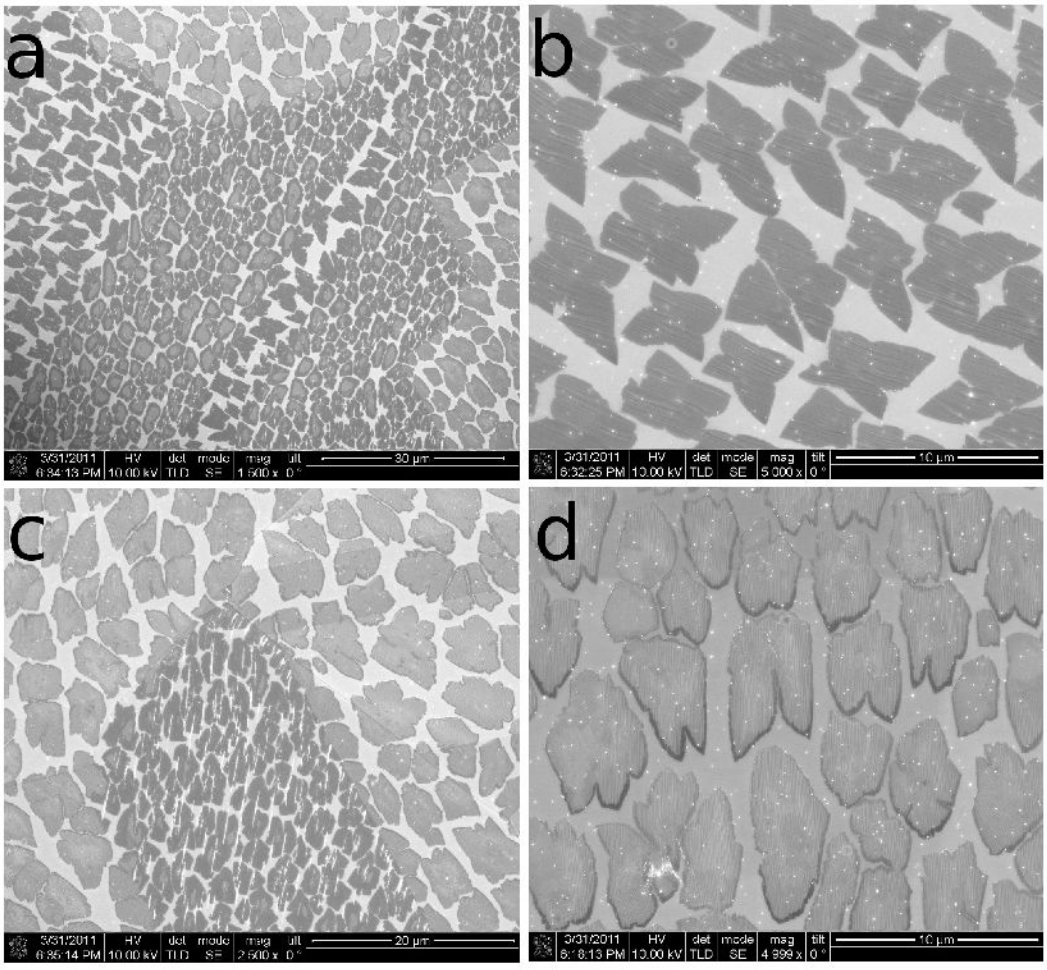

FIGURE 3.4. SEM images of graphene partial growth on a polycrystalline copper foil. (a) Low magnification image of different copper grains of the foil with different graphene island growth morphologies. (b) A high magnification image of graphene growth morphology from (a) illustrating the four lobed structure of commonly reported graphene islands. (c) Image illustrating different copper grains of the copper foil producing distinct graphene island growth morphologies. (d) High magnification image of graphene islands containing multiple lobes.

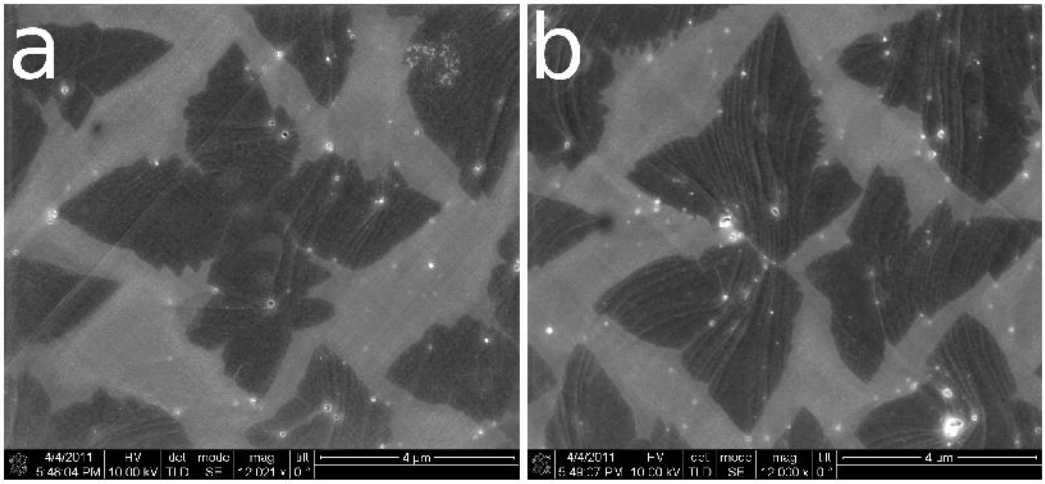

FIGURE 3.5. SEM images of graphene islands with a four lobe morphology. (a) High magnification image of an isolated graphene island. The island has a symmetric morphology due to its distance from neighboring islands. (b) High magnification image of three graphene islands which appear to have nucleated near each other on the surface. The oblique morphology is attributed to a depletion of active carbon species in the inter-island space during growth.

In order to qualitatively understand how the graphene growth is affected by temperature, partial growths were performed at different temperatures and allowed to proceed until 70 to 80 percent of the surface had been covered with graphene. **Figure 3.6** shows the SEM images of partial growths performed at 1000, 950, 800, and 750 °C for 1, 2, 6, and 15 minutes, respectively. The resulting morphologies at 1000 and 950 °C are similar and show the same morphological dependence on different copper grains as seen in **Figure 3.3** and **3.4**. At the growth temperatures of 800 and 750 °C, graphene islands show similar irregular shaped islands over the various copper crystal grains. This lack of dependence on the underlying copper structure may be the result of island growth which is not diffusion limited as would be expected at the higher temperatures.

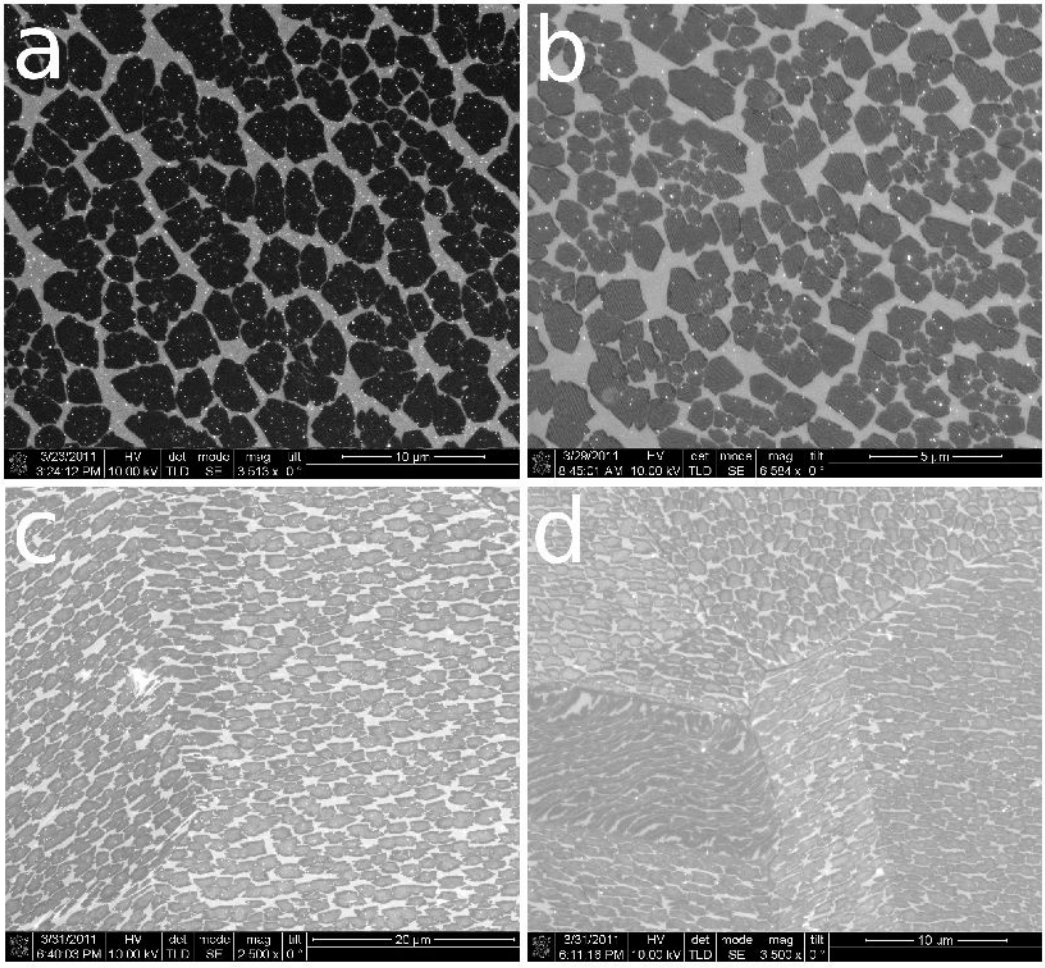

FIGURE 3.6. SEM images of graphene partial growths at different temperatures and times. The partial growths were performed at (a) 1000 °C for 1 minute, (b) 950 °C for 2 minutes, (c) 800 °C for 6 minutes, and (d) 750 °C for 15 minutes.

3.3 POST PROCESSING OF CVD GRAPHENE

Once graphene growth has been accomplished, removal of the grown material from the surface is required to further characterize its electronic and mechanical properties or produce functional devices. **Figure 3.7** provides a schematic illustration of the steps required to transfer graphene from the copper to a receiving substrate. After graphene has been grown, the first step in the transfer process is the spin coating of a liquid which contains a dissolved polymer onto the copper. A typical polymer used for this purpose is poly(methyl methacrylate), referred to as

PMMA. It can produce uniform films which are 100 to 200 nm thick when applied and spun at 3000 to 4000 rpm. After the film is applied, the solvent, in this case anisole, is allowed to evaporate under ambient temperature and pressure. The copper is then etched with a $FeCl_3$ – HCl aqueous mixture by floating the copper foil on the solution with the uncoated side in contact with the solution. A 25 μm thick foil dissolves in less than 10 minutes, leaving behind the PMMA – graphene film at the liquid surface. The film is transferred to a bath of deionized water and then to a bath of dilute aqueous HCl. The film is again transferred into a new deionized water bath for a final rinse. Lastly, the receiving substrate is then lowered in the water bath and the film is pulled onto the substrate as it is withdrawn from the water bath. After allowing to sit for 20 minutes on a hot plate at 40 °C to enhance film adhesion, the PMMA is dissolved in acetone as a final step in the transfer process.

The method described, produces high quality graphene films on a variety of substrates and can be used to transfer full or partial coverage growths. **Figure 3.8** shows SEM images taken of full and partial growth samples transferred to 300 nm SiO_2 layers grown on Si wafers, this is the "classic" receiving substrate for optical visualization of graphene. **Figure 3.8a** was taken over the corner of a transferred film from a full growth. Again, the darker contrast is due to the graphene and the light colored background is the SiO_2 surface. Upon closer inspection of the graphene, noticeable tears can be seen in various regions of the film. However, with further process development and engineering, it should be possible to reduce the frequency of these features. In addition, there exist regions on the sample which are free of tares over 5 to 10 μm^2, which is sufficient for further studies of the material properties. A partial growth transfer is shown in **Figure 3.8c** and **3.8d**. The transfer of the partial growth clearly illustrates the fidelity with which the graphene can be removed from the copper substrate. Over a 100 square micron

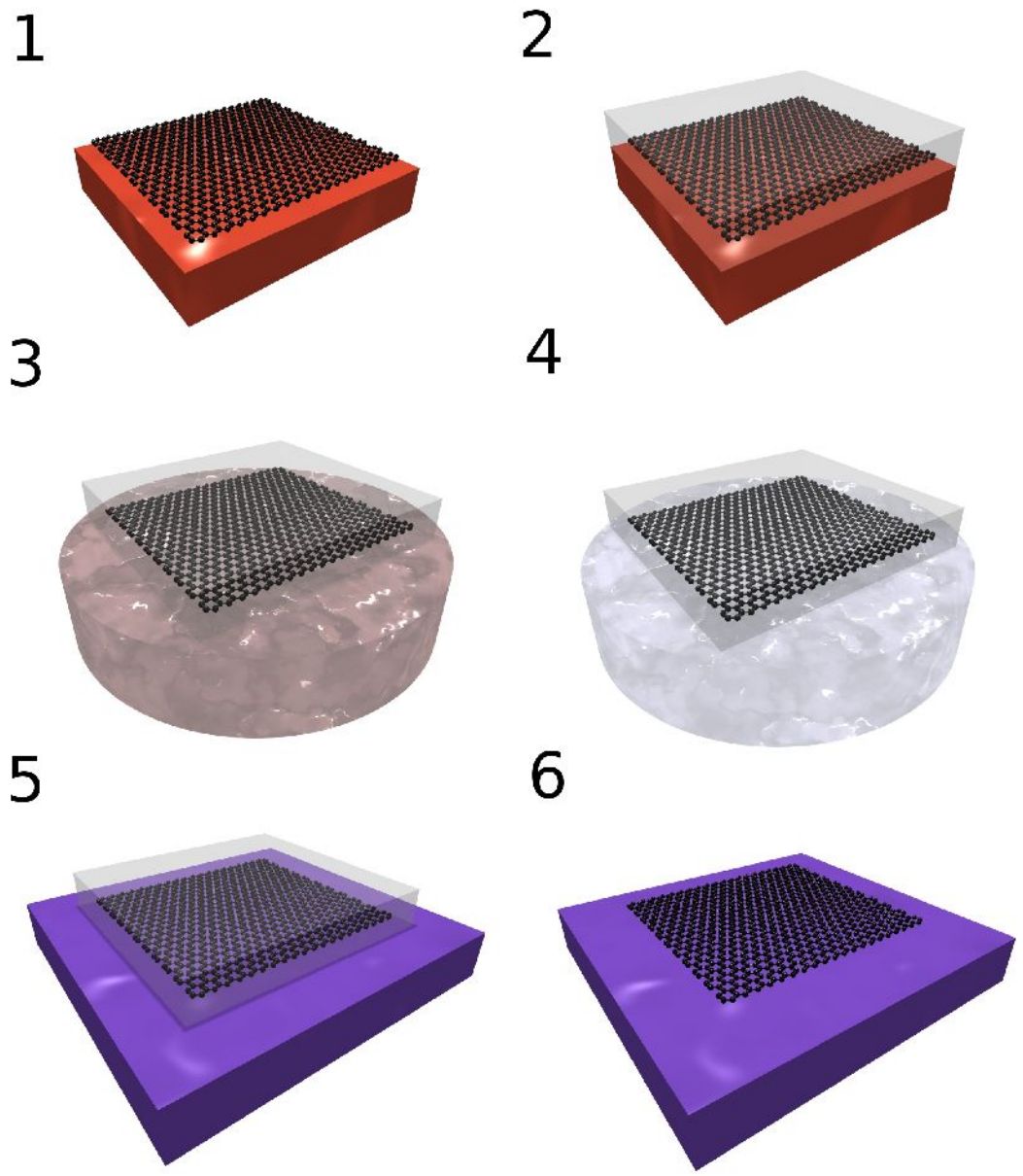

FIGURE 3.7. Schematic illustration of the transfer process for removal of grown graphene from copper to receiving substrate. Starting with grown graphene (1) a PMMA thin film is spun onto the copper (2). A desired size of graphene is cut and dissolved in a copper etchant bath (3). The film is then rinsed in aqueous HCl and water baths (4). The released graphene – PMMA film is placed onto a receiving substrate (5). The receiving substrates (shown in purple) is finally rinsed with acetone to remove the PMMA resist for a final isolation of the graphene sheet (6).

area, the transfer effectively maintains the islands positions and orientations as they exist on the copper. In the regions where two copper grains join in the substrate, the graphene islands often

appear distorted or wrinkled. This may be the result of the roughness of the interface between copper grains. The high magnification image in **Figure 3.8d** depicts the transfer of a region similar to that observed in the fourth marked region in **Figure 3.3c**.

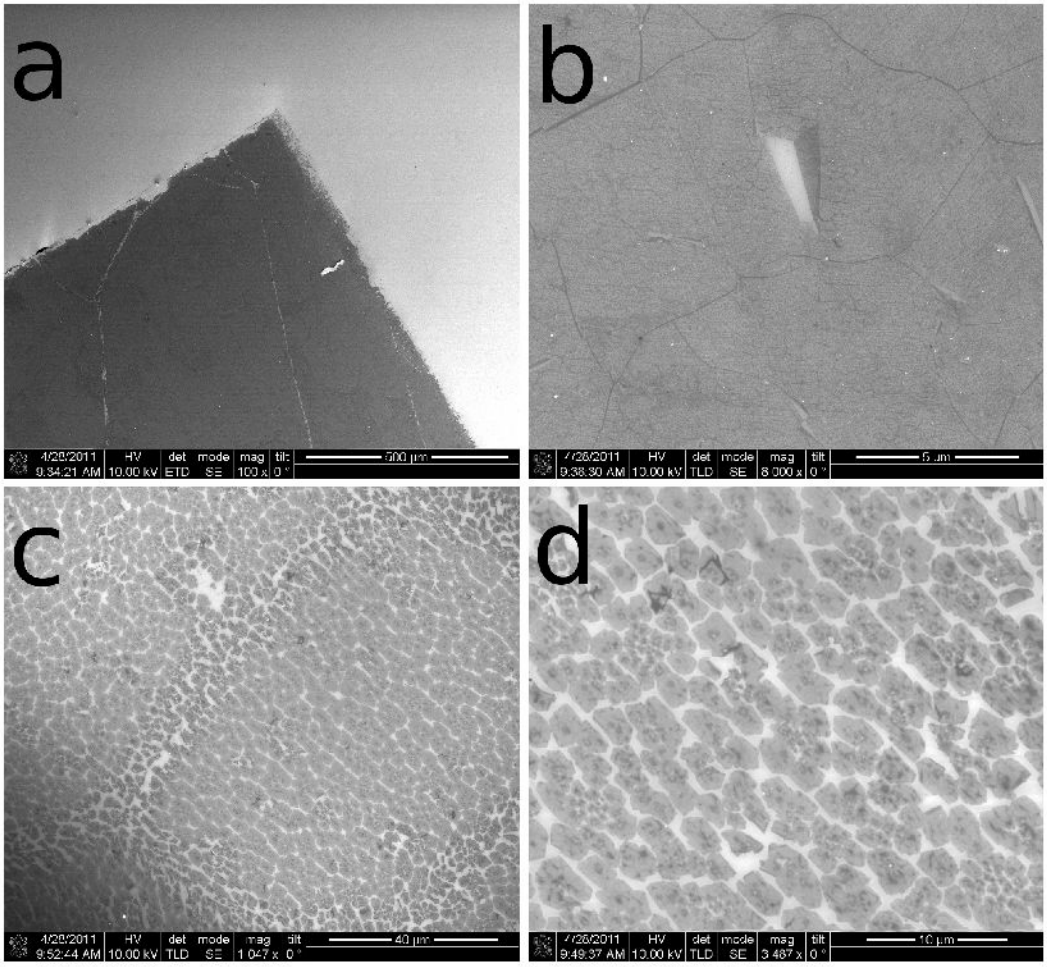

FIGURE 3.8. SEM images of the transfer of graphene to a 300 nm SiO_2 layer on a Si wafer. (a) Large area image of a corner of a full growth graphene film. (b) High magnification image of a small tare in the full growth film. (c) Large area image of transferred graphene islands. (d) High magnification image of graphene islands.

For study of the intrinsic mechanical or electrical properties of graphene it is useful to suspend the graphene over holes or trenches in order to remove substrate affects. A simple way to accomplish this is by using thin layers of PMMA followed by a "dry" removal of the polymer by

heating in air or a low pressure Ar – H_2 flow in the temperature range of 350 – 400 °C, rather than the acetone dissolution described previously. This dry heating allows for the decomposition of the PMMA without the deleterious affects of solution surface tension. This method was used

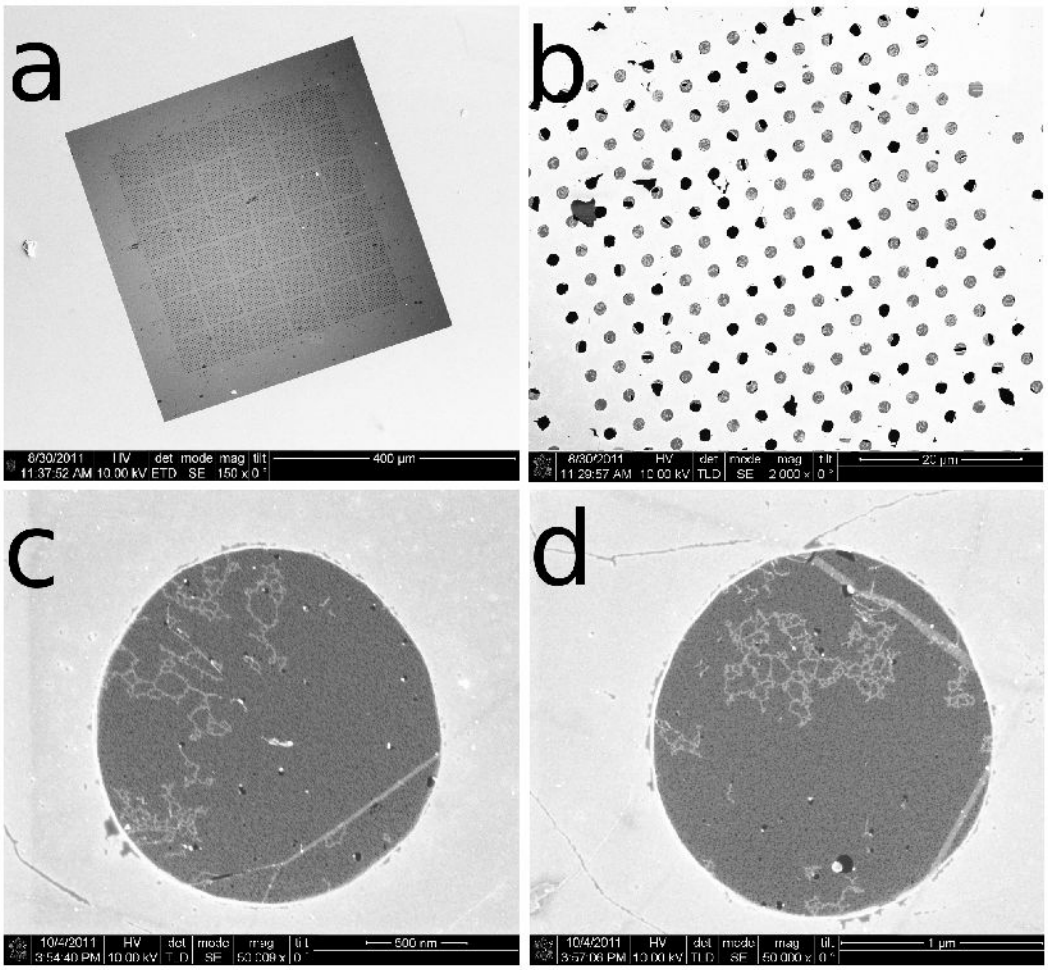

FIGURE 3.9. SEM images of graphene transferred to a perforated TEM window. (a) Large area image of a TEM window sample. (b) A zoom in image of one of the 15 by 15 array of holes. The light gray holes have suspended graphene membranes over the holes. Black holes correspond to ruptured graphene membranes. (c) and (d) High magnification images of two graphene membranes completely covering the 2 micron holes in the TEM window.

to suspend graphene over holes present in different transmission electron microscope (TEM) windows. Images acquired with the SEM of one of these samples are presented in **Figure 3.9**. The total window contains about 10,000 holes, each with a diameter of 2 μm. **Figures 3.9c** and

3.9d show two exemplary graphene membranes present in the window. The white string like material is attributed to residual polymer left from the transfer process.

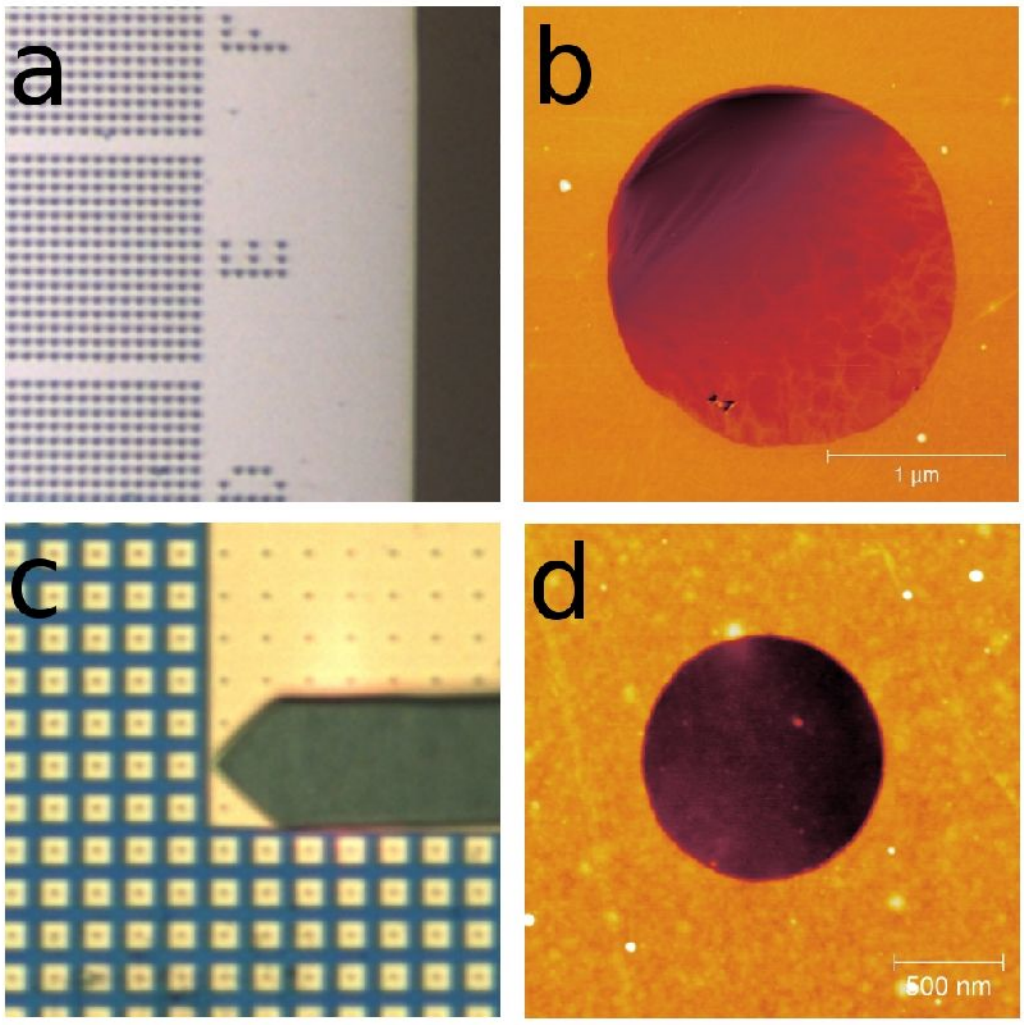

FIGURE 3.10. Characterization of graphene transferred to a perforated TEM window. (a) Optical image of a TEM window sample. The spacing between holes is 4 microns. (b) An AFM height image of a 2 micron graphene membrane. The pair of black spots at the base of the membrane are small holes in the graphene membrane. The height scale is 72 nm. (c) Optical image of an AFM cantilever probe during imaging of a 1 micron graphene membrane. The spacing between holes is 12 microns. (d) A 1 micron graphene membrane present in a perforated TEM window. The height scale is 25 nm.

The graphene membranes prepared in this manner are mechanically robust and can be imaged with an AFM to observe topographical features. An optical image of a TEM window, similar to the one shown in **Figure 3.9**, as viewed in a commercial AFM is shown in **Figure 3.10a**. An AFM height image acquired over a 2 μm diameter graphene membrane is shown in **Figure 3.10b**. A pair of small holes is clearly observed in addition to any wrinkles or asymmetries in the membrane topography, which are difficult to observe quantitatively in an SEM or TEM. Smaller 1 μm holes often show more uniform suspension of the graphene and can be directly visualized with an optical microscope and AFM, as well. **Figure 3.10c** shows an optical image of a cantilever viewed from the backside in contact with the TEM window during the imaging of a suspended graphene membrane. This level of positioning accuracy and imaging enables the potential to map the local electronic or mechanical properties of suspended graphene.

In addition to imaging the suspended graphene samples prepared on the TEM windows with an SEM and AFM, it is also possible to image and study the graphene directly in a TEM. One important note with regard to TEM imaging, the graphene should be imaged at 60 – 80 kV under low electron doses in order to avoid substantial degradation of the films by the electron beam. An image of a 1 μm hole covered with a continuous sheet of monolayer graphene is shown in **Figure 3.11a**. The area of the suspended region belongs to a single crystal of graphene. This is determined by collecting the electrons that are diffracted from the region within the red circle of **Figure 3.11a** with the selected area (SA) aperture of the microscope and changing the lens configuration to image the back focal plane of the objective lens. The selected area electron diffraction (SAED) pattern of the single crystal region of graphene is shown in **Figure 3.11b**.

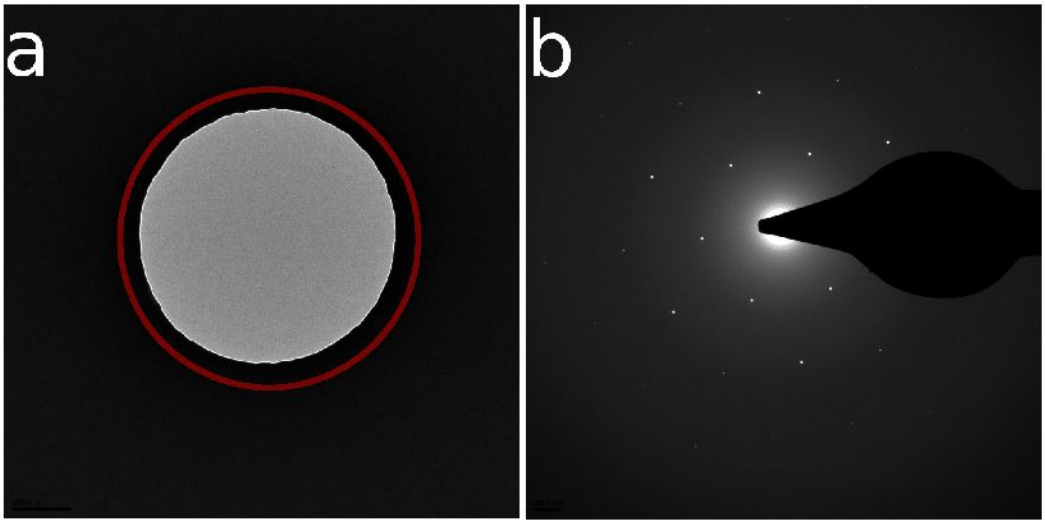

FIGURE 3.11. TEM analysis of a single crystal graphene membrane. (a) BF – TEM image of a 1 micron graphene membrane. The red circle illustrates the area exposed by the SA aperture of the microscope. (b) SAED pattern formed from imaging the back focal plane of the objective lens with the SA aperture inserted as shown in (a).

When larger areas are imaged and larger SA apertures are used for diffraction analysis, their often exists multiple diffraction patterns generated from a single area of graphene. This can occur if there are either multiple graphene layers that are rotated with respect to each other or if the single layer of graphene is polycrystalline with grain boundaries between distinct crystallographic grains [23,24]. Of course, a combination of the two situations is possible as well. The real space distribution of the different regions creating distinct diffraction patterns can be visualized through dark – field TEM (DF – TEM) imaging. Here, an objective aperture (OA) is placed in the back focal plane of the objective lens such that only the electrons from a single diffraction spot and any amorphous background are used to form an image. A complete TEM imaging and diffraction analysis of a 2 μm graphene membrane is shown in **Figure 3.12**. The standard bright – field TEM (BF – TEM) image (**Figure 3.12a** and **3.12b**) does not show any diffraction contrast. However, when an OA is placed at the three locations shown in **Figure 3.12c**, three different DF – TEM images are generated. Each one of these images reveals the

different graphene domains within the single sheet being visualized. The DF – TEM images are shown in **Figure 3.12d – 3.12f**.

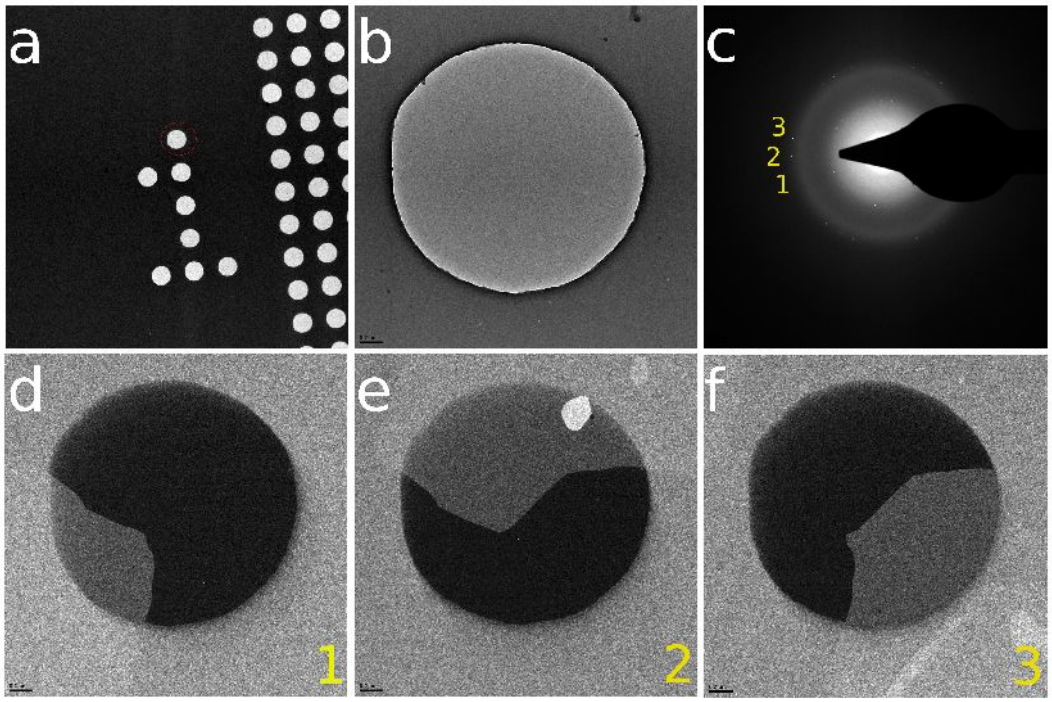

FIGURE 3.12. TEM analysis of a 2 micron polycrystalline graphene membrane. (a) Low magnification BF – TEM image of hole array in the TEM membrane. The red circle indicates the hole of interest. (b) High magnification BF – TEM image of the hole of interest. (c) SAED pattern acquired over the hole. (d) – (f) DF – TEM images acquired by collecting the diffracted electrons shown in (c).

3.4 GRAPHENE COATED AFM PROBES

Using the knowledge of the growth gained from direct observation of graphene on copper and from post processing, it is possible to fabricate polymer glass AFM probes with graphene present along the cantilever underside and over the probe apex. The first step in accomplishing AFM probe fabrication was to grow graphene on thin films of copper evaporated on SiO_2 on Si substrates. These substrates are ideal for further fabrication of graphene films with geometries that follow etched patterns in the Si wafer. SEM images of graphene grown on copper thin films

on patterned SiO_2 on Si wafers is shown in **Figure 3.13**. The patterns are generated by conventional silicon chip processing techniques involving a combination of photolithography and anisotropic wet chemical etching with KOH solutions.

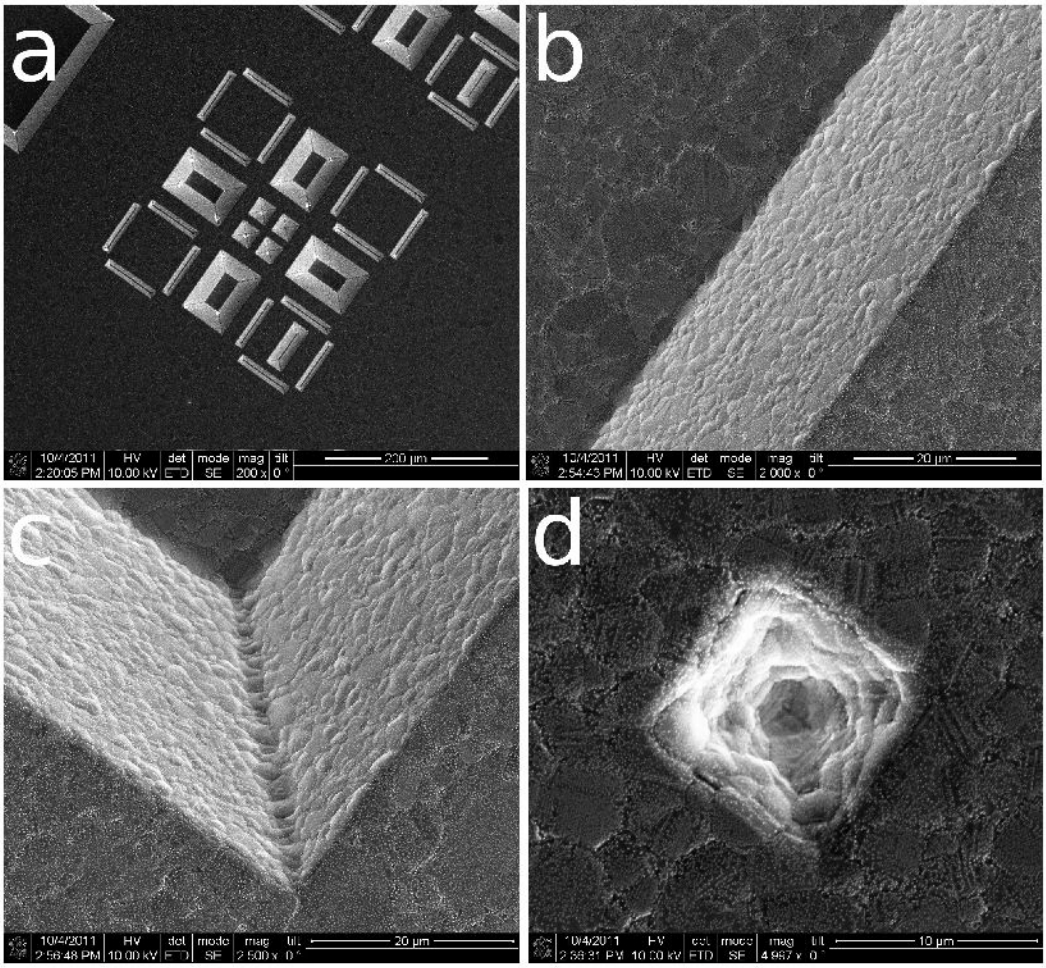

FIGURE 3.13. SEM image of graphene grown on pre – patterned SiO_2 – Si wafers coated with copper. (a) Low magnification images of substrate after growth, illustrating the variety of patterns that can be made in the substrate. (b) Edges of trenches showing continuous copper – graphene coverages. (c) Continuous coverage over vertices in the substrate patterns. (d) Inverted pyramid used as a mold for the fabrication of polymeric AFM probes.

Figure 3.13a shows a low magnification image of a variety of structures such as trenches, pits, and inverted pyramids that are coated with the copper – graphene layer. The copper uniformly coats the edges of the underlying structures present in the wafer (**Figures 3.13b** and **3.13c**) and

produces a continuous graphene film. For purposes of growing graphene coated AFM tips, inverted pyramids etched into the wafer can also be fabricated. A coated inverted pyramid use in the tip fabrication is shown in **Figure 3.13d**.

Once the patterned SiO_2 on Si wafers have the copper – graphene layer present, a series of lithography steps are used to build an AFM cantilever around the coated inverted pyramids in the substrate. **Figure 3.14** provides a schematic illustration of the steps required to fabricate graphene coated polymer cantilevers. First, a thin layer of SU-8, a common epoxy-based negative photoresist, is applied to the substrate with a spin coater. This layer is used to define the cantilever with the integrated graphene coated tip. Using standard photolithography and rinse, a set of cantilever structures are defined on the surface. A second, spin coating of SU-8 is performed in order to define the AFM chip, which is primarily used for handling the probe. The surrounding graphene not directly beneath the AFM probe is remove with an Argon plasma dry etch. Lastly, the probes are released by dissolution of the copper with etchant.

The AFM probes produced by this method can produce hundreds of probes for a single processing set, limited only by the size of the silicon wafer used. Optical microscope images of a set of AFM probes and the tip of a cantilever are shown in **Figure 3.15**. In order to characterize the cantilevers, particularly the tip apex, the probes were imaged in an SEM as well (**Figure 3.16**). A single cantilever and an array are shown in **Figure 3.16a** and **3.16b**. The dark features are attributed to continuous graphene coverage over the cantilever and tip. The white coating beginning at the cantilever base and extending over the entire support chip is an evaporated gold coating used for conductive AFM measurements between the graphene tip and any conducting substrate. The probes have tip radii of approximately 2.0 – 2.5 μm, as determined from high magnification SEM images (**Figure 3.16c** and **3.16d**).

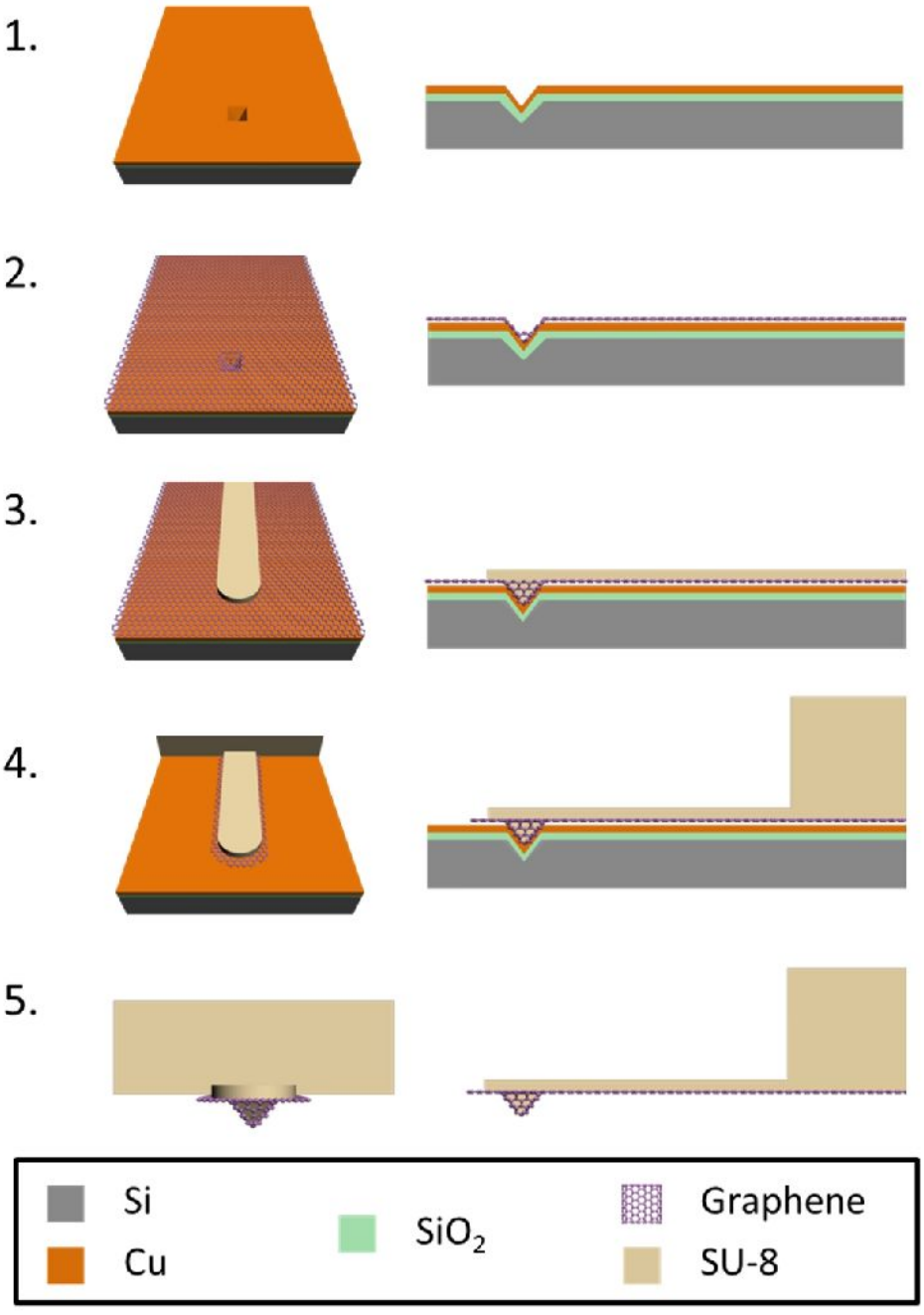

FIGURE 3.14. Schematic illustration of the graphene coated polymeric AFM probe fabrication process. Patterned substrates are coated with copper films by evaporation (1) and graphene is grown by standard CVD (2). Cantilever is defined through an initial spin coating of SU8 and photolithography (3). The residual is rinsed and the cantilever chip support is defined by a second step of spinning and photolithography (4). Graphene is removed from remaining substrate areas with a Argon plasma dry etch. Lastly, the probes are released from the substrate with chemical etchants.

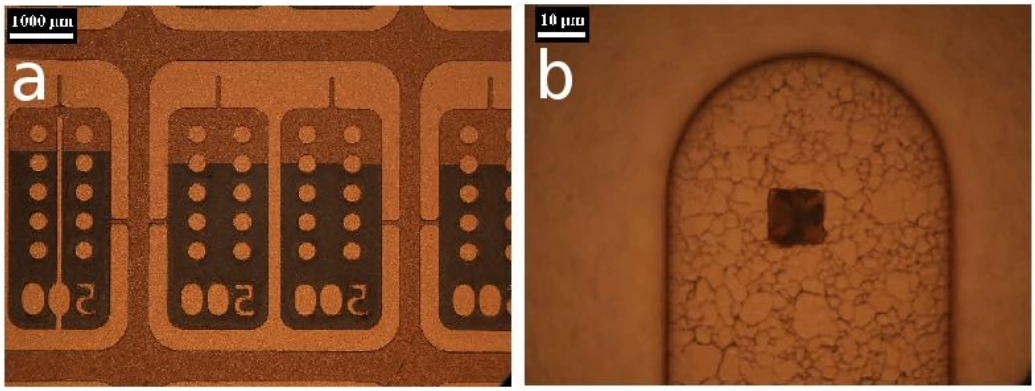

FIGURE 3.15. Optical images of fabricated polymeric AFM probes. (a) Low magnification image showing a set of cantilevers still attached to fabrication frame. (b) High magnification image showing an AFM tip. The cantilever underside clearly shows surface feature that directly replicate the copper morphology prior to dissolution.

The probes fabricated using the described process can be used to obtain AFM images in either a dynamic mode, such as AM – AFM, or a static mode of operation, such as CM – AFM. An example of an AM – AFM image taken over a calibration substrate containing 40 nm tall 1 µm wide pillars with a 2 µm spacing and a corresponding line profile is shown in **Figure 3.17a** and **3.17b**. A CM – AFM image on the same substrate and a corresponding line profile is shown in **Figure 3.17c** and **3.17d**. In the CM image, the features appear sharper and more well defined. This may be the result of a smaller interaction volume or the nature of the tip apex during imaging. It is evident from these AFM images that features well below 100 nm can easily be visualized with the fabricated probes.

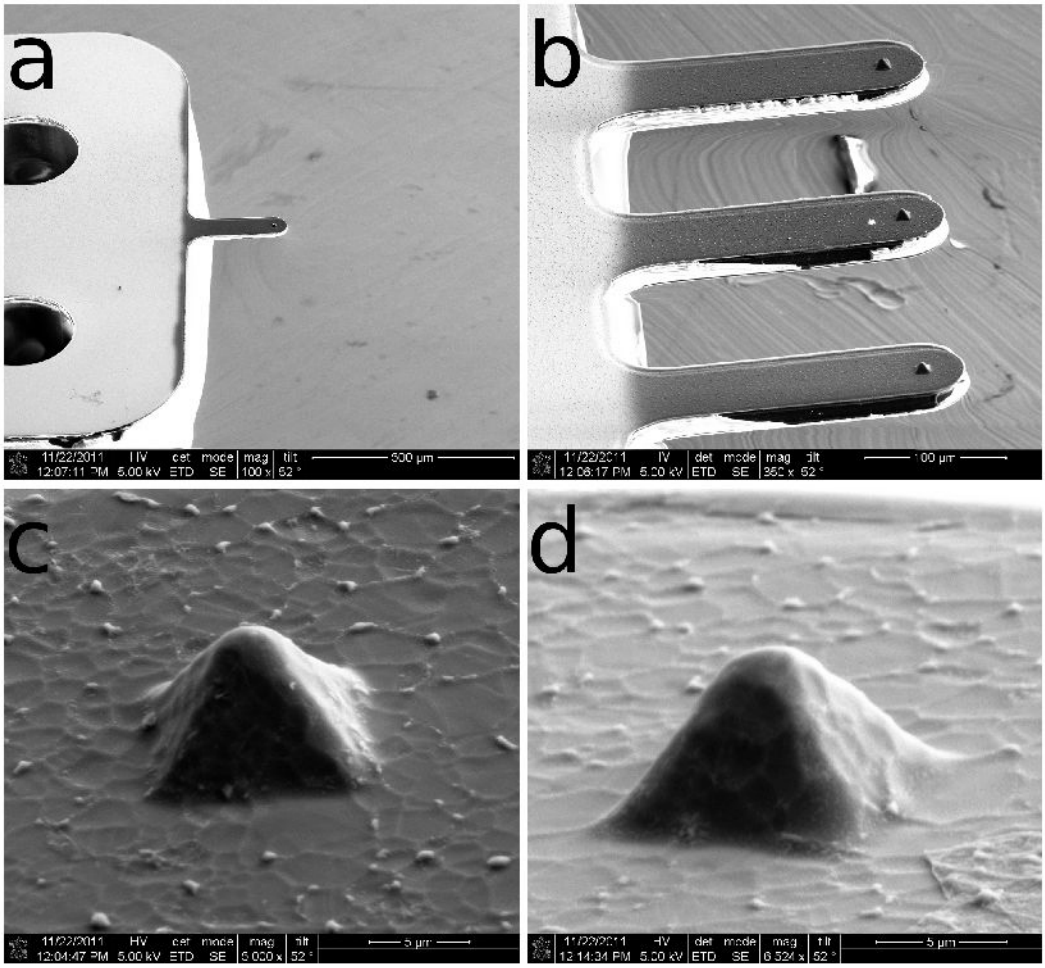

FIGURE 3.16. SEM images of graphene coated polymer AFM probes. (a) Low magnification image of a single AFM probe. The chip support was coated with gold (white snow like material) for conductive measurements between the AFM tip and surfaces of interest. (b) Cantilever array fabricated onto a single AFM chip support. (c) and (d) High magnification images of graphene coated AFM tips. The tip radii are uniform across different probes and in the range of 2.5 to 5.0 μm.

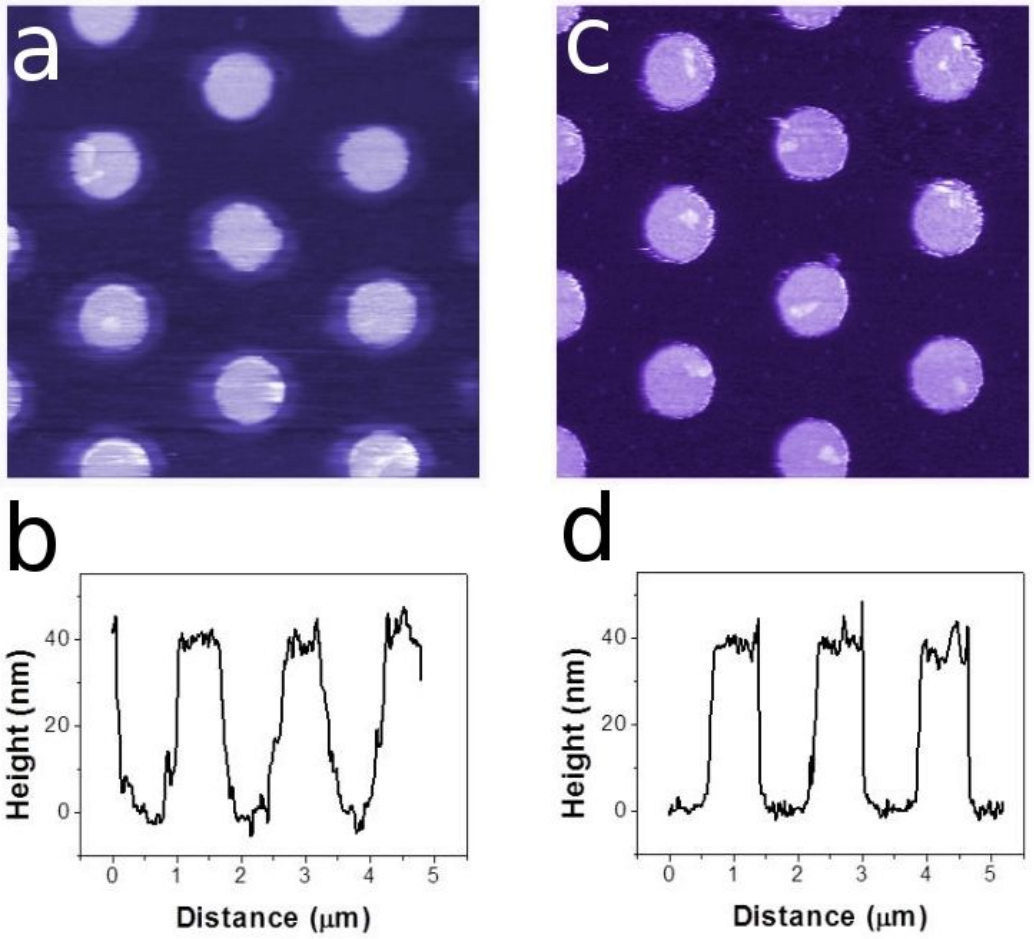

FIGURE 3.17. AFM images acquired with graphene coated probes. (a) AM – AFM image acquired on a test substrate with 1 μm wide pillars that are 40 nm tall, with a pitch of 2 μm. (b) Line profile taken over three pillars in (a). (c) CM – AFM image of the same substrate. The resolution appears better, which may be the result of a smaller interaction volume in this mode of imaging or the nature of tip during imaging. (d) Line profile taken over three pillars shown in (c).

3.5. SUMMARY

Results on the growth and processing of graphene grown on copper was presented. The fundamental knowledge gained by the body of work in this chapter forms the basis for the understanding required for the STM work that is presented in the preceding chapters. Graphene is shown to grow over the entirety of copper substrates, even crossing over a variety of grain boundaries present in the copper. Partial growths on the copper substrates reveal distinct island

growth morphologies on different copper grains. Temperature dependent studies of the growth reveal a significant reduction in reaction rates at lower temperatures. Using a spin coated polymer release film, it is possible to transfer graphene samples from the copper growth catalysts to arbitrary substrates for further analysis of the grown graphene. For example, transfer of graphene to TEM grids allows for the characterization of the crystallinity of the grown graphene through DF – TEM imaging. The suspended graphene membranes can also be imaged using an AFM and may allow for the probing of the mechanical properties such as the Young's modulus and failure strength of the grown material.

The knowledge gained from experiments on polycrystalline copper foil allowed for the growth of graphene on copper thin films deposited on patterned Si wafers. Through a combination of photolithography and chemical etching, polymeric cantilevers were fabricated. These cantilevers contain integrated AFM tips with covered graphene. The graphene coating on the polymer tip is expected to show a significant enhancement in the durability of the tip apex as a result of graphenes extraordinary strength. In addition, these probes may be used for fundamental studies of graphene interactions with a variety of materials. For instance, the graphene tips could be used to study frictional forces between graphene and hexagonal boron nitride, silicon dioxide, or any substrate of interest. Since the graphene is continuous from the AFM tip apex to the base of the cantilever, local electronic properties of a variety of conducting samples could also be measured.

3.6. REFERENCES

[1] Novoselov, K. S.; Geim, A. K.; Morozov, S. V.; Jiang, D.; Zhang, Y.; Dubonos, S. V.; Grigorieva, I. V.; Firsov, A. A. *Science* **2004**, 306, 666.

[2] Zhang, Y.; Tan, Y-W.; Stormer, H. L.; Kim, P. *Nature* **2005**, 438, 201.

[3] Lee, C.; Wei, X.; Kysar, J. W.; Hone, J. *Science* **2008**, 321, 385.

[4] Wei, X.; Fragneaud, B.; Marianetti, C. A.; Kysar, J. W. *Phys. Rev. B.* **2009,** 80, 205407.

[5] Cadelano, E.; Palla, P. L.; Giordano, S.; Colombo, L. *Phys. Rev. Lett.* **2009**, 102, 235502.

[6] Bolotin, K.I.; Sikes, K.J.; Jiang, Z.; Klima, M.; Fudenberg, G.; Hone, J.; Kim, P.; Stormer, H.L.; *Solid State Comm.* **2008**, 146, 351.

[7] Dean, C.R.; Young, A.F.; Meric, I.; Lee, Cl; Wang, L.; Sorgenfrei, S.; Watanabe, K.; Taniguchi, T.; Kim, P.; Shepard, K.L.; Hone, J. *Nat. Nanotech.* **2010**, 5, 722.

[8] Xue, J.; Sanchez-Yamagishi, J.; Bulmash, D.; Jacquod, P.; Deshpande, A.; Watanabe, K.; Taniguchi, T.; Jarillo-Herrero, P.; LeRoy, B. J. *Nat. Mater.* **2011**, 10, 282.

[9] Koenig, S. P.; Boddeti, N. G.; Dunn, M. L.; Bunch, J. S.; *Nat. Nanotech.* **2011**, 6, 543.

[10] Bunch, J. S.; Verbridge, S. S.; Alden, J. S.; van der Zande, A. M.; Parpia, J. M.; Graighead, H. G.; McEuen, P. L.; *Nano Letters* **2008,** 8, 2458.

[11] Bai, J.; Zhong, X.; Jiang, S.; Huang, Y.; Duan, X. *Nat. Nanotech.* **2010**, 5, 190.

[12] Li, X.; Wang, X.; Zhang, L.; Lee, S.; Dai, H.; *Science* **2008**, 319, 1229.

[13] Liao, L.; Bai, J.; Cheng, R.; Zhou, H.; Liu, L.; Liu, Y.; Huang, Y.; Duan, X. *Nano Letters* **2012,** 12, 2653.

[14] Cheng, R.; Bai, J.; Liao, L.; Zhou, H.; Chen, Y.; Liu, L.; Lin, Y-C.; Jiang, S.; Huang, Y.; Duan, X. *Proc. Nat. Acad. Sci.* **2012,** Early Edition.
DOI:10.1073/pnas.1205696109/-/DCSupplemental.

[15] Bunch, J. S.; van der Zande, A. M.; Verbridge, S. S.; Frank, I. W.; Tanenbaum, D. M.; Parpia, J. M.; Craighead, H. G.; McEuen, P. L. *Science* **2007**, 315, 490.
[16] Barton, R. A.; Ilic, B.; van der Zande, A. M.; Whitney, W. S.; McEuen, P. L.; Parpia, J. M.; Craighead, H. G. *Nano Letters* **2011**, 11, 1232.

[17] Chen, C.; Rosenblatt, S.; Bolotin, K. I.; Kalb, W.; Kim, P.; Kysmissis, I.; Stormer, H. L.; Heinz, T. F.; Hone, J. *Nat. Nanotech.* **2009**, 4, 861.

[18] Eichler, A.; Moser, J.; Chaste, J.; Zdrojek, M.; Wilson-Rae, I.; Bachtold, A. *Nat. Nanotech.* **2011**, 6, 339.

[19] Coraux, J.; N'Diaye, A.T.; Busse, C.; Michely, T. *Nano Lett.* **2008**, 8, 565.

[20] Ueta, H.; Saida, M.; Nakai, C.; Yamada, Y.; Sasaki, M.; Yamamoto, S. *Surf. Sci.* **2004**, 560, 183.

[21] Sutter, P. W.; Flege, J-I.; Sutter, E. A. *Nat. Mater.* **2008**, 7, 406.

[22] Nie, S.; Bartlet, N.C.; Wofford, J. M.; Dubon, O. D.; McCarty, K. F.; Thürmer, K. *Phys. Rev. B.* **2012**, 85, 205406.

[23] Nie, S.; Wofford, J. M.; Bartlet, N. C.; Dubon, O. D.; McCarty, K. F. *Phys. Rev. B.* **2011**, 84, 155425.

[24] Walter, A. L.; Nie, S.; Bostwick, A.; Kim, K. S.; Moreschini, L.; Chang, Y. J.; Innocenti, D.; Horn, K.; McCarty, K. F.; Rotenberg, E. *Phys. Rev. B.* **2011**, 84, 195443.

[25] Li, X.; Cai, W.; An, J.; Kim, S.; Nah, J.; Yang, D.; Piner, R.; Velamakanni, A.; Jung, I.; Tutuc, E.; Banerjee, S. K.; Colombo, L.; Ruoff, R. S. *Science* **2009**, 324, 1312.

[26] Li, X.; Cai, W.; Colombo, L.; Ruoff, R. S. *Nano Lett.* **2009**, 9, 4268.

[27] Huang, P. Y.; Ruiz-Vargas, C. S.; van der Zande, A. M.; Whitney, W. S.; Levendorf, M.P.; Kevek, J. W.; Garg, S.; Alden, J. S.; Hustedt, C. J.; Zhu, Y.; Park, J.; McEuen P. L.; Muller, D. A. *Nature* **2011**, 469, 389.

[28] Kim, K.; Lee, Z.; Regan, W.; Kisielowski, C.; Crommie, M. F.; Zettl, A. *ACS Nano* **2011**, 5, 2142.

[29] Yazyev, O. V.; Louie, S. G. *Nat. Mater.* **2010**, 9, 806.

[30] Yazyev, O. V.; Louie, S. G. *Phys. Rev. B* **2010**, 81, 195420.

[31] Grantab, R.; Shenoy, V. B.; Ruoff, R. S. *Science* **2010**, 330, 946.

[32] Wei, Y.; Wu, J.; Yin, H.; Shi, X.; Yang, R.; Dresselhaus, M. *Nat. Mater.* **2012**, Advanced On-Line Publication. DOI: 10.1038/nmat3370.

[33] Tsen, A. W.; Brown, L.; Levendorf, M. P.; Ghahari, F.; Huang, P. Y.; Havener, R. W.; Ruiz-Vargas, C. S.; Muller, D. A.; Kim, P.; Park, J. *Science* **2012**, 336, 1143.

[34] Li, X.; Magnuson, C. W.; Venugopal, A.; Tromp, R. M.; Hannon, J. B.; Vogel, E. M.; Colombo, L.; Ruoff, R. S.; *J. Am. Chem. Soc.* **2011**, 9, 2816.

CHAPTER 4

CONTINUITY OF GRAPHENE ON POLYCRYSTALLINE COPPER

4.1 INTRODUCTION

Knowledge of material growth mechanisms on solid supports allows scientists to grow materials with highly desired properties. In heteroepitaxy, lattice matching between deposited materials and single crystal substrates dramatically affects the properties of grown materials. For instance, small atomic lattice mismatches between substrates and growth materials creates significant strain in single crystal films [1] which can result in highly desired electronic properties or harmful defects [2]. In addition, when growing ionic films on metallic single crystals, the initial facet identity and mobility of the underlying substrate greatly influence resulting surface structures. In these systems, a strong interfacial binding between surface charges on vicinal metal surfaces and ionic overlayers [3,4] drives massive surface restructuring and selective growth on specific metal facets [5,6]. These exemplary studies illustrate the significant role of substrate – overlayer interactions in the field of film growth.

Recently, graphene growth [7 – 9] has been accomplished on the surface of several metal catalysts [10 – 15]. Of particular interest is the work by Li and colleagues [16], in which large scale graphene films were grown on copper foils and shown to be applicable for the production of practical transparent electrodes [17]. In the original work the authors suggested that the process occurs via a surface catalyzed reaction, which was corroborated by a mechanistic study using isotope labeled carbon [18]. For future electronic device applications and rational materials design, a fundamental understanding of the atomic structure of the as-grown graphene overlayer on copper substrates is of great importance [19,20]. Understanding the interplay between the copper surface and the growing honeycomb lattice of graphene will provide valuable information for the production of high quality graphene.

In this chapter, scanning tunneling microscope (STM) topographs of as-grown graphene produced by the thermal decomposition of methane on high purity polycrystalline copper disks is

discussed. The STM allows for the observation of the morphology of samples over several hundred square nanometers and obtain atomic resolution of graphene's carbon lattice at specific surface features of interest in a single experiment. The pristine graphene lattice is shown to exist over the copper substrate despite underlying features that are generally thought to create defects in a growing overlayer. Defect-free graphene is observed over edges and vertices of the copper substrate where line and point defects are expected under conventional wisdom. Furthermore, the perfect lattice is observed over crystalline facets of a different symmetry than graphene and over highly stepped surfaces, both of which should inhibit efficient sheet extension.

4.2 RESULTS AND DISCUSSION

Samples were first characterized by Raman spectroscopy and powder X-ray diffraction (XRD). **Figure 4.1a** shows a typical Raman spectrum of the as-grown graphene on a copper substrate. The 2D band at ~2700 cm^{-1} is symmetric with a full width at half maximum (FWHM) of 32cm^{-1} and is more than twice as intense as the G band at ~1600 cm^{-1}. These results are consistent with the synthesis of high quality monolayer graphene [21,22]. Polycrystallinity of the copper disc after graphene growth was established through XRD. A typical XRD pattern is shown in **Figure 4.1b**. Three low index facets of copper, (100), (110), and (111), are clearly oriented in the vertical direction, i.e. accessible to the imaging plane of the microscope. The only high index facet clearly observed in the diffraction pattern is the (311) plane.

While the substrate polycrystallinity is expected, it is remarkable that monolayer graphene can grow over a substrate with multiple facets of different identities and whose surface atomic configurations vary dramatically. In addition, it is interesting that the graphene layer has been shown, through SEM and optical studies, to grow continuously across the surface of different crystal grains present in the copper substrate [16]. This was also independently

confirmed by our group through the analysis of partial growth samples, as discussed in Chapter 3. The (111) and (100) facets of the face centered cubic (FCC) copper metal have a "flat" hexagonal and cubic atomic arrangement at the surface of the bare metal with each atom having 6 and 4 in plane nearest neighbors, respectively. Conversely, the (110) and (311) facets have complex corrugated atomic arrangements at the surface with significant anisotropy. These fundamental geometric differences of the facets are expected to have distinct surface energy potentials, affecting the carbon atom extension differently.

Large area scans of graphene covered copper substrates taken at different locations show varied surface topography, but with common fundamental features. A three dimensional topograph of a large area is shown in **Figure 4.1c**. Some areas have large atomically flat regions that span hundreds of nanometers. Other areas have a highly corrugated surface, which is the result of small atomically flat planes oriented in different directions and with surface areas of a few tens of nanometers.

The continuity of graphene was established through atomic resolution imaging at various features of interest. A typical atomic resolution image is shown in **Figure 4.1d** and clearly shows the typical honeycomb structure at the surface. An STM topograph of a corrugated area of the sample is shown in **Figure 4.2a**. The surface structure is characterized by different sets of parallel flat planes intersecting to form edges or vertices. An edge is defined as the intersection of two distinct planes and a vertex as the intersection of three or more planes. Atomic resolution images taken in certain flat areas show a perfect graphene lattice with a superimposed aperiodic

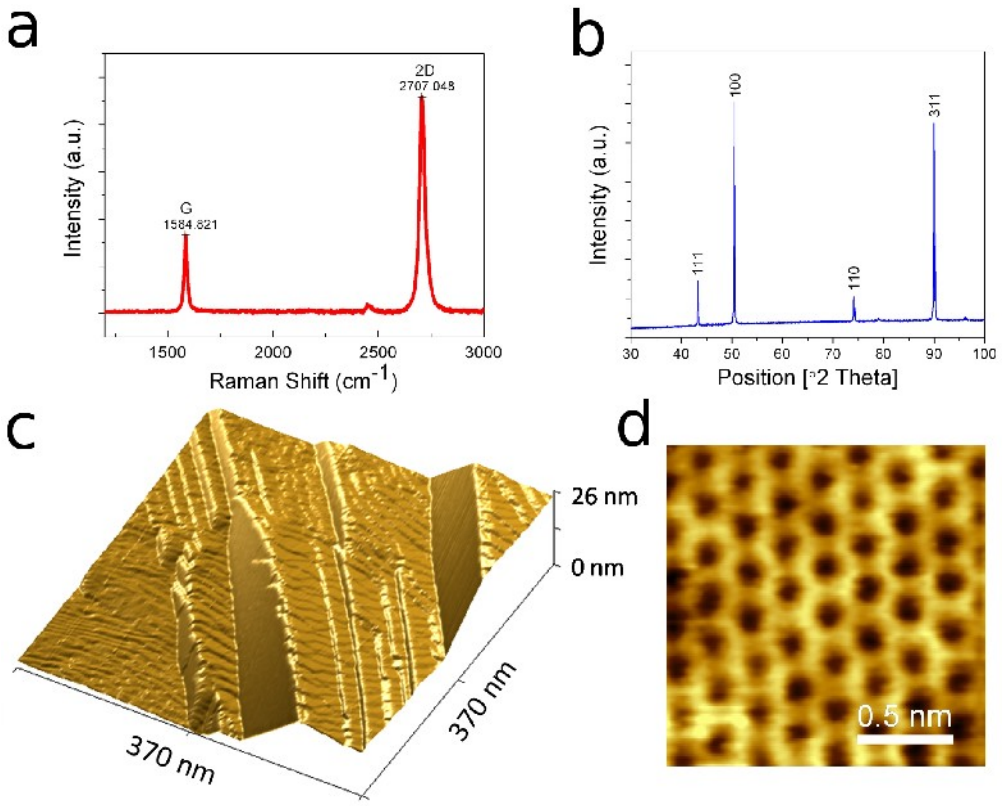

Figure 4.1. Characterization of as-grown graphene on polycrystalline copper. (a) Typical Raman spectrum of graphene on a polycrystalline copper substrate (after subtraction of copper luminescent background). (b) Powder X – ray diffraction pattern of a copper disk after growth. (c) Typical large area STM topograph of as – grown graphene on a copper substrate: $I_{tunneling} = I_t = 0.9$ nA, $V_{sample} = V_s = -75$ mV. (c) Atomic resolution STM image of the pristine carbon honeycomb lattice: $I_t = 5.0$ nA, $V_s = -75$ mV.

modulation. The height variations proceed for a few nanometers with localized depressions of a half nanometer in width and up to 30 pm in depth. These modulations are attributed to defects within the copper substrate since freely suspended graphene shows larger intrinsic modulation amplitudes of 1 nm and longer coherence lengths of approximately 10 nm [23]. An example of such an area is rendered in a colored three dimensional topograph in **Figure 4.2b**. The copper may create these variations in the STM topograph where atomic vacancies exist near or at the interface between the metal and graphene overlayer [3]. This is expected since copper mobility is

extremely high at the growth temperature of 1000 °C and vacancies can become pinned between the graphene sheet and the copper during cooling.

Within the flat regions, single and double atomic copper steps draped with a continuous layer of pristine graphene are observed. **Figure 4.2c** shows an atomic resolution STM topograph of a graphene sheet draped over a monatomic copper step. While the continuity of graphene over monatomic steps of single crystal metal surfaces such as Ru (0001) and Ir (111) is known [10,11], the mechanism of growth at these features remains an active area of theoretical and experimental research [24,25]. The growth mechanism associated with the extension of a carbon front (the foremost atoms of a sheet) "up" or "down" a monatomic metal step is thought to be fundamentally different. A schematic illustration of this process is shown in **Figure 4.2d**. The purple spheres represent the copper surface and the red highlighted spheres represent the carbon front of the graphene island depicted by the interconnected black spheres.

Recent findings suggest that the carbon front terminates at metal step edges through bonding of the dangling carbon sigma bonds to metal step atoms, inhibiting upward growth [10]. However, a different study suggests that the carbon front may displace metal atoms beneath the sheet and onto nearby terraces in order to accomplish upward growth through an etching of the catalytic surface [25]. In the downward direction, growth seems uninhibited and may occur through a carbon dimer extension to a lower terrace [24]. Each of these formulations treats the graphene sheet as extending over or affecting a stagnant catalytic surface. In our experiments graphene continuity over step edges is always observed with no signs of termination at copper steps and may proceed via a more dynamic growth mechanism.

Remarkably, it is also possible to observe pristine graphene conforming over the edges and vertices joining different copper facets. These two copper features can be further defined as

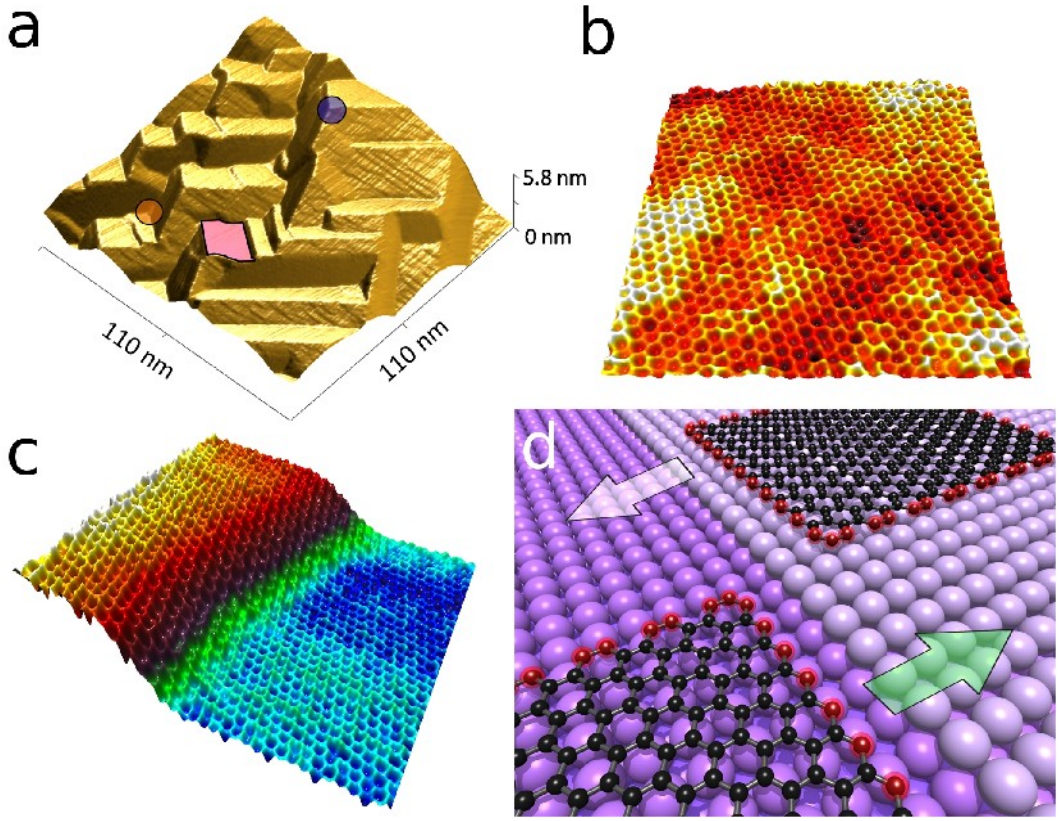

Figure 4.2. (a) STM topograph of a highly corrugated region of the sample. The magenta rectangle highlights an atomically flat plane, the blue circle highlights where three positive edges meet to form a positive vertex, and the orange circle highlights where three negative edges meet to form a negative vertex. (b) Atomic resolution STM topograph of a graphene sheet above an amorphous copper plane. (c) Atomic resolution STM topograph illustrating continuous growth over a copper monatomic step. (d) Schematic illustration of graphene growth "down" (white arrow) and "up" (green arrow) a monatomic Cu (100) step. Carbon atoms are represented by black spheres, foremost carbon atoms of the graphene sheet expected to interact with the monatomic step are highlighted with red spheres, light purple spheres represent copper atoms of the upper terrace, and darker purple spheres represent copper atoms of the lower terrace. Imaging parameters are as follows: (a) $\boldsymbol{I_t}$ = 0.5 nA, $\boldsymbol{V_s}$ = -500 mV, (b) $\boldsymbol{I_t}$ = 0.9 nA, $\boldsymbol{V_s}$ = -65 mV, and (c) $\boldsymbol{I_t}$ = 30 nA, $\boldsymbol{V_s}$ = -75 mV.

being either negative or positive based on their interaction with graphene. In the case of negative edges and vertices, the graphene bends toward the STM tip producing trough and valley structures in the observed topography. This creates a tension in the portion of the carbon p_z orbitals interacting with the copper substrate and a compression in the portion of the carbon p_z

orbitals interacting with the tip. In the case of positive edges and vertices, the sheet bends away from the STM tip producing ridge and hill structures in the observed topography and an opposite strain affect. **Figures 4.3a – 4.3d** exemplify the continuity of the graphene atomic lattice over these four fundamentally different copper surface features.

Under a stagnant growth model, the graphene front is expected to extend differently over positive and negative copper features. In the case of positive edges and vertices, the dangling bonds of the extending sheets are uninhibited by the copper atoms and are expected to grow continuously over these copper features in a manner that is comparable to extension down a monatomic step. In the case of negative edges and vertices, the copper atoms should terminate the sheet growth by bonding to the dangling bonds of the carbon lattice. This is analogous to what has been suggested for graphene growth termination on Ru (0001) at single monatomic steps [10], since a change in facet orientation is essentially a stack of atomic steps. As an example, a schematic illustration is provided in **Figure 4.3e**, where Cu (100) facets are oriented along the horizon and stacked vertically to make Cu (111) facets that should terminate graphene growth. However, a number of atomic resolution images of graphene over negative edges and vertices of the copper substrate have been acquired without sign of termination or creation of defects. Furthermore, the observation of all four surface features within a single area necessitates an upward and then downward extension across multiple facets, precluding only downward extension (i.e. repeated positive features).

The picture including displacement of monatomic step edges by the extending carbon front can adequately explain micron size graphene monolayers on single crystal metallic surfaces, which are known to have sub-micron step densities. However, in the case of the polycrystalline surface, the extending carbon front would need to displace a tremendous number of copper atoms beneath the growing sheet or to exposed copper atom aggregations to obtain the

observed features beneath graphene. An alternative explanation is that mobile copper atoms or clusters act as carbon carriers, allowing for sheet extension over the metal surface.

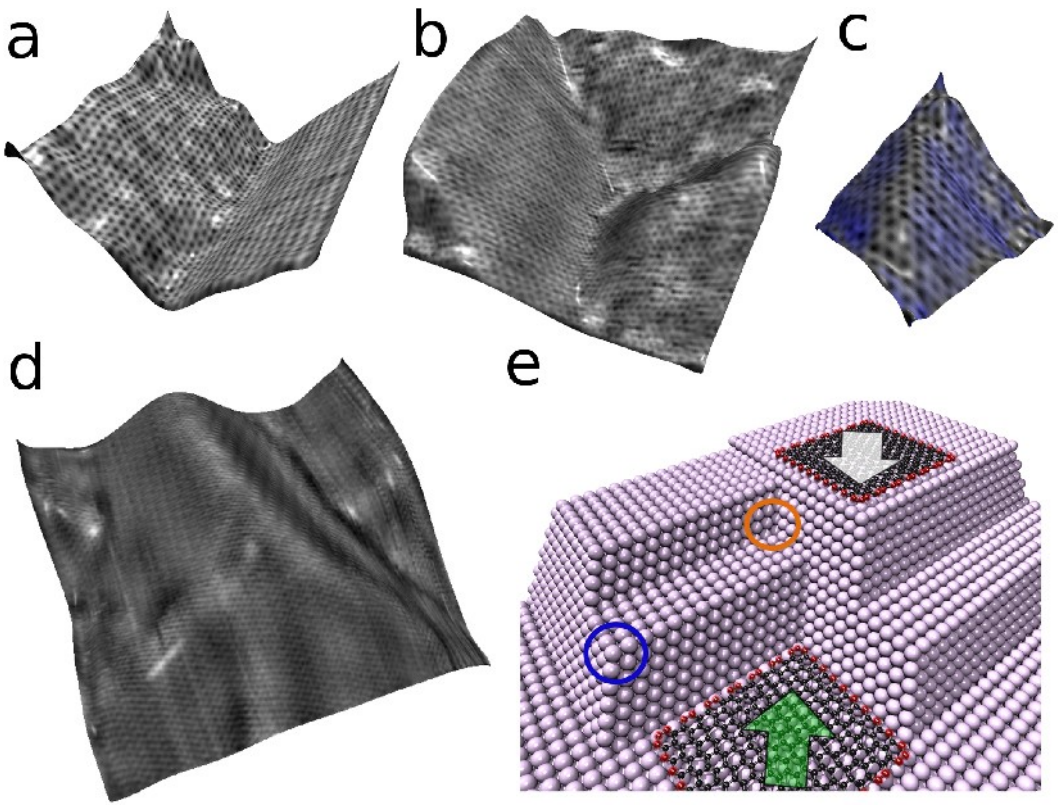

FIGURE 4.3. STM images illustrating defect – free growth of graphene over (a) a negative edge, (b) a negative vertex, (c) a positive edge, and (d) a positive vertex. (e) Schematic illustration of graphene growth "down" (white arrow) positive edges and vertices and "up" negative edges and vertices. Carbon atoms are represented by black spheres, foremost carbon atoms of the growing sheet expected to interact with edges and vertices are highlighted with red spheres, the blue circle illustrates where three positive edges unite at a positive vertex, and the orange circle illustrates where three negative edges unite at a negative vertex. Imaging parameters are as follows: (a) I_t = 5.0 nA, V_s = -75 mV, (b) I_t = 5.0 nA, V_s = -75 mV, (c) I_t = 0.9 nA, V_s = -75 mV, and (d) I_t = 1.0 nA, V_s = -500 mV.

A natural question that arises when analyzing the STM topographs is whether the underlying copper planes belong to crystallographic facets of different identities. Using higher order periodic modulations to the graphene sheet, we find that unique sets of modulations to graphene's atomic structure appear along sets of parallel planes of the sample. This can be seen

in **Figure 4.4a**. The modulations span the entirety of an atomically flat region and fade when the edge of one plane meets another plane oriented in a different direction. An atomic resolution image at the meeting of the edge can be seen in **Figure 4.4b**.

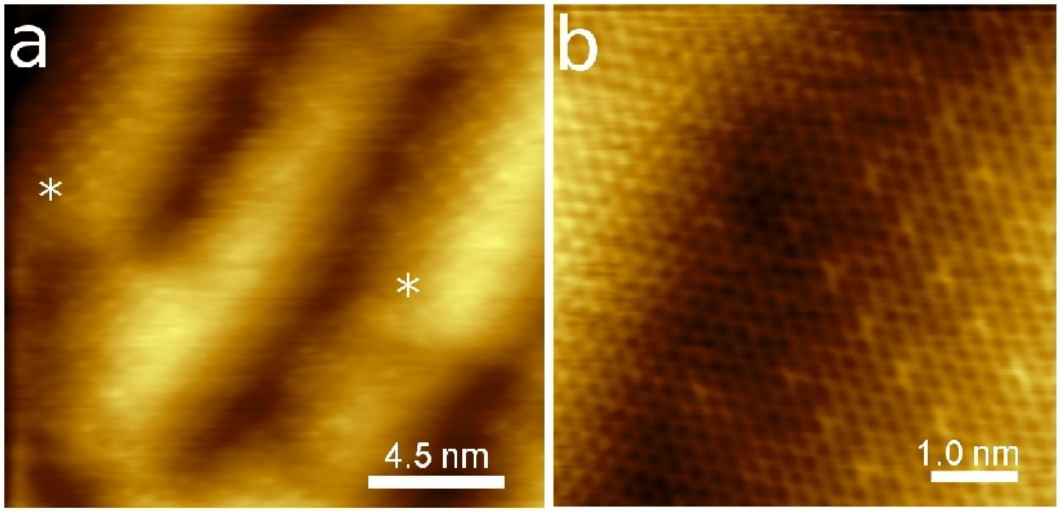

Figure 4.4. STM images over multiple parallel planes. (a) Large area image over multiple parallel planes. The white asterisks mark parallel planes where identical moiré patterns are observed. (b) Atomic resolution STM image of a periodic modulation to the graphene lattice. The pattern clearly disappears at the junction of two planes. Imaging parameters are as follows: (a) I_t = 0.99 nA, V_s = -75 mV, (b) I_t = 0.99 nA, V_s = -85 mV.

The two-dimensional spatial modulation frequency and apparent height of a unique pattern does not depend on the size or shape of the flat region. This indicates that the patterns are not a result of electron standing waves created from geometrical confinement as has been observed in graphene nanoribbons [26]. Additionally, it is possible to image these modulations with "moiré defects," where portions of the pattern are absent and replaced by slight depressions of approximately 10 pm with the graphene layer maintaining a pristine structure. An example of this is illustrated in **Figure 4.5**. The origin of the periodic modulations is, hence, attributed to the presence of different crystalline copper facets interacting with the graphene sheet to produce

unique moiré superstructures in an analogous manner to what has been observed for graphene on metal single crystals [11,13,14].

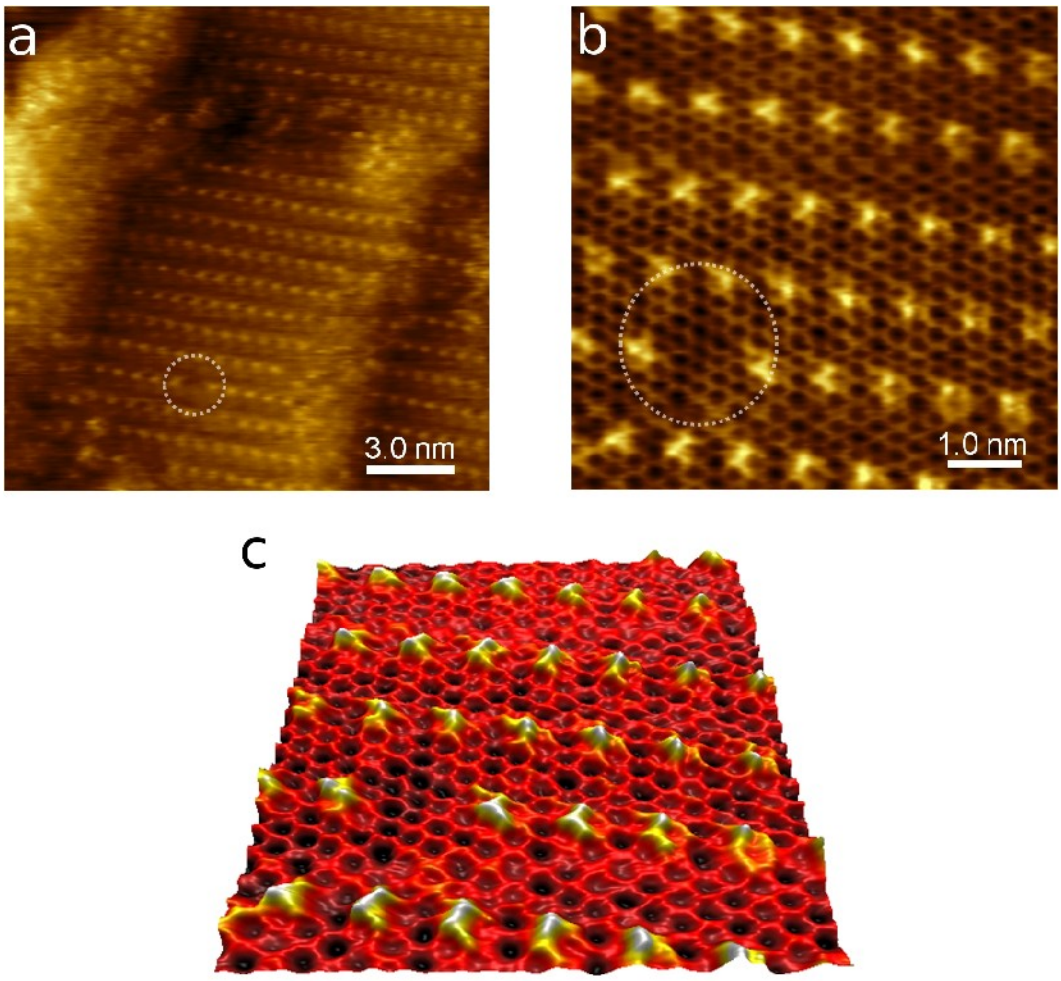

Figure 4.5. (a) STM image illustrating graphene growth over a large Cu (100) facet that produces a similar pattern as seen in Figures 4a and 4b. The missing bright spot (white circle) is attributed to a defect in the underlying copper substrate. (b) Atomic resolution image of the graphene lattice over the same area shown in (a). The graphene overlayer is observed to grow continuously over the same defect (white circle). (c) STM topography of Figure S1b, highlighting the affect of the underlying substrate on the constant current height field. Note that the graphene lattice shows a slight depression where the "moiré defect" exists.

In order to identify the atomic arrangement of the copper facets beneath the graphene, a moiré pattern analysis [27,28] was performed on each unique angle of a graphene overlayer on

the four facets appearing in the X-ray diffraction data. These images were then checked against the multitude of patterns appearing in STM topographs. Of particular interest is graphene growth observed over a Cu (100) facet. This is shown in **Figure 4.6a** where the graphene [11$\bar{2}$0] direction makes a 17 degree angle with the copper [011] direction. An atomic model for the STM image is presented in **Figure 4.6b**. The existence of the graphene layer over the Cu (100) facet is interesting because the symmetry of the underlying substrate is fundamentally different than that of graphene. The copper (100) square lattice belongs to the p4m plane crystallographic group whereas the hexagonal carbon lattice of graphene belongs to the p6m group. A model of the copper (100) surface is provided in **Figures 4.6c** and **4.6d**.

Another interesting aspect of the overgrowth is the continuity of the graphene lattice over the regularly stepped Cu (311) surface. This facet is comprised of alternating monatomic (111) and (100) nanofacets with a dilated hexagonal arrangement of the top most atoms. An STM topograph of a graphene sheet on a Cu (311) surface is shown in **Figure 4.7a**. The graphene [11$\bar{2}$0] direction makes a 6 degree angle with the [01$\bar{1}$] direction of the Cu (311) surface, which generates a moiré pattern with alternating bright and dark bands. The atomic model for the STM image this STM image is presented in **Figure 4.7b**. In addition, a model of the copper (311) surface is presented in **Figure 4.7c** and **4.7d** for clarity.

The structure of the (311) facet is of particular interest because the stepped surface is expected to produce a periodic strain that is strictly mechanical in nature as well as a charge – modulation beneath the graphene. The modulation is a result of charge smoothing and formation of electrostatic dipoles at step edges due to the Smoluchowski effect [29]. It has recently been

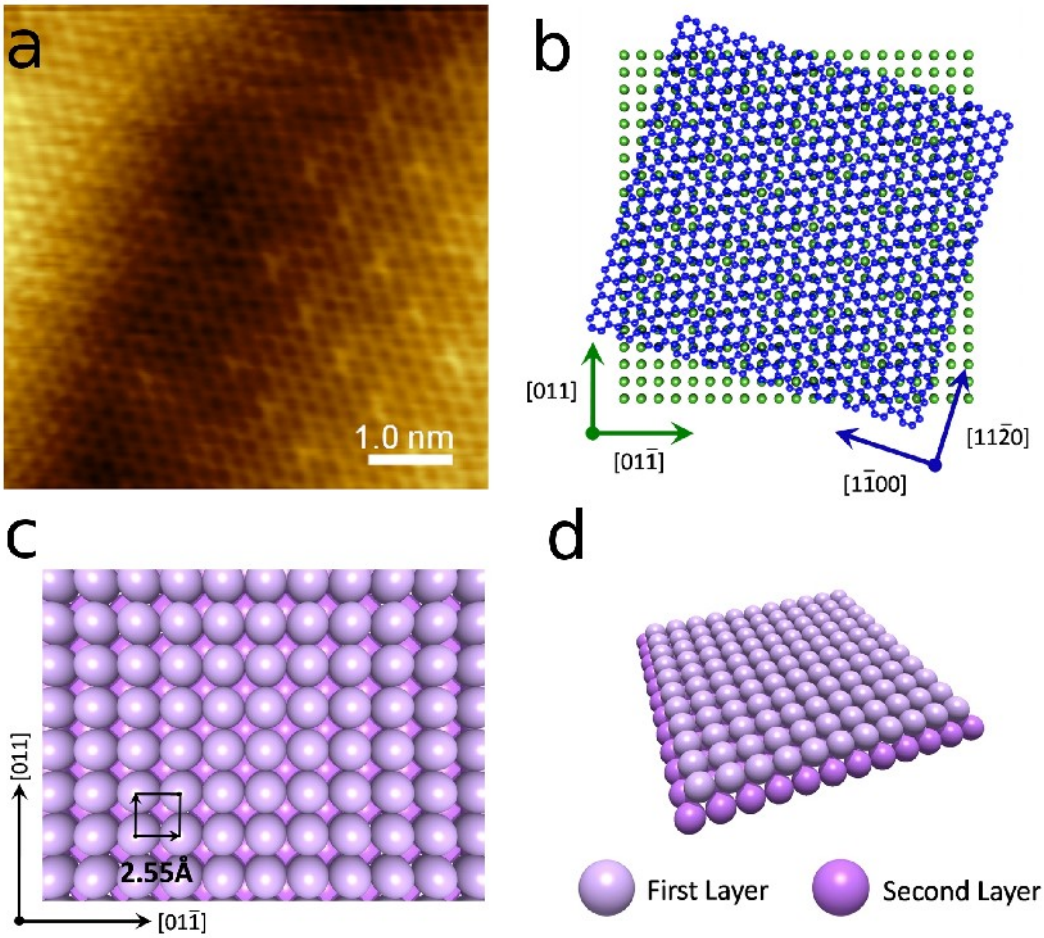

FIGURE 4.6. Graphene growth over a copper (100) plane. (a) Atomic resolution STM image of graphene growth over a Cu (100) facet. The graphene [11$\bar{2}$0] direction makes a 17 degree angle with the copper [011] direction. (b) Moiré pattern analysis of the STM image shown in (a). The green spheres and axis belong to copper and the blue lattice and axis belong to graphene. Hard sphere schematic illustrations of a (c) top view and a (d) perspective view of a Cu (100) facet, highlighting the square symmetry of the atomic arrangement and low surface corrugation. Imaging parameters are as follows: (a) I_t = 0.99 nA, V_s = -85 mV.

shown that surface adsorption and post modification of graphene layers atop low index metal single crystal surfaces are sensitive to the registry of the overlayer with the underlying metal atoms [30,31]. These affects have been exploited to induce measurable band gaps in graphene's electronic structure with the hope of making practical carbon based logic devices. By using graphene growth over stepped surfaces such as Cu (311) it may be possible to also exploit the

charge modulation of the underlying metal surface for applications requiring post modification.

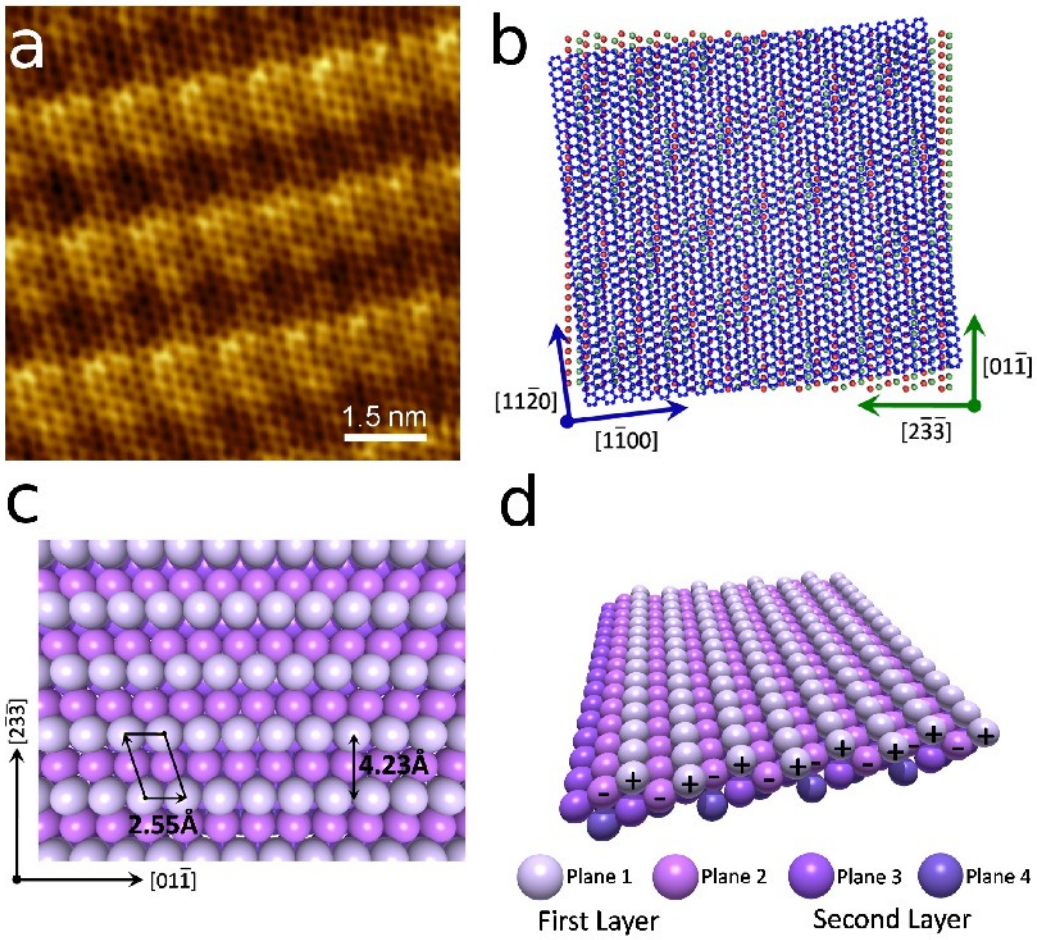

FIGURE 4.7. Graphene growth over a copper (311) plane. (a) Atomic resolution STM image of graphene growth over a Cu (311) facet. The graphene [11$\bar{2}$0] direction makes a 6 degree angle with the copper [01$\bar{1}$] direction. (b) Moiré pattern analysis of the STM image shown in (a). The red and green spheres belong to plane 1 and 2 of the Cu (311) facet. Hard sphere schematic illustration of a (c) top view and a (d) perspective view of the Cu (311) facet, highlighting the dilated hexagonal arrangement of the top most atoms and significant corrugation of the facet. In this facet two planes of atoms make up the first layer of exposed atoms at the surface. Each set of four distinct colors shown in (d) belong to a Cu (100) facet. As discussed in the main text, electric dipoles exist at this surface. The first plane of copper atoms (white spheres) carry a positive charge and the second plane of copper atoms (magenta spheres) carry a negative charge, which results in atomic scale stripes of periodic dipoles along the surface.

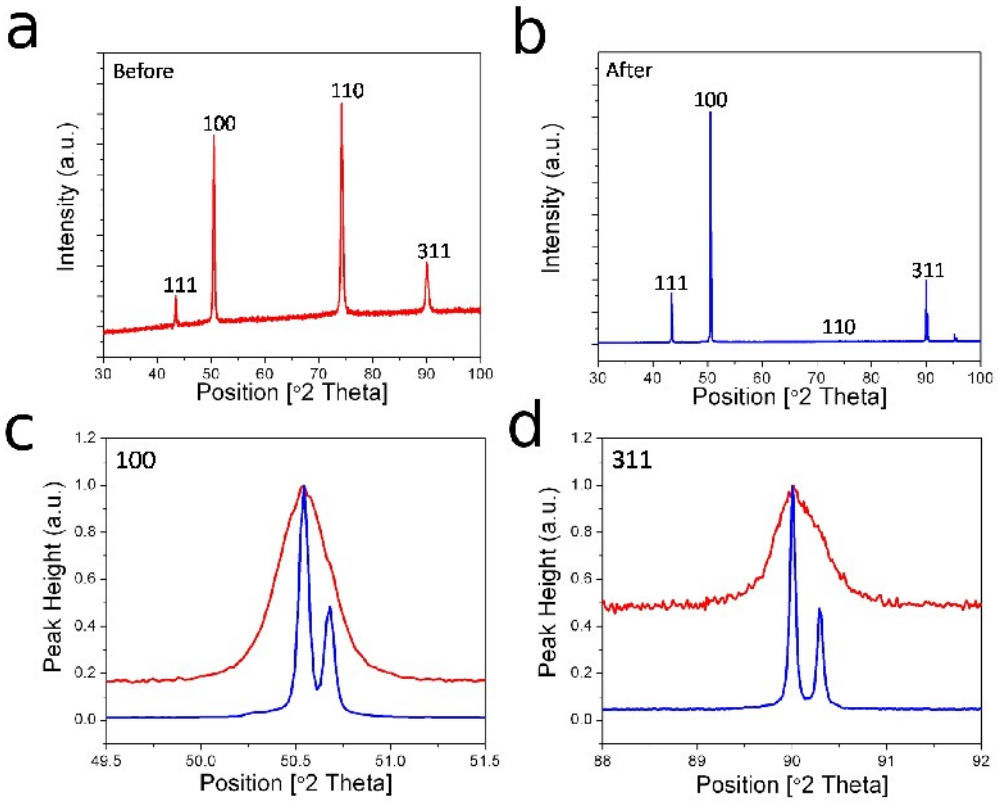

Figure 4.8. X – Ray diffraction pattern of a copper substrate. Diffraction (a) before and (b) after graphene growth. Each diffraction peak becomes sharper and splitting of the peaks into their respective Kα1 and Kα2 components is clearly observed. This is consistent with increased grain size and enhanced crystallinity of the copper substrate before and after graphene growth. The diffraction peaks of the (c) Cu (100) and the (d) Cu (311) facets before and after growth are provided to illustrate the clear change in substrate structure. This data provides strong evidence for copper atom mobility during graphene growth over the substrate surface.

Graphene continuity over the various surface features may be the result of mobile copper atoms or islands acting as carbon carriers which extend the graphene front over the copper surface with minimal inhibition in a type of "tiling" growth. This is analogous to the way a regularly arranged stone path may be laid over a complex terrain with hills and valleys. At the growth temperatures of 1000 °C, only 83 °C less than the metals melting point, the copper atoms have a high degree of mobility at the surface. This is corroborated by X-ray diffraction data presented in **Figure 4.8** where narrowing and splitting of the diffraction peaks of the graphene -

copper samples is observed as compared to the bare copper substrates, suggesting a substantial amount of mass transport within the copper catalyst during growth. While the trajectory of carbon carrying copper atoms or islands would primarily follow the copper substrate's symmetry during graphene growth, the high temperatures could provide sufficient kinetic energy for the surface diffusion required to generate trajectories that allow extension of the hexagonal carbon lattice over the square atomic lattice of the Cu (100) surface or over the highly corrugated and anisotropic Cu (311) facet.

4.3 SUMMARY

In summary, we have established the continuity of the perfect graphene atomic structure over a multitude of surface features on the copper substrate which are expected to inhibit efficient growth. Edges and vertices of the copper surface reveal perfect graphene growth where line or point defects are expected to occur through substrate induced sheet termination. The two exemplary cases of Cu (100) and Cu (311) reveal that overgrowth occurs on facets of different fundamental symmetries than graphene as well as on highly stepped vicinal surfaces. With the possibility to grow graphene on high index regularly stepped surfaces, it may be possible to make use of periodic charge modulation as well as atomic lattice registry for post modification studies. To date, this has been limited to growth on low index hexagonal single crystals for band gap studies. Our results reveal that graphene growth on copper is a unique system where the underlying substrate morphology and atomic arrangement does not affect the atomic arrangement of the grown material. Finally, the presented results suggest that the growth of continuous macroscopic pristine graphene on copper is not limited by the substrate.

4.4 MATERIALS AND METHODS

4.4.1 Sample Preparation

Graphene was grown by CVD, in a method similar to that described in Chapter 3. Briefly, the reactants were a mixture of high purity methane (CH_4) and hydrogen (H_2) gas and were allowed to react at 1000 °C in a tube furnace. Copper disks were loaded into a quartz tube and heated to 1000 °C over a period of ~40 minutes under a constant flow of H_2 gas. Samples were held at 1000 °C for 10 minutes before addition of methane. A flow rate of 100 sccm was used for CH_4 at a partial pressure of 6 Torr and a flow rate of 25 sccm was used for H_2 at a partial pressure of 1.5 Torr. After 20 minutes CH_4 flow is stopped. The sample is then cooled at a rate of ~20 °C/min under a 1.5 Torr atmosphere of H_2 gas. Copper disks were purchased from Alfa Aesar with the following characteristics; diameter = 9.0 mm, thickness = 0.8 mm, and percent purity = 99.9995%.

4.4.2 STM Imaging

Samples were imaged under ambient conditions using a home-built scanning probe microscope housed in a custom-built enclosure. All images were acquired in constant current mode with tunneling setpoints between 0.2 nA and 30 nA. Typical sample biases were acquired between -30mV and -300 mV, referenced to the tip voltage. A Nanonis Universal SPM Controller was used for all data acquisition.

4.4.3 X-ray Diffraction

The X-ray diffraction patterns were collected on an XPert Pro powder diffractometer with Cu Kα radiation (λ=1.5418 Å; PANalytical). Copper disks were rotated at a rate of 0.5 revs./sec.

in order to eliminate rotational asymmetries in the sample plane. Diffraction peaks were assigned according to JCPDS file #00-002-1225. Samples measured before and after graphene growth were acquired using identical measurement parameters.

4.4.4 Raman Spectroscopy

The raman spectroscopy characterization was acquired using a Renishaw Micro Raman microscope. An acquisition time of 600 seconds was used with a 514 nm laser. The laser power density irradiating the sample was less than $2mW/\mu m^2$.

4.5 REFERENCES

[1] Roberts, M. M.; Klein, L. J.; Savage, D. E.; Slinker, K. A.; Friesen, M.; Celler, G.; Eriksson, M. A.; Lagally, M. G. *Nat. Mater.* **2006**, 5, 388.

[2] Chen, Y.; Washburn, J. *Phys. Rev. Lett.* **1996**, 77, 4046.

[3] Repp, J.; Fölsch, S.; Meyer, G.; Rieder, K-H. *Phys. Rev. Lett.* **2001**, 86, 252.

[4] Olsson, F. E.; Persson, M. *Surf. Sci.* **2003**, 540, 172.

[5] Fölsch, S.; Helms, A.; Zöphel, S.; Repp, J.; Meyer, G.; Rieder, K-H. *Phys. Rev. Lett.* **2000**, 84, 123.

[6] Fölsch, S.; Riemann, A.; Repp, J.; Meyer, G.; Rieder, K-H. *Phys. Rev. B* **2002**, 66, 161409(R).

[7] Geim, A. K.; Novoselov, K. S. *Nat. Mater.* **2007**, 6, 183.

[8] Castro Neto, A. H.; Guinea, F.; Peres, N. M. R.; Novoselov, K. S.; Geim, A. K. *Rev. Mod. Phys.* **2009**, 81, 109.

[9] Zhu, Y.; Murali, S.; Cai, W.; Li, X.; Suk, J.; Potts, J. R.; Ruoff, R. S. *Advanced Materials* **2010**, 22, 3906.

[10] Sutter, P. W.; Flege, J-I.; Sutter, E. A. *Nat. Mater.* **2008**, 7, 406.

[11] Coraux, J.; N'Diaye, A.T.; Busse, C.; Michely, T. *Nano Lett.* **2008**, 8, 565.

[12] Reina, A.; Jia, X.; Ho, J.; Nezich, D.; Son, H.; Bulovic, V.; Dresselhaus, M. S.; Kong, J. *Nano Lett.* **2009**, 9, 30.

[13] Ueta, H.; Saida, M.; Nakai, C.; Yamada, Y.; Sasaki, M.; Yamamoto, S. *Surf. Sci.* **2004**, 560, 183.

[14] Gao, L.; Guest, J. R.; Guisinger, N. P. *Nano. Lett.* **2010**, 10, 3512.

[15] Zhao, L.; Rim. K. T.; Zhou, H.; He, R.; Heinz, T. F.; Pinczuk, A.; Flynn, G. W.; Pasupathy, A. N. **2010** (http://arxiv.org/ftp/arxiv/papers/1008/1008.3542.pdf)

[16] Li, X.; Cai, W.; An, J.; Kim, S.; Nah, J.; Yang, D.; Piner, R.; Velamakanni, A.; Jung, I.; Tutuc, E.; Banerjee, S. K.; Colombo, L.; Ruoff, R. S. *Science* **2009**, 324, 1312.

[17] Bae, S.; Kim, H.; Lee, Y.; Xu, X.; Park, J – S.; Zheng, Y.; Balakrishnan, J.; Lei, T.; Kim, H. R.; Song, Y. II; Kim, Y – J; Kim, K. S.; Özyilmaz, B.; Ahn, J – H; Hong, B. H.; Iijima, S. *Nat. Nanotechnol.* **2010**, 5, 574.

[18] Li, X.; Cai, W.; Colombo, L.; Ruoff, R. S. *Nano Lett.* **2009**, 9, 4268.

[19] Rutter, G. M.; Crain, J. N.; Guisinger, N. P.; Li, T.; First, P. N.; Stroscio, J. A. *Science* **2007**, 317, 219.

[20] Lee, C.; Wei, X.; Kysar, J. W.; Hone, J. *Science* **2008**, 321, 385.

[21] Ferrari, A. C.; Meyer, J. C.; Scardaci, V.; Casiraghi, C.; Lazzeri, M.; Mauri, F.; Piscanec, S.; Jiang, D.; Novoselov, K. S.; Roth, S.; Geim, A. K. *Phys. Rev. Lett.* **2006**, 97, 187401.

[22] Graf, D.; Molitor, F.; Ensslin, K.; Stampfer, C.; Jungen, A.; Hierold, C.; Wirtz, L. *Nano Lett.* **2007**, 7, 238.

[23] Meyer, J. C.; Geim, A. K.; Katsnelson, M. I.; Novoselov, K. S.; Booth, T. J.; Roth, S. *Nature* **2007**, 446, 60.

[24] Chen, H.; Zhu, W.; Zhang, Z. *Phys. Rev. Lett.* **2010**, 104, 186101.

[25] Starodub, E.; Maier, S.; Stass, I.; Bartlet, N. C.; Feibelman, P. J.; Salmeron, M; McCarty, K. F. *Phys. Rev. B* **2009**, 80, 235422.

[26] Wassmann, T.; Seitsonen, A. P.; Saitta, A. M.; Lazzeri, M; Mauri, F. *J. Am. Chem. Soc.* **2010**, 132, 3440.

[27] Loginova, E.; Nie, S.; Thürmer, K.; Bartlet, N. C.; McCarty, K. F. *Phys. Rev. B* **2009**, 80, 085430.

[28] Repp, J.; Meyer, G.; Rieder, K-H. *Phys. Rev. Lett.* **2004**, 92, 036803.

[29] Smoluchowski, R. *Phys. Rev.* **1941**, 60, 661.

[30] N'Diaye, A. T.; Bleikamp, S.; Feibelman, P. J.; Michely, T. *Phys. Rev. Lett.* **2006**, 97, 215501.

[31] Balog, R.; Jørgensen, B.; Nilsson, L.; Andersen, M.; Rienks, E.; Bianchi, M.; Fanetti, M.; Laegsgaard, E.; Baraldi, A.; Lizzit, S.; Sljivancanin, Z.; Besenbacher, F.; Hammer, B.; Pendersen, T. G.; Hofmann, P.; Hornekaer, L. *Nat. Mater.* **2010**, 9, 315.

CHAPTER 5

GRAPHENE GROWTH ON COPPER (100) SINGLE CRYSTALS

5.1 INTRODUCTION

As discussed in Chapter 3, graphene has remarkable electronic [1,2] and mechanical properties [3,4]. Initial electronic measurements [5,7] used pristine graphene sheets isolated by mechanical exfoliation from naturally occurring graphite on silicon-insulator substrates [8]. While devices derived by exfoliation have provided scientists with valuable insights into the electronic transport and mechanics of this remarkable material, a more scalable method for obtaining isolated graphene sheets is required for widespread use. To this end, graphene has been synthesized by physical desorption of Si from SiC single crystal surfaces [9,10], chemical treatments of graphite [11 – 13], and from small organic molecules involving different metal substrates [14 – 20].

Of particular interest is the growth of graphene on copper substrates [18 – 20], which provides many unique advantages, such as industrial scalability and efficient processing of grown films. In fact, large scale fabrication of graphene by chemical vapor deposition (CVD) on copper foils [18] has been used to assemble transparent electrodes and commercial prototype touch screen displays [21]. In order to realize further high quality electronic devices and rational materials from this method of synthesis, atomic scale characterization of grown graphene and a fundamental understanding of the mechanisms governing the growth process are of great importance. Recent STM [22] and LEEM/LEED [23] studies of graphene on polycrystalline copper substrates have revealed that graphene extension can occur on crystal grains that are oriented such that the square atomic lattice of the Cu(100) surface can act as a suitable solid support for catalysis of graphene growth, with LEEM/LEED studies suggesting that the (100) face being the primary exposed facet. While studies on polycrystalline substrates provide valuable information regarding growth, characterization and growth on single crystal substrates allows for a deeper understanding without the presence of surface features such as copper grain

boundaries, identical crystal grains oriented in different directions, and large areas of exposed facets of different identities whose surface arrangement of atoms vary dramatically.

In this chapter, STM topographs of as-grown graphene produced by CVD through the thermal decomposition of methane on high purity Cu(100) single crystal substrates at elevated temperatures are presented. Observation of the large scale morphology of samples was accomplished over hundreds of square nanometers with atomic resolution images acquired at specific features of interest. Raman spectroscopy reveals that it is possible to grow high quality graphene on the Cu(100) surface. Through detailed moiré analysis of the superstructures present in atomic resolution images of the graphene overlayer, the carbon lattice is shown to grow in different orientations with respect to the atomic lattice of the copper crystal. The lack of a clear epitaxial relationship between graphene's honeycomb lattice and the Cu(100) square lattice is shown to translate into the growth of polycrystalline graphene islands and continuous sheets through the use of the TEM analysis previously discussed in Chapter 3. The perfect continuous carbon lattice is observed to exist over copper step edges, corners, and screw dislocations present at the surface, which are generally thought to provide barriers to efficient sheet extension. These features have been shown to create defects in growing graphene sheets on different metal catalysts [14]. Distinct protrusions, known as “flower” structures, are observed over the sample surface and are attributed to breaks from the standard hexagonal bonding within the carbon atomic lattice. Grown graphene is also shown to be continuous over small copper adatom clusters and vacancy islands present at the surface of the single crystal. These vacancy islands show significant copper atom mobility at room temperature beneath suspended graphene sheets. Lastly, the implications of these observations in the context of the mechanism of graphene growth on copper substrates is discussed.

5.2 RESULTS AND DISCUSSION

Large scale STM images of Cu(100) single crystal surfaces overgrown with graphene (**Figure 5.1a**), at full surface coverage, show large atomically flat terraces that have surface areas of a few hundred square nanometers. The total height variation over 500 nm^2 is only 1.98 nm, which is more than an order of magnitude lower than what has been observed for similar areas of graphene grown on polycrystalline copper substrates [22]. Each atomically flat terrace has step edges that come together in right angle corners that are aligned along the {011} crystal directions with step heights of approximately 0.18nm, which is characteristic of the Cu(100) surface. In order to highlight the small height variation over the copper surface, a cross section of **Figure 5.1a** is provided in **Figure 5.1b**. In this line profile, three distinct levels of copper terraces are clearly observed with atomic flats that proceed for more than 100 nm. These large terraces present throughout the sample have smaller scattered rectangular islands and pits with single monatomic step heights that are overgrown with defect-free graphene.

In addition to acquiring STM topographs, the graphene overlayer was characterized through Raman spectroscopy. **Figure 5.1c** shows a typical Raman spectrum of as-grown graphene on a single crystal, after subtraction of the copper luminescent background. The peak located at ~2700 cm^{-1} (2D Band) is symmetric with a full width at half maximum (FWHM) of 33 cm^{-1} and is more than twice as intense as the peak located around 1600 cm^{-1} (G band). No measurable peak is observed around 1350 cm^{-1} (D band). These results are consistent with the synthesis of high quality monolayer graphene [24,25].

Once large area images were obtained over the surface, we characterized the atomic structure of the graphene overlayer (**Figure 5.1d**) and its registry with the copper lattice. This is accomplished by analyzing higher order periodic modulations to atomic resolution images of the graphene. These modulations are attributed to the convolution of the electronic structure of the

copper square lattice of the crystal and the carbon honeycomb lattice of graphene, which interact to produce unique moiré superstructures in STM topographs [15,17].

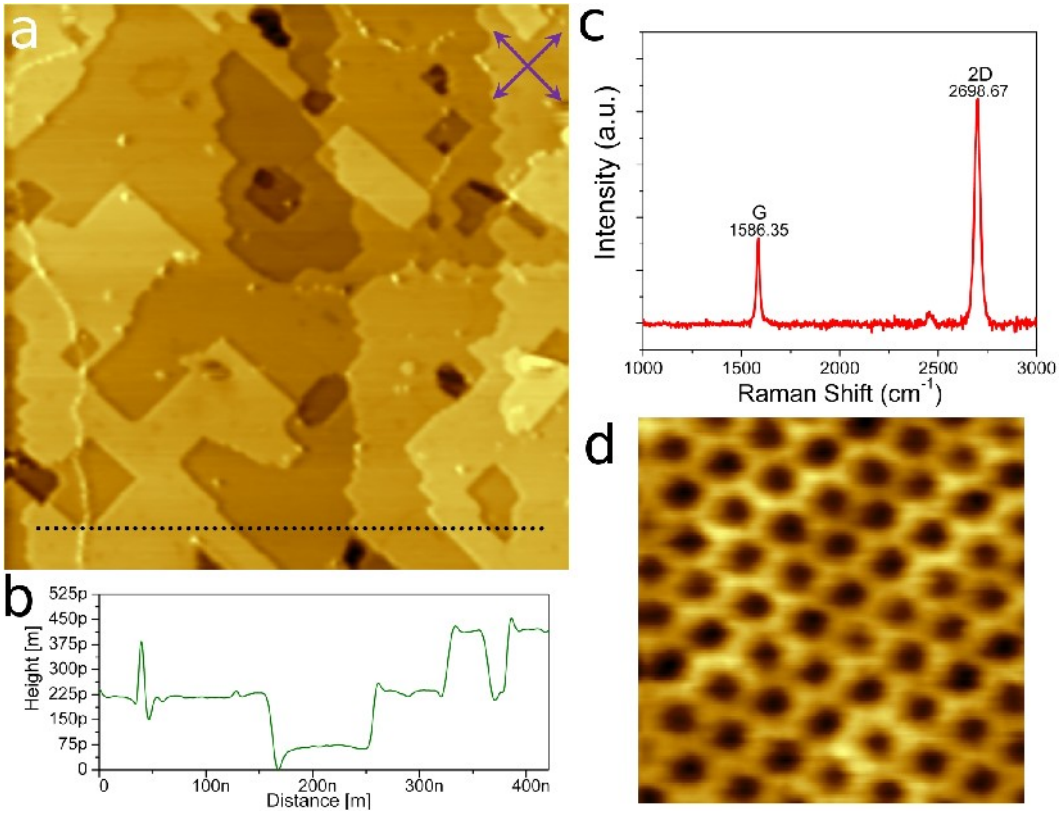

FIGURE 5.1. Characterization of as-grown graphene on Cu(100) single crystals. (a) Large area STM image of sample surface: $I_{tunneling} = I_t = 1.0$ nA, $V_{sample} = V_s = -75$ mV. Purple arrows act as a compass, indicating the {011} directions of the copper crystal. Line profile (b) taken from the dotted line in (a), showing single copper atom steps. (c) Typical Raman spectrum of crystal after growth. (d) Atomic resolution STM image of the graphene overlayer: $I_t = 5.0$ nA, $V_s = -75$ mV, Scale Bar = 0.75 nm.

Atomic resolution images taken at different areas of the single crystal surface show a variety of moiré superstructures, indicating that graphene grows in different orientations with respect to the underlying lattice. In certain STM images acquired over flat terraces of the surface, the graphene overlayer has a moiré superstructure with a well-defined linear periodic modulation as can be seen in **Figures 5.2a** and **5.2b**. These alternating bands in the STM topograph have a

1.25 nm spatial modulation frequency and make a 10° angle with the [1$\bar{1}$00] direction of the graphene sheet. Using the known directions of the Cu(100) single crystal surface and moiré pattern simulations, the linear superstructure is attributed to the case where the graphene [11$\bar{2}$0] direction makes a small angle of 3.5° with the [01$\bar{1}$] direction of copper. The result of a moiré simulation of this structure is provided in the hard sphere model of **Figure 5.2c**.

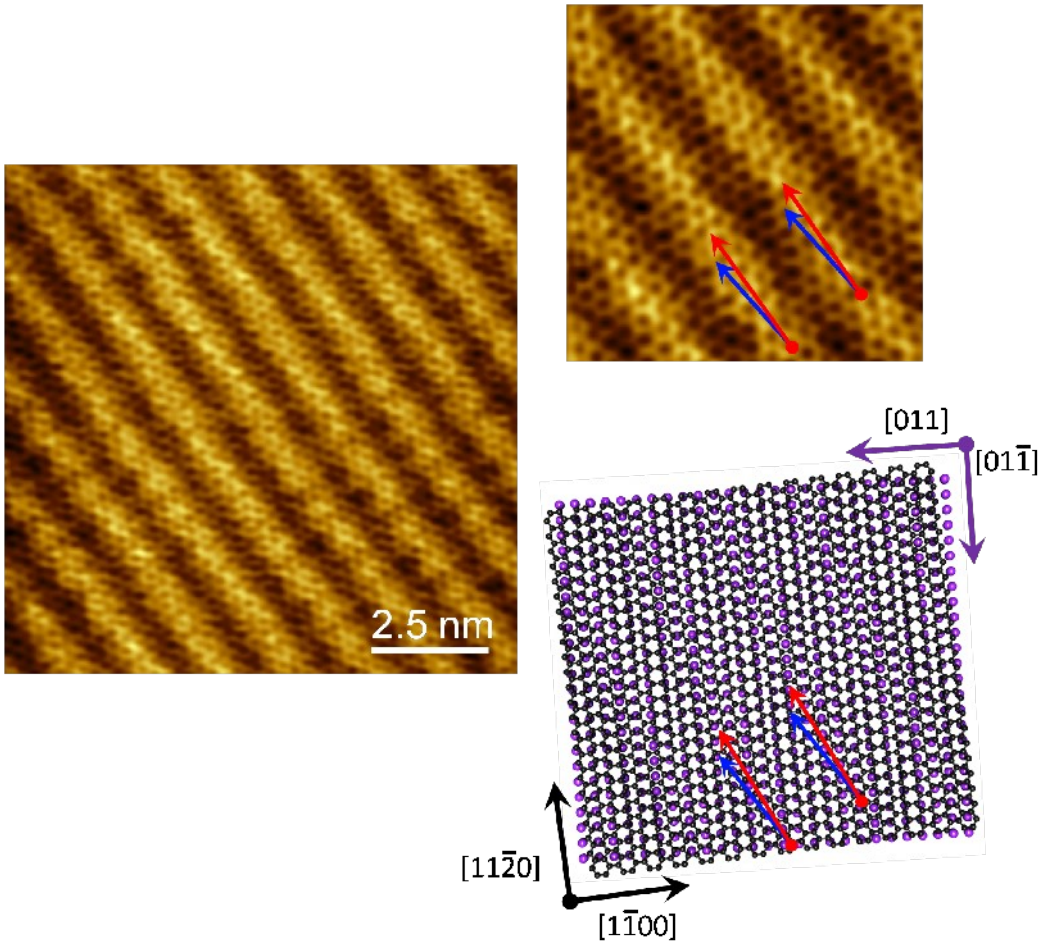

FIGURE 5.2. Moiré structure of graphene at a 3.5° angle with respect to the underlying copper crystal. (a) Large area image illustrating the linear periodic modulation to the graphene overlayer. (b) High-resolution image of the graphene structure. The parallel red arrows have a spacing of 1.25 nm and indicate the direction of the moiré pattern, which make a 10° angle with the [1**1**00] graphene direction highlighted with blue arrows. (c) Hard sphere atomic model of the two lattices. The black arrows and lattice belong to graphene and the purple arrows and spheres belong to the copper substrate. Imaging parameters: (a) and (b) I_t = 1.45 nA, V_s = -75 mV.

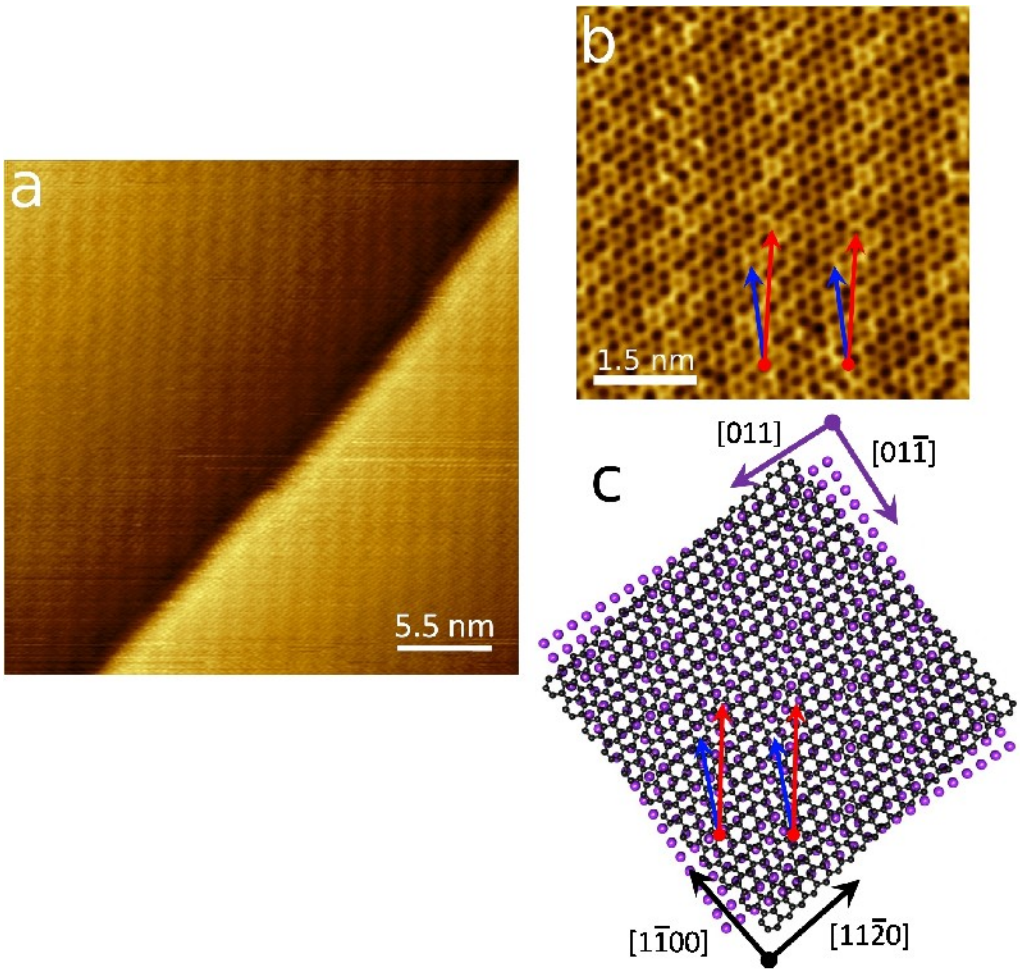

FIGURE 5.3. Moiré structure of graphene at a 10.0° angle with respect to the underlying copper crystal. (a) Large area image illustrating a linear periodic modulation to the graphene overlayer. (b) High-resolution image of the graphene structure. The parallel red arrows have a spacing of 1.35 nm and indicate the direction of the moiré pattern, which make a 8.5° angle with the [11**2**0] graphene direction highlighted with blue arrows. (c) Hard sphere atomic model of the two lattices. The black arrows and lattice belong to graphene and the purple arrows and spheres belong to the copper substrate. Imaging parameters: (a) and (b) I_t = 5.50 nA, V_s = -75 mV.

One of the larger angular differences found between the graphene sheet and the copper lattice produces the moiré pattern shown in **Figures 5.3a** and **5.3b**. In these areas, alternating bright and dark regions are, again, observed with a different overall moiré pattern. These linear bands make an 8.5° angle with the indicated [11$\bar{2}$0] direction of the graphene layer and have a

slightly larger spatial modulation frequency of 1.35 nm. This observed STM topography is attributed to the case where the graphene [$11\bar{2}0$] direction makes a 10° angle with the [$01\bar{1}$] direction of the copper. The result of the moiré simulation for this larger angular orientation is shown in **Figure 5.3c**.

The observation of multiple orientations between graphene and the single crystals has important implications regarding the CVD growth. First, graphene does not have a clear preferred orientation, which is likely the result of a weak interaction between the copper lattice and the extending graphene sheet. Second, the formation of grain boundaries between two different nucleated graphene sheets that bond together will contain carbon structures other than the ideal hexagonal carbon lattice to accommodate lattice mismatches. These grain boundaries can dramatically alter electron transport [26,27] and provide potential sites for mechanical failure under an applied stress [28]. Without the ability of the underlying substrate to minimize the mismatch between sheets, careful control of the nucleation rate on copper surfaces is necessary to synthesize large high quality graphene. Additionally, a variety of surface adsorption measurements can be accomplished on a single sample to study possibilities of opening a band gap in post modified graphene, as has been previously reported for growth on Ir(111) crystals [29].

With the observation of multiple orientations between the graphene overlayer and the copper lattice, we sought to characterize the growth evolution and crystallinity of the resulting graphene film using an SEM and a TEM. Using the SEM, we visualized the growth at partial and full surface coverage. This was accomplished in analogous manner as described in Chapter 3 on polycrystalline samples. **Figures 5.4a** and **5.4b** show typical SEM images taken of the partial growth of graphene islands on the single crystal surface. The islands have a characteristic four lobe structure, which has been previously reported for graphene growth on polycrystalline foils

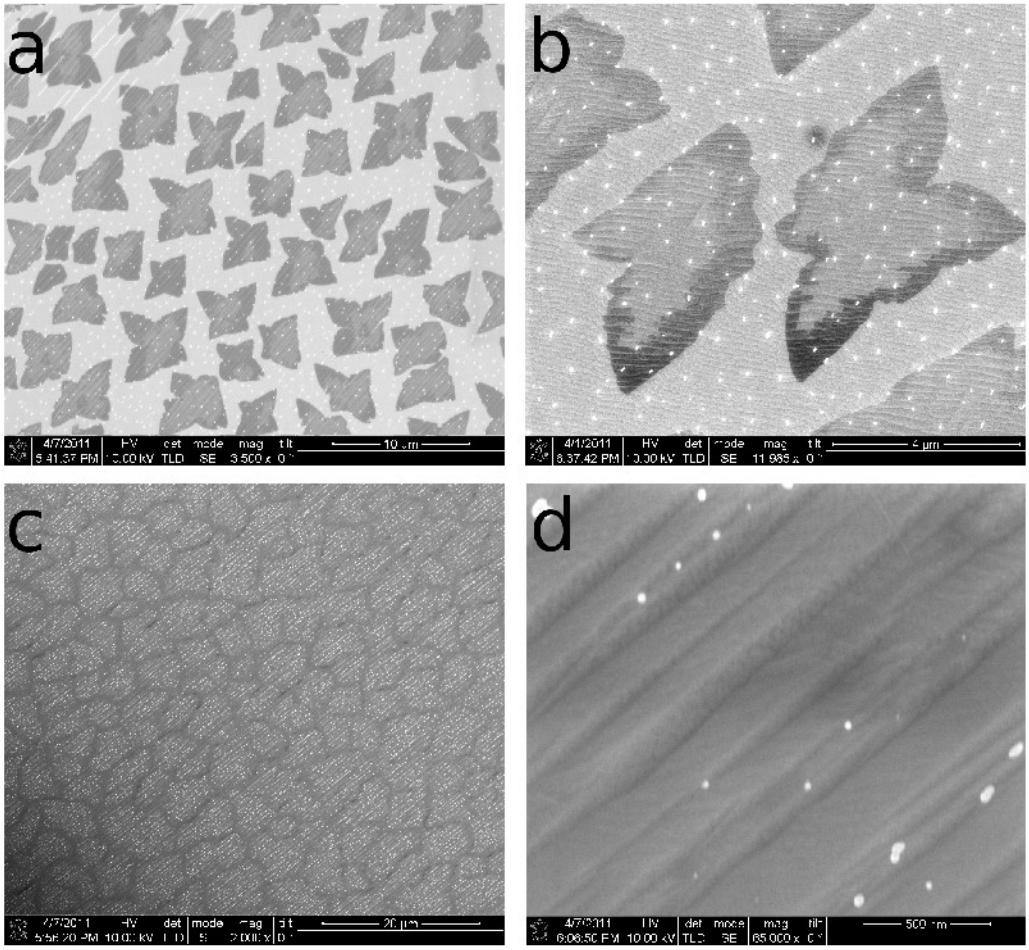

FIGURE 5.4. SEM images of graphene growth on Cu(100) single crystals. (a) Large area and (b) high magnification images of partial surface coverage illustrating the typical lobe geometry of individual islands. (c) Large area and (d) high magnification images of graphene growth after full surface coverage.

[18, 23], and discussed in Chapter 3. One possible explanation of the observed island shape can be attributed to the four fold symmetry of the underlying copper lattice rather than the six fold symmetry of the graphene hexagonal lattice. Mobile carbon atoms at the surface, or carbon carrying copper atoms, are expected to diffuse along one of the four equivalent lattice axis of the copper substrate before extending the growing island along one of the surface directions. As the reaction proceeds, the entire surface becomes covered with a continuous graphene overlayer. SEM images of full growth over the entirety of the surface are shown in **Figures 5.4c** and **5.4d**.

The apparent grains, or domains, appearing in **Figure 5.4c** are attributed to the coalescence of the four lobed islands into a continuous graphene overlayer.

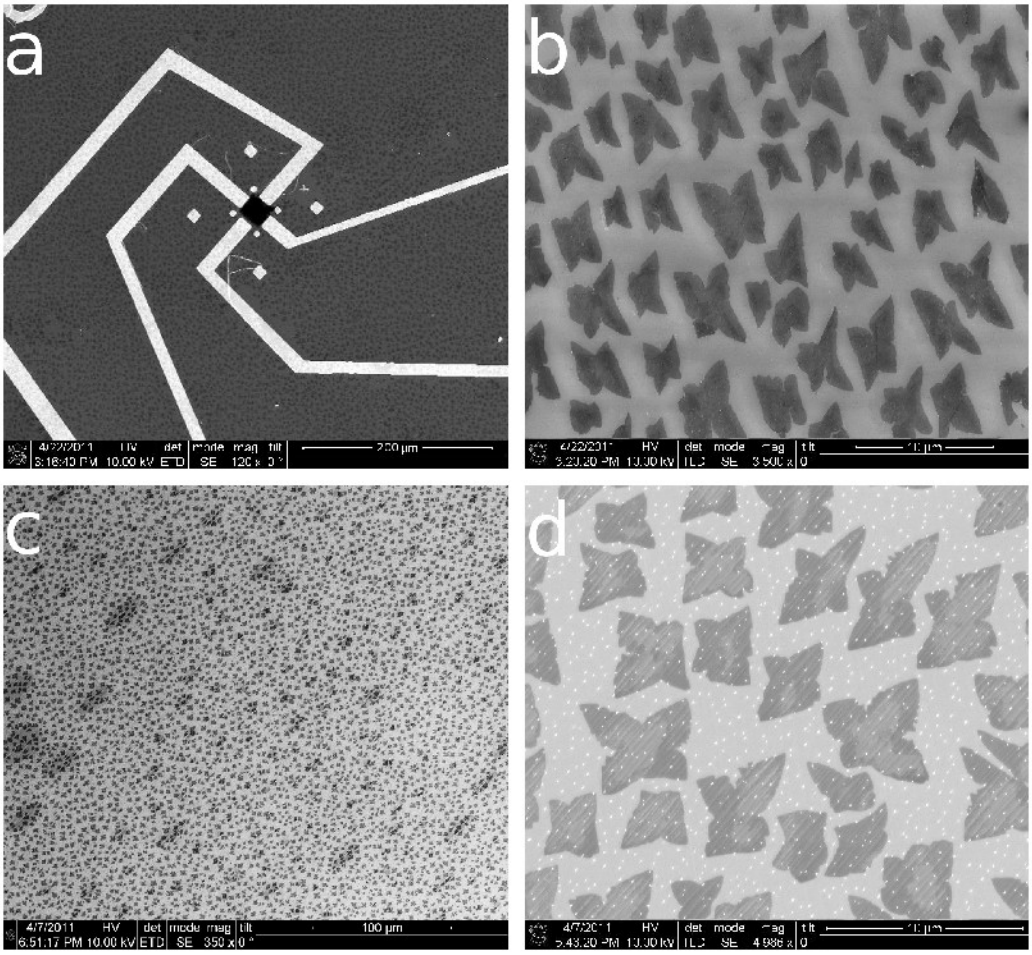

FIGURE 5.5. SEM images of transferred and as – grown partially grown graphene on Cu(100) single crystals. (a) Large area image of transferred graphene islands onto a TEM window. The black square of (a) corresponds to one of the coated TEM windows with surrounding markers. (b) High magnification image of transferred graphene islands on support chip near a window used for TEM analysis. (c) Large area image of as – grown graphene islands on a single crystal. (d) High magnification image of as – grown graphene islands on Cu(100) crystal. The elongated and more symmetric four lobe island morphology is clearly visible in both (b) and (d). Comparing (b) and (d), it is clear that the overall island shape and relative orientation between islands remains constant during the entire transfer process.

One natural question which arises from the observed SEM images is whether each isolated island is comprised of single or multiple orientations of graphene's honeycomb lattice. In order to address this issue, transfers were performed of the grown graphene islands to custom designed TEM windows for imaging and diffraction analysis using a spin – coated polymer support and wet chemical etching of single crystals. The transferred graphene islands showed minimal distortion or wrinkling on the new substrate as checked by the SEM and TEM. **Figure 5.5** shows the SEM images used to check the fidelity of the transfers from the single crystals.

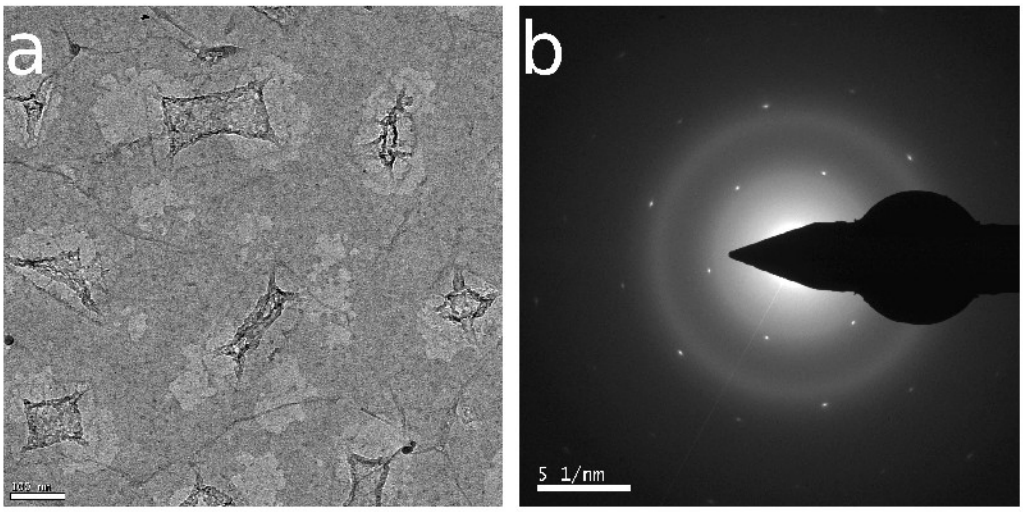

FIGURE 5.6. TEM analysis of a single graphene grain supported on a TEM window. (a) Bright – field TEM image of part of a graphene grain present in the fully grown transferred sample. The small square and rectangular shaped material are attributed to debris left from the transfer process. (b) SAED pattern of the same area showing only one crystallographic orientation of graphene. As the beam size is increased or moved over the sample, the diffraction pattern may include multiple graphene orientations or switch to just illuminating a different graphene domain.

In addition, high magnification TEM images were acquired over select regions of the graphene islands to check the transfer and sample crystallinity. **Figure 5.6** shows a typical high magnification image and diffraction pattern taken from a transferred sample atop a TEM

window. **Figure 5.7a** shows a lower magnification bright – field image of an entire graphene island on a TEM window. A selected area electron diffraction (SAED) pattern collected over the graphene island is shown in **Figure 5.7b** and reveals two distinct sets of graphene orientations. Measuring the angle between the selected diffraction peaks reveals a 28° rotation between these two sets of lattices. The real space distribution of the two orientations within the island can be visualized using dark – field TEM (DF – TEM) imaging by collecting specific diffracted electrons through an objective aperture placed in the back focal plane of the objective lens, as described in Chapter 3. **Figures 5.7c** and **5.7d** show the resulting DF – TEM images generated when diffracted electrons are collected from the circled regions shown in red and blue of **Figure 5.7b**. From the DF – TEM image it is clear that the upper lobe of the island is comprised of one crystalline domain and the rest of the island belongs to the other domain of a different orientation.

Given the polycrystallinity of the graphene islands, it is expected that as the graphene grows over the entirety of the surface the resulting continuous layer will contain many domains of different orientations as well. To corroborate this assertion, continuous graphene from fully covered single crystals were also transferred to TEM windows and analyzed. A bright – field image of a continuous graphene sheet and the SAED pattern of the same area are shown in **Figures 5.8a** and **5.8e**. From the SAED diffraction, it is clear that there are three distinct graphene orientations present in the illuminated area. Measuring the angle of the diffraction peaks, it is found that the blue domain is oriented 28° relative to the yellow domain, which in turn is oriented 4° relative to the red domain. Selecting each of the distinct diffraction spots and imaging using DF – TEM, again, allows for the real space visualization of the distribution of the different graphene orientations. The highlighted areas of **Figures 5.8b**, **5.8c**, and **5.8d** show that

the illuminated area has three distinct grains that have come together to form a continuous juncture within the grown graphene overlayer.

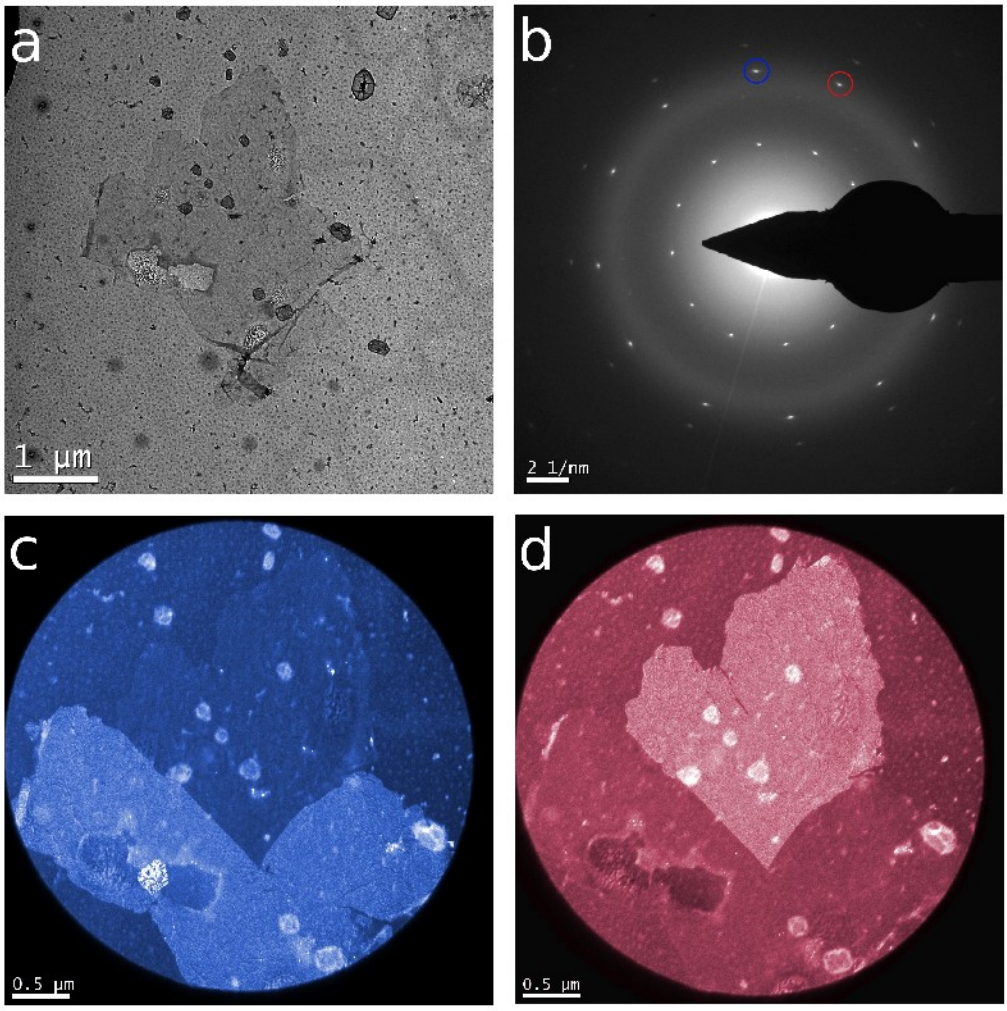

FIGURE 5.7. TEM analysis of a graphene island. (a) Bright – field image of a transferred island supported on a TEM window. (b) SAED pattern of illuminated island, illustrating two distinct crystallographic orientations of graphene within the island. (c) DF – TEM image showing the real space distribution of the crystal orientation when the objective aperture is placed over the diffraction spot circled in blue in (b). (d) DF – TEM image showing the real space distribution of the second graphene crystal orientation when the objective aperture is placed over the diffraction spot circled in red in (b).

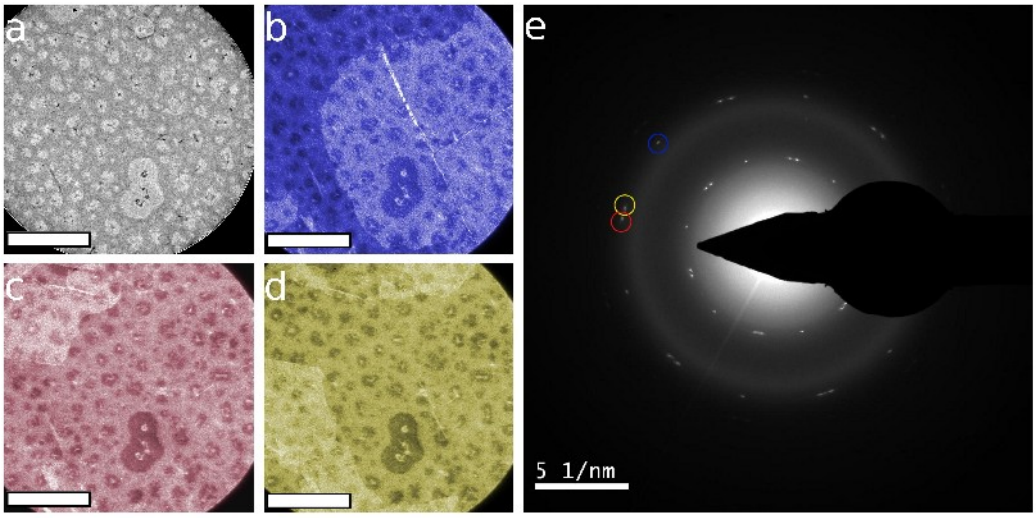

FIGURE 5.8. TEM analysis of full graphene growth. (a) Bright – field image of transferred graphene sheet supported on a TEM window. (b) – (d) DF – TEM images showing the real space distribution of different crystal orientations within the continuous graphene sheet when the objective aperture is placed over different diffraction spots of the illuminated region. Scale bars for (a) – (d) are 1 μm. (e) SAED pattern acquired over the illuminated region shown in (a) revealing the presence of three distinct crystallographic orientations of graphene. Colored circles show the position of the objective aperture when acquiring the DF – TEM images in (b) – (d).

In order to grow high quality graphene on copper, it is also important to understand which surface features in the copper contribute to defects in the growing carbon atomic lattice. Under growth models where the catalytic surface is treated as a stagnant structure, breaks in flat terraces at monatomic step edges and corners of the metal surface present possible sites for defect formation. Hence, these surface features are actively being studied, both, theoretically and experimentally [31,32]. In an upward growth over a monatomic copper step or corner, the extending carbon front of the graphene sheet may terminate through bonding of the carbon sigma bonds to adjacent copper atoms of a step or corner, producing line defects or point dislocations in the overlayer. When growing in the downward direction, the carbon sigma bonds are uninhibited by the copper substrate and continuous growth is expected.

In the number of experiments performed continuous growth of graphene in a “carpet” like draping over monatomic steps and corners (**Figures 5.9a**) is consistently observed on the Cu(100) surface. **Figure 5.9b** shows a current image simultaneously acquired with the image presented in **Figure 5.9a**. It clearly highlights the continuity of the overlayer since a large disparity exists between the small vertical corrugations of the graphene atomic lattice and the larger atomic step heights of copper. From **Figures 5.9a** and **5.9b** it is clear that graphene not only spans the edges of the steps but also grows continuously over the two different types of corners, which are characterized by either seven surrounding copper atoms (turquoise sphere of **Figure 5.9c**) or three surrounding atoms (green sphere of **Figure 5.9c**). This uninhibited growth over the copper surface may be the result of high copper adatom and island mobility at the growth temperatures of 1000 °C, where carbon carrying copper atoms can extend the sheet front in a type of “tiling” over the various surface structures [22]. In order to accomplish growth up or down steps, the nearly full coordinated corners (turquoise sphere of **Figure 5.9c**) present during growth provide high probability sites for atomic diffusion across steps, since diffusing atoms will follow trajectories that maximize coordination during motion [33]. The corners with lower coordination (green sphere of **Figure 5.9c**) have higher barriers to diffusions across the step boundaries and provide open sites for possible interaction with an extending graphene sheet. Surprisingly, continuous growth is observed over edges and both types of corners of the various smaller rectangular pits and islands present on the sample surface, revealing uninhibited growth in both the up and downward directions.

Continuous graphene growth over dislocations at the copper surface is also observed. **Figure 5.9d** and **5.9e** show graphene growth over a screw dislocation present at the copper surface. This screw dislocation is formed from the propagation of a double step edge out of a single terrace of atoms in the copper. While the screw dislocation may move laterally across the

surface during the growth, the structural identity is expected to remain constant providing a unique surface topography for graphene sheet extension.

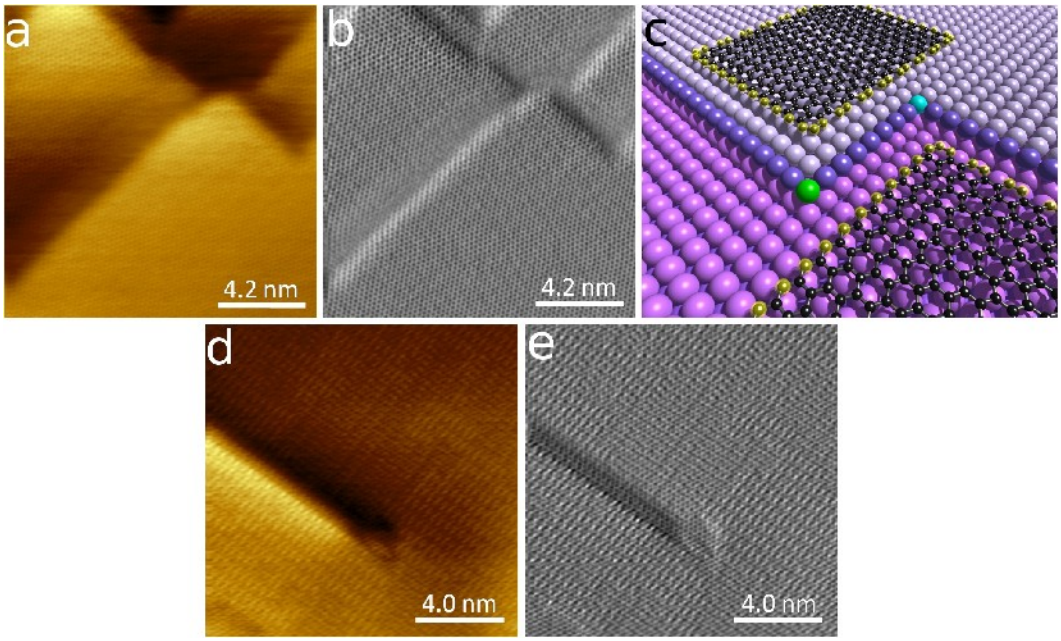

FIGURE 5.9. Atomic resolution images of continuous defect-free growth of graphene over Cu(100) single crystals. (a) STM topograph and simultaneously acquired (b) current image of graphene growth over copper monatomic step edges and corners. (c) Illustration of graphene growth over steps and corners of the Cu(100) single crystal surface. Magenta spheres belong to the lower terrace, gray spheres belong to the upper terrace, and dark purple spheres belong to the copper step edges. Two different types of copper corner atoms are colored in green and turquoise. Frontier carbon atoms are highlighted with yellow spheres. (d) STM topograph and (e) current image of defect-free growth over a screw dislocation in the copper substrate. Imaging parameters: (a) and (b) I_t = 1.74 nA, V_s = -75 mV, (d) and (e) I_t = 5.50 nA, V_s = -75 mV.

When imaging the graphene overlayer, a variety of protrusions and depressions are found over the sample surface. One interesting type of protrusion found on the sample surface is a "flower" structure. This type of structure has previously been observed on SiC grown graphene and is attributed to a defect which perturbs the electronic structure of graphene [26, 34 – 36]. A pair of these defects is shown in **Figure 5.10a** and a different isolated "flower" is shown in **Figure 5.10b**. These structures do not appear to show any correlation with specific surface

features present in the copper single crystal. The exact nature and atomic origin of this unique structure is currently under investigation since the presence of scattering centers and possible breaks in the perfect honeycomb lattice of graphene are expected to have profound effects on the electronic and mechanical properties of grown graphene [26 – 28]. For instance, defect engineering of graphene sheets can produce localized one dimensional metallic states within the carbon lattice [37], for use in electronics applications.

Observation of this type of defect on a substrate other than SiC grown graphene suggests that the scattering source is independent of the identity of the underlying material and likely due to a structure formed within the carbon atomic lattice. A survey of current experimental and theoretical STM work on defect structures and their appearance in STM topographs was performed in an attempt to identify the origin of this structure [38, 39]. Recent results on SiC suggest that the "flower" structure results from a rotational defect where a symmetric core of seven connected hexagons is rotated by 30 (or equivalently 90) degrees with respect to the remaining graphene lattice and stitched into the sheet with a closed loop of five- and seven-membered rings [36]. This proposed structure has recently been shown to exist experimentally in a high resolution TEM analysis of CVD grown graphene [40]. A ball-and-stick model of the proposed structure from Ref. 36 is provided in **Figure 5.10c**, where the center of the red group of carbon atoms corresponds to the center of the "flowers" observed in the STM images. The density functional theory (DFT) calculations of that work show good agreement with the experimental STM topography and accurately predict the observed height profile of the structures found in the graphene grown on Cu(100) single crystals in this work. A few interesting observations which support the assertion that the defect originates from a structure present within the graphene lattice is that the orientation and symmetry of the two defects present in **Figure 5.10a** are identical with each of the six "petals" positioned along the six directions of the carbon

atomic lattice. This is also seen in STM images of previous reports of SiC grown graphene [34].

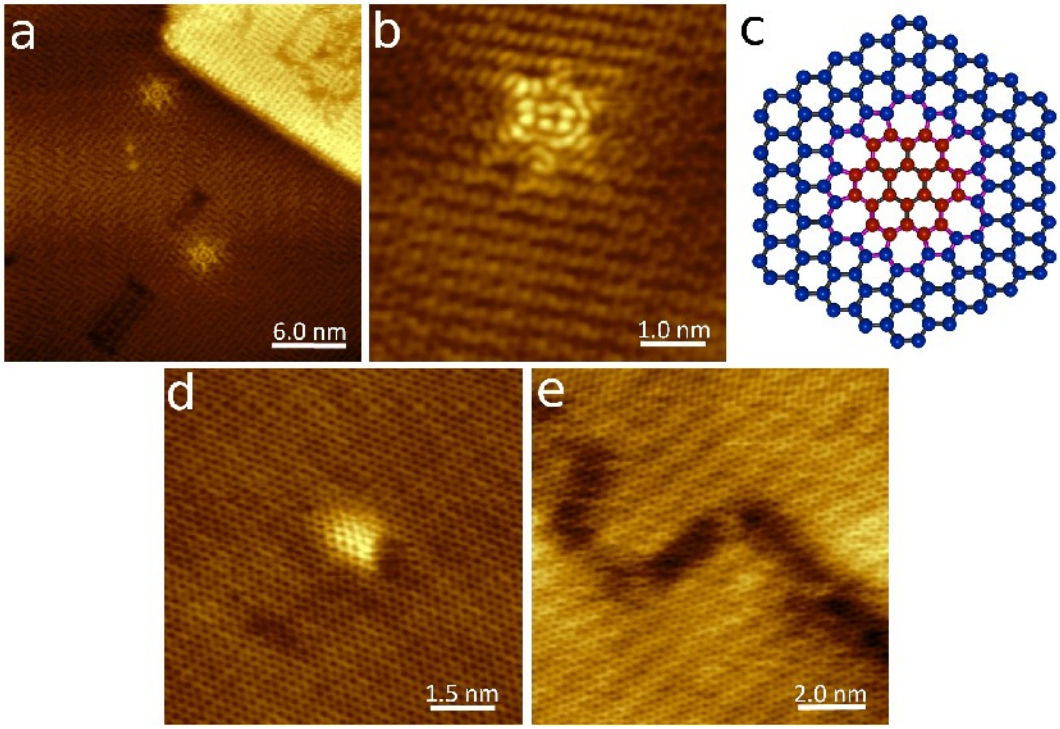

FIGURE 5.10. Small protrusions and depressions present at the sample surface. (a) STM image of two "flower" structures and two rectangular depressions. (b) High-resolution STM image of a "flower" structure in the carbon atomic lattice of graphene. (c) Atomic model of the "flower" structure proposed in Ref. 36. Red spheres belong to "inner" piece of graphene that is rotated by 30° with respect to the rest of the "outer" graphene sheet represented by blue spheres. The two domains are stitched together by six pentagon – heptagon pairs highlighted by magenta bonds in the model. (d) Continuous graphene growth over a copper adatom of the single crystal. (e) Pristine graphene suspended over atomic vacancies of the Cu(100) square lattice. Imaging parameters: (a) I_t = 5.50 nA, V_s = -75 mV, (b) I_t = 1.75 nA, V_s = -75 mV, (d) I_t = 1.40 nA, V_s = -75 mV, (e) I_t = 1.74 nA, V_s = -75 mV.

In addition to the above mentioned carbon structure, it is possible to observe graphene growth over defects within the underlying copper single crystal. **Figure 5.10d** shows growth over a protrusion in the substrate which is attributed to a small cluster of copper adatoms with a height that corresponds to a single monatomic copper step. There is no break in the carbon atomic lattice, no change in orientation of the moiré pattern present on the atomically flat

terraces, nor are there any scattering waves present near the protrusion indicating minimal perturbation to the structure of the sheet. **Figure 5.10e** shows a typical atomic resolution image of an observed depression present in one of the atomically flat terraces of the sample. Under normal imaging conditions these small regions have a height that is typically 30 – 60 pm lower than the surrounding terrace. The pristine atomic structure of the graphene sheet spans the depressed region where the moiré pattern is absent. Additionally, these depressed regions often have the same square symmetry of the underlying atomic lattice as can be seen in **Figure 5.10e** and the dark rectangular regions present in **Figure 5.10a**. From these observations we conclude that the depressions are copper atom vacancies in the flat terraces of the crystal covered with a continuous suspended sheet of graphene.

Interestingly, the depressions discussed above are not always static structures on the surface and often span large areas of tens of square nanometers as seem in **Figure 5.11**. In **Figure 5.12** a series of images taken over an area of 20 nm^2 where two of these smaller "moiré defects" show significant mobility at room temperature. Each image was taken over the same scan area, under identical scan parameters, with the static kink on the terrace edge serving as a reference point for observation of the copper motion. In order to explain the changes in shape of the vacancies, four distinct types of copper atom diffusion events may be considered; (1) arrival of a copper atom at an edge or corner, (2) diffusion along the edge of the vacancy, (3) movement across a corner where two edges meet, and (4) dissociation from a vacancy edge or corner into the vacancy. In the absence of the suspended graphene sheet, each of these distinct types of motion are expected to increase in energy since diffusing copper atoms prefer to decrease their overall coordination number during mobility [33]. Evidence for each of the diffusion events is observed in **Figure 5.12** with nucleation and dissociation of a small copper island within the vacancy observed in **Figure 5.12g**.

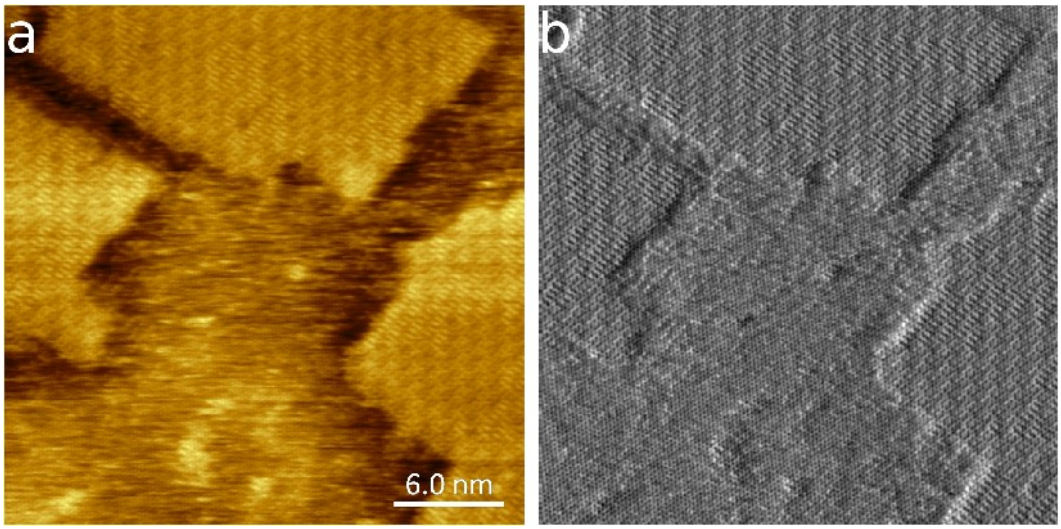

FIGURE 5.11. (a) Atomic resolution STM topograph and (b) simultaneously acquired current image of a large copper atom vacancy island overgrown with defect-free graphene. In this image the square symmetry of the underlying copper surface is clearly visible with the formation of dynamic copper islands within the large vacancy. Imaging parameters are: I_t = 5.0 nA and V_s = -75 mV.

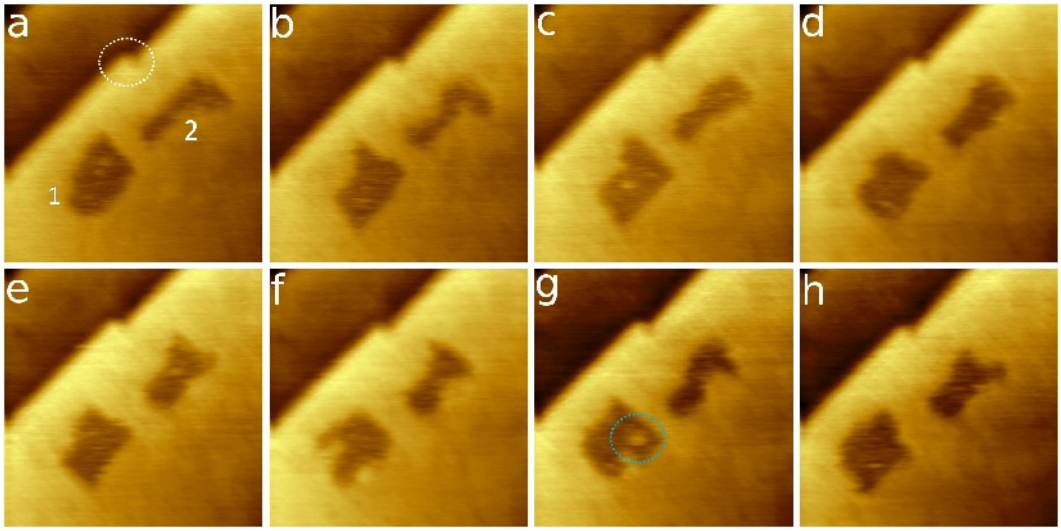

FIGURE 5.12. Copper atom mobility within vacancy islands covered with a continuous suspended sheet of graphene. The white circle highlights a static kink present on the terrace edge, which serves as a reference for visualizing the copper motion. The green circle highlights the formation and dissolution of a small copper atom cluster within the vacancy. Each of the 20 nm^2 images was acquired in 115 seconds, with an I_t of 1.00 nA and a V_s of -100 mV.

The observed mobility within the vacancies reveals that carbon atoms of the suspended sheet do not interact strongly with the copper substrate, since a strong interaction would be expected to pin the copper edges and trapped atoms of the vacancy, resulting in static structures in the STM topographs. While quantitative estimations of the interaction strength between the suspended sheet and the underlying copper surface is beyond the scope of the current work, it is interesting to note that over larger vacancies it is possible to lift the central areas of the suspended graphene sheet by altering the interaction between the STM tip and the graphene sheet. This is similar to what has been shown for exfoliated graphene on SiO_2 substrates [41]. Near the edges of the vacancies the graphene appears depressed, whereas the central region of these vacancies can undergo reversible deformation depending on the imaging parameters as can be seen in **Figure 5.13**. These observations suggest that the interaction strength between the graphene sheet and the copper may be close to a weak, van der Waals type, interaction rather than a more pronounced interaction resulting from significant overlap of the carbon p_z- and copper *d*-orbitals.

The mobility of copper atoms beneath the suspended graphene imaged at room temperature suggests that copper atom diffusion may also play an important role in the extension of the carbon lattice during growth. These mobile copper atoms may act as carbon carriers and efficiently extend the growing sheet over the steps and different corners present on the surface of copper substrates [22]. While the weak interaction between carbon and copper atoms permits significant surface diffusion, it also allows for the formation of a variety of orientations between the two lattices creating potential mismatches between neighboring graphene domains. To minimize the formation of scattering sources and generate large crystalline domains, recent work has shown that altering growth parameters such as flow rate, temperature, chamber pressure, and local growth environment can have substantial affects on the size of graphene crystallites, which

are ultimately determined by the average spacing of nucleation sites at the surface [42,43].

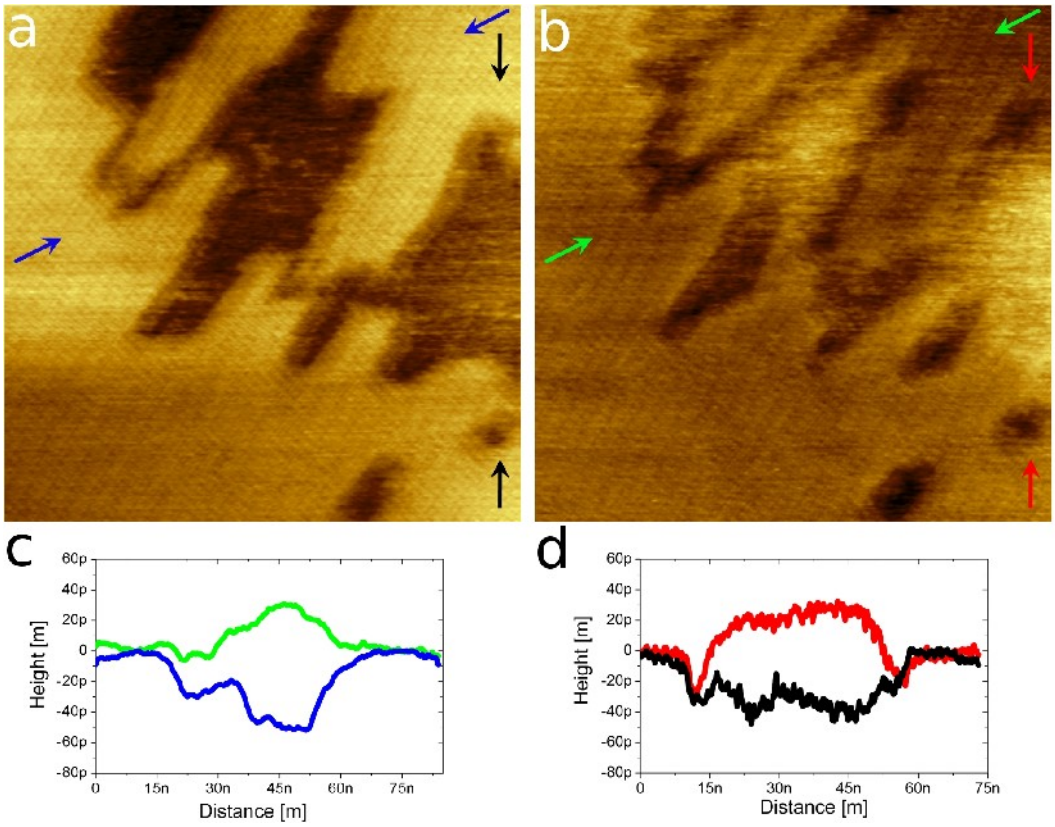

FIGURE 5.13. Manipulation of suspended graphene sheets covering large atomic vacancies on the copper single crystal surface. (a) STM image acquired at a V_s of +150 mV and (b) STM image acquired at a V_s of –150 mV. The large depressions can be lifted by the STM tip to overcome the substrate attractive force on the graphene sheet to produce protrusions at the surface. It should be noted that both of the images were acquired at the same tunnel current setpoint of 1.0 nA. In addition, this behavior is only observed where moiré patterns are absent from the graphene atomic structure. The two sets of line profiles (c) and (d) indicated in the STM topographs show an envelope of approximately 60 pm between the "depressed" and "lifted" regions. The depressions usually appear 30 – 40 pm lower than the surrounding terrace, whereas the protrusions usually appear 20 pm above the flat areas.

5.3 SUMMARY

In conclusion, the atomic scale characterization of graphene grown on Cu(100) single crystals by thermal decomposition of methane has been accomplished using STM. Graphene is found to grow over the square lattice of Cu(100) single crystals in a variety of orientations, which is expected to produce grain boundaries that contain carbon structures that depart from the ideal honeycomb lattice of graphene [30]. Through TEM characterization of graphene grown at partial and full surface coverage of single crystals, it is shown that the varied orientations give rise to nucleated islands and continuous graphene films which are polycrystalline in nature. The observed growth over steps, corners, and screw dislocations, as well as room temperature mobility of the underlying copper atoms suggest that substrate motion may play a significant role in the growth mechanism of graphene sheet extension on copper substrates. The observed variation in graphene growth orientation, in combination with the continuity over the various surface features of the Cu(100) single crystals reveal that the quality of grown graphene will ultimately be limited by the nucleation at the surface rather than the exact nature of the atomic structure of the underlying copper substrate. A fundamental understanding of the growth mechanism will help elucidate the factors that contribute to formation of the "flower" structures observed within the graphene lattice grown on copper crystals and may allow researchers to grow wafer-scale pristine graphene sheets. Future mechanistic studies may also aid in the rational incorporation of dopant atoms, such as nitrogen and boron, for electronic device applications.

5.4 MATERIALS AND METHODS

5.4.1 Graphene Growth

Graphene was grown by CVD of carbon from a mixture of high purity methane (CH_4) and hydrogen (H_2) gases at 1000 °C in a tube furnace. Copper (100) single crystals were loaded into a quartz tube and heated to 1000 °C over a period of ~40 minutes under a constant flow of H_2 gas. Samples were held at 1000 °C for 10 minutes before addition of CH_4. Graphene was grown under constant flow of CH_4 and H_2 mixtures. The samples were then cooled to room temperature before removal from the furnace. Copper (100) single crystals were purchased from MTI Corporation (www.mtixtl.com) with the following characteristics; length = width = 10.0 mm, thickness = 1.0 or 0.5 mm, and percent purity = 99.9999%.

5.4.2 STM Imaging

Samples were imaged under ambient conditions using a home-built scanning probe microscope housed in a custom-built enclosure. All images were acquired in constant current mode with tunneling setpoints between 0.2 nA and 30 nA. Typical sample biases were acquired between -30mV and -800 mV, referenced to the tip voltage. A Nanonis Universal SPM Controller was used for all data acquisition. Raw data was processed and analyzed with the SPM data analysis software known as Gwyddion (http://gwyddion.net/).

5.4.3. Raman Spectroscopy

Raman spectroscopy was acquired using a Renishaw Micro Raman microscope. An acquisition time of 600 seconds was used with a 514 nm laser. The laser power density

irradiating the sample was less than $2mW/\mu m^2$.

5.4.4. SEM Imaging

All SEM images were acquired using a FEI Nova 600 Dualbeam SEM/FIB. A typical operating voltage of 10 kV and typical currents of 0.5 – 2.0 nA were used to acquire all images presented in this chapter.

5.4.5. Transferred Samples for TEM Analysis

Partial and fully graphene covered single crystals were coated with a thin poly methyl methacrylate (PMMA) support. Three separate applications of 6% PMMA in anisole were spin coated onto single crystals and baked at 185 °C. Copper single crystals were completely dissolved in a $HCl/FeCl_3$ etchant solution (Transene, CE – 100). The etching process releases a floating polymer – graphene film whose top side never comes into contact with the etchant solution. The bottom of the film is then rinsed in deionized water by floating. The floating film is scooped out onto custom TEM substrates with amorphous SiO_2 windows. The PMMA is then removed by soaking the TEM substrate in acetone for 30 minutes.

5.4.6. TEM Analysis

All TEM images and data were acquired using a FEI Titan 80 – 300 kV S/TEM operated at 80kV to avoid damage of the graphene. Acquisition time for the DF – TEM images were 20 or 30 seconds per frame. An OA of 10 μm was used for all DF – TEM images. The second order diffraction peaks were used for DF – TEM images for an enhanced SNR when compared to first order diffracted electrons. SAED data was taken with a beam diameter of 3.6 μm.

5.5. REFERENCES AND NOTES

[1] Geim, A. K.; Novoselov, K. S. *Nat. Mater.* **2007**, 6, 183.

[2] Castro Neto, A. H.; Guinea, F.; Peres, N. M. R.; Novoselov, K. S.; Geim, A. K. *Rev. Mod. Phys.* **2009**, 81, 109.

[3] Lee, C.; Wei, X.; Kysar, J. W.; Hone, J. *Science* **2008**, 321, 385.

[4] Bunch, J. S.; van der Zande, A. M.; Verbridge, S. S.; Frank, I. W.; Tanenbaum, D. M.; Parpia, J. M.; Craighead, H. G.; McEuen, P. L. *Science* **2007**, 315, 490.

[5] Novoselov, K. S.; Geim, A. K.; Morozov, S. V.; Jiang, D.; Zhang, Y.; Dubonos, S. V.; Grigorieva, I. V.; Firsov, A. A. *Science* **2004**, 306, 666.

[6] Novoselov, K. S.; Geim, A. K.; Morozov, S. V.; Jiang, D.; Katsnelson, M. I.; Grigorieva, I. V.; Dubonos, S. V.; Firsov, A. A. *Nature* **2005**, 438, 197.

[7] Zhang, Y.; Tan, Y-W.; Stormer, H. L.; Kim, P. *Nature* **2005**, 438, 201.

[8] Novoselov, K. S.; Jiang, D.; Schedin, F.; Booth, T. J.; Khotkevich, V. V.; Morozov, S. V.; Geim, A. K. *Proc. Nat. Acad. Sci.* **2005**, 102, 10451.

[9] Berger, C.; Song, Z.; Li, X.; Wu, X.; Brown, N.; Naud, C.; Mayou, D.; Li, T.; Hass, J.; Marchenkov, A. N.; Conrad, E. H.; First, P. N.; de Heer, W. A. *Science* **2006**, 312, 1191.

[10] Emtsev, K. V.; Bostwick, A.; Horn, K.; Jobst, J.; Kellogg, G. L.; Ley, L.; McChesney, J. L.; Ohta, T.; Reshanov, S. A.; Röhrl, J.; Rotenberg, E.; Schmid, A. K.; Waldmann, D.; Weber, H. B.; Seyller, T. *Nat. Mater.* **2009**, 8, 203.

[11] Gilje, S.; Han, S.; Wang, M.; Wang, K. L.; Kaner, R. B. *Nano Lett.* **2007**, 7, 3394.

[12] Tung, V. C.; Allen, M. J.; Yang, Y.; Kaner, R. B. *Nat. Nanotechnol.* **2009**, 4, 25.

[13] Park, S; Ruoff, R. S. *Nat. Nanotechnol.* **2009**, 4, 217.

[14] Sutter, P. W.; Flege, J-I.; Sutter, E. A. *Nat. Mater.* **2008**, 7, 406.

[15] Coraux, J.; N'Diaye, A.T.; Busse, C.; Michely, T. *Nano Lett.* **2008**, 8, 565.

[16] Reina, A.; Jia, X.; Ho, J.; Nezich, D.; Son, H.; Bulovic, V.; Dresselhaus, M. S.; Kong, J. *Nano Lett.* **2009**, 9, 30.

[17] Ueta, H.; Saida, M.; Nakai, C.; Yamada, Y.; Sasaki, M.; Yamamoto, S. *Surf. Sci.* **2004**, 560, 183.

[18] Li, X.; Cai, W.; An, J.; Kim, S.; Nah, J.; Yang, D.; Piner, R.; Velamakanni, A.; Jung, I.; Tutuc, E.; Banerjee, S. K.; Colombo, L.; Ruoff, R. S. *Science* **2009**, 324, 1312.

[19] Gao, L.; Guest, J. R.; Guisinger, N. P. *Nano. Lett.* **2010**, 10, 3512.

[20] Zhao, L.; Rim. K. T.; Zhou, H.; He, R.; Heinz, T. F.; Pinczuk, A.; Flynn, G. W.; Pasupathy, A. N. http://arxiv.org/ftp/arxiv/papers/1008/1008.3542.pdf, 2010.

[21] Bae, S.; Kim, H.; Lee, Y.; Xu, X.; Park, J – S.; Zheng, Y.; Balakrishnan, J.; Lei, T.; Kim, H. R.; Song, Y. II; Kim, Y – J; Kim, K. S.; Özyilmaz, B.; Ahn, J – H; Hong, B. H.; Iijima, S. *Nat. Nanotechnol.* **2010**, 5, 574.

[22] Rasool, H. I.; Song, E. B.; Allen, M. J.; Wassei, J. K.; Kaner, R. B; Wang, K. L.; Weiller, B. H.; Gimzewski, J. K. *Nano Lett.* **2010**. DOI: 10.1021/nl1036403

[23] Wofford, J. M.; Nie, S.; McCarty, K. F.; Bartelt, N. C.; Dubon, O. D. *Nano Lett.* **2010**. DOI:10.1021/nl102788f

[24] Ferrari, A. C.; Meyer, J. C.; Scardaci, V.; Casiraghi, C.; Lazzeri, M.; Mauri, F.; Piscanec, S.; Jiang, D.; Novoselov, K. S.; Roth, S.; Geim, A. K. *Phys. Rev. Lett.* **2006**, 97, 187401.

[25] Graf, D.; Molitor, F.; Ensslin, K.; Stampfer, C.; Jungen, A.; Hierold, C.; Wirtz, L. *Nano Lett.* **2007**, 7, 238.

[26] Rutter, G. M.; Crain, J. N.; Guisinger, N. P.; Li, T.; First, P. N.; Stroscio, J. A. *Science* **2007**, 317, 219.

[27] Yazyev, O. V.; Louie, S. G. *Nat. Mater.* **2010**, 9, 806

[28] Grantab, R.; Shenoy, V. B.; Ruoff, R. S. *Science* **2010**, 330, 946.

[29] Balog, R.; Jørgensen, B.; Nilsson, L.; Andersen, M.; Rienks, E.; Bianchi, M.; Fanetti, M.; Laegsgaard, E.; Baraldi, A.; Lizzit, S.; Sljivancanin, Z.; Besenbacher, F.; Hammer, B.; Pendersen, T. G.; Hofmann, P.; Hornekaer, L. *Nat. Mater.* **2010**, 9, 315.

[30] Huang, P. Y.; Ruiz-Vargas, C. S.; van der Zande, A. M.; Whitney, W. S.; Levendorf, M.P.; Kevek, J. W.; Garg, S.; Alden, J. S.; Hustedt, C. J.; Zhu, Y.; Park, J.; McEuen P. L.; Muller, D. A. *Nature* **2011**, 469, 389.

[31] Chen, H.; Zhu, W.; Zhang, Z. *Phys. Rev. Lett.* **2010**, 104, 186101.

[32] Starodub, E.; Maier, S.; Stass, I.; Bartlet, N.C.; Feibelman, P. J.; Salmeron, M.; McCarty, K. F. *Phys. Rev. B* **2009**, 80, 235422.

[33] Zhang, Z.; Lagally, M. G. *Science* **1997**, 276, 377.

[34] Guisinger, N. P.; Rutter, G. M.; Crain, J. N.; Heiliger, C.; First, P. N.; Stroscio; J. A. *J. Vac. Sci. Technol. A* **2008**, 26, 932.

[35] Simon, L.; Bena, C.; Vonau, F.; Aubel, D.; Nasrallah, H.; Habar, M.; Peruchetti, J. C. *Eur. Phys. J. B* **2009**, 69, 351.

[36] Cockayne, E.; Rutter, G. M.; Guisinger, N. P.; Crain, J. N.; Stroscio, J. A.; First, P. N. http://arxiv.org/abs/1008.3574, 2010.

[37] Lahiri, J.; Lin, Y.; Bozkurt, P.; Oleynik, I. I.; Batzil, M. *Nat. Nanotechnol.* **2010**, 5, 326.

[38] Yazyev, O. V.; Louie, S. G. *Phys. Rev. B* **2010**, 81, 195420.

[39] Amara, H.; Latil, S.; Meunier, V.; Lambin, Ph.; Charlier J.-C. *Phys. Rev. B* **2007**, 76, 115423.

[40] Meyer, J. C.; Kurasch, S.; Park, H. Y.; Skakalova, V.; Künzel, D.; Groß, A.; Chuvilin, A.; Algara-Siller, G.; Roth, S.; Iwasaki, T.; Starke, U.; Smet, J. H.; Kaiser, U. *Nat. Mater.* **2011**, 10, 209.

[41] Mashoff, T.; Pratzer, M.; Geringer, V.; Echtermeyer, T. J.; Lemme, M. C.; Liebmann, M.; Morgenstern, M. *Nano Lett.* **2010**, 10, 461.

[42] Li, X.; Magnuson, C. W.; Venugopal, A.; An, J.; Won Suk, J.; Han, B.; Borysiak, M.; Cai, W.; Velamakanni, A.; Zhu, Y.; Fu, L.; Vogel, E. M.; Voelkl, E.; Colombo, L.; Ruoff, R. S. *Nano Lett.* **2010**, 10, 4328.

[43] Li, X.; Magnuson, C. W.; Venugopal, A.; Tromp, R. M.; Hannon, J. B.; Vogel, E. M.; Colombo, L.; Ruoff, R. S.; *J. Am. Chem. Soc.* **2011**, 9, 2816.

CHAPTER 6

CONCLUSION

6.1 SUMMARY AND CONCLUSIONS

In this thesis, a description of a home built fiber interferometer deflection sensor was discussed in the context of the design of a SPM system capable of imaging in ambient and liquid environments with true atomic resolution of both insulating and conducting substrates. With the low noise deflection sensor, it was possible to achieve true atomic resolution imaging of a mica surface in water with the FM – AFM dynamic mode of AFM operation. Upon completion of the deflection sensor and the operational status of the home built system, the microscope was used to understand graphene growth on copper substrates through atomic resolution imaging of the carbon overlayer in the STM mode of operation. On polycrystalline copper substrates, graphene is shown to grow continuously over the entire surface, spanning copper atom steps, vertices, and edges of highly irregular features present in the copper surface. The graphene was shown to grow over the copper (100) square lattice as well as the anisotropic vicinal copper (311) facet. In addition, the STM was used to study graphene growth on copper (100) single crystal substrates. The graphene was shown to grow continuously over the single crystal substrates as well. When imaging different regions of the sample surface, it was found that the graphene overlayer grows in different orientations with respect to the underlying copper lattice. Through the use of DF – TEM imaging it was confirmed that transferred graphene overlayers grown on single crystals are continuous and polycrystalline in nature.

6.2 POTENTIAL FUTURE WORK ON THE HOME BUILT SPM

For an instrument developer, their seems to be no end or sense of completion for a given piece of equipment. One can spend a life time improving the various parts or implementing newly designed components for enhanced instrument functionality. In this section, potential directions for future development will be discussed.

As discussed in Chapter 2, the AFM cantilever is mechanically excited with a piezo actuator present in the drive assembly of the constructed microscope. The use of this type of drive assembly can create resonances in the fluid which adversely affect the motion of the cantilever oscillation in liquid environments. When these additional resonances affect the drive signal, the phase locked loop (PLL) of the control electronics often loses lock and stops functioning. Since the PLL is the source of the feedback signal for the AFM imaging, this makes it impossible to proceed with experiments.

One possible solution to this problem would be to only move the cantilever itself, rather than the entire support chip. This results in a clean oscillation signal output to the PLL and allows for efficient tracking by the control electronics. In the current home built system with the fiber interferometer deflection sensor, two possible avenues for driving the cantilever would be to directly excite the cantilever with a modulating light source or by using a piezo electric cantilever that can be electrically excited. In the first configuration, laser light can create a deflection of the cantilever through the photothermal affect whereby the differential thermal expansion coefficients of the silicon cantilever and a reflective gold coating causes bending in the lever arm. In the interferometer configuration, the laser light can be passed down the optical fiber that is used for optical detection with a wave division multiplexer (WDM). A WDM is a passive optical component that allows for the combination of different wavelengths of light from separate fiber cables into a single optical path. The modulating light source will actuate the cantilever for dynamic modes of operation and can be implemented relatively easily in the home built microscope. For the piezo electric actuation, a special type of cantilever made from a quartz tuning fork can be implemented with a tungsten or gold wire tip that is electro - chemically etched to a sharp point for AFM or dual STM - AFM operation. In this case, no modification will be necessary to the deflection sensor and the tip may be placed into the liquid without

submersion of the quartz cantilever.

Another possible direction for instrument development would be to make efforts to minimize drift between the AFM tip and the sample, particularly in liquid environments. The drift produces deleterious image distortions, often times making results uninterpretable. In a typical liquid AFM experiment the cantilever is submerged in approximately 2 - 3 milliliters of liquid. This small volume needs to be replenished every 3 - 5 hours. Ideally, the sample and tip should be unperturbed for 24 hours after the initial set up of an AFM experiment. In order, to allow for the lengthy equilibration period, a siphon system can be implemented which will allow for a closed liquid system with approximately 50 - 100 milliliters of fluid. With this large liquid reservoir and a siphon system a tip and sample can be submerged prior to approach and left unperturbed in order to reduce drift.

6.3 POTENTIAL FUTURE WORK ON GRAPHENE

A variety of possible future directions for graphene research that make use of the ability to grow and transfer graphene to arbitrary substrates exist. The first, most accessible, avenue of research would be to explore the mechanical properties of CVD graphene. For example, AFM fracture measurements can be performed by using DF - TEM imaging to visualize suspended graphene grain boundaries and apply a known force until a failure event occurs. By doing this for a variety of orientations, a map can be made of the strength of grain boundaries as a function of mismatch angle between different graphene crystal regions. In addition, the fracture strength of single crystal regions could be measured and compared to measurements on pristine graphene derived from mechanical exfoliations.

Using suspended graphene membrane samples on TEM windows, a detailed analysis of the structure of graphene grain boundaries at a variety of angles can be visualized by both high

resolution TEM imaging and STM measurements. The TEM imaging can lead to understanding of the exact atomic positions, while STM measurements can yield information regarding the local electronic properties of the grain boundaries.